Functionalization of Ultrathin Alumina Films of Atomically Precise Thickness with Dye Molecules as Model Systems for Photoelectrodes

Dissertation

zur

Erlangung der naturwissenschaftlichen Doktorwürde
(Dr. sc. nat.)

vorgelegt der

Mathematisch-naturwissenschaftlichen Fakultät

der

Universität Zürich

von

Wolf-Dietrich Zabka

aus Deutschland

Promotionskommission:
Prof. Dr. Jürg Osterwalder (Vorsitz und Leitung der Dissertation)
Dr. Zbynek Novotny
Dr. Gerson Mette
Prof. Dr. Roger Alberto
Prof. Dr. David Tilley

Zürich 2018

Abstract

Dye-sensitized solar cells and photoelectrochemical cells are promising technologies for the future energy sector, and ultrathin insulating layers can improve their performance significantly. Here a suitable well defined model system is established for surface science to study the dye/insulator interface and first prototypical experiments are performed to achieve a better understanding of adsorption structures of dyes and of occurring charge transfer processes.

A crystalline atomic bilayer of alumina can be grown on the NiAl(110) surface and is an established well understood substrate for catalysis studies studies under ultra-high vacuum (UHV) conditions. To enable studies with variable tunneling barriers two methods are explored to increase the thickness of this thin film: The high-temperature oxidation of the clean NiAl(110) surface and the continued oxidation of the crystalline alumina bilayer. The latter balances the relevant thermodynamic processes in a more favorable manner and enables the production of thicker well-ordered films, as can be deducted from low-energy electron diffractograms. The film growth is monitored using quantitative X-ray photoelectron spectroscopy (XPS) and the topographic structure is of the films is studied using low-energy energy diffraction (LEED) and X-ray photoelectron diffraction (XPD). LEED indicates that the large unit cell of the alumina surface oxide is maintained in the observed thickness range of up to 1.5 nm and combined with XPD suggests the formation of sub-nanometer sized γ-Al_2O_3(111) nuclei in this unit cell. The electronic band structure of the thin films is mapped with angle-resolved photoemission and does not change drastically during the film growth.

In a next step these alumina films are functionalized with metalorganic dye molecules. The ultrathin alumina films on NiAl(110) are not stable in atmosphere and the NiAl continues to oxidize in an uncontrolled manner, which obstacles the functionalization with dye molecules from solution as a self-assembled monolayer (SAM). A vacuum chamber was developed to overcome this limitation and to deposit SAMs without taking the substrate out on air. The uncontrolled oxidation of the substrate can be reduced with this method to less then one atomic layer. The deposited SAM acts as a capping and passivates the dye/insulator/metal-heterostructure against air. Five different dye molecules are deposited on ultrathin alumina/NiAl(110) with this setup. Two prototypical ruthenium dyes and three rhenium dyes are characterized with XPS and ultraviolet photoelectron spectroscopy (UPS) to elucidate their electronic structure and to compare the molecular density of these molecules. Further light is shed on the counterion coadsorption of one rhenium and one ruthenium dye.

Ultrafast time-resolved core-level spectroscopy of rhenium 4f electrons in a dye/insulator/metal-heterostructure is used to observe the oxidation of the metal center upon optical excitation due to the metal-to-ligand charge transfer. An oscillating appearance of the oxidized species is observed. It is found that ultrafast time-resolved core-level spectroscopy is a promising technique with the potential to shine light on the charge carrier dynamics in such heterostructures and into the intramolecular charge transfer.

Zusammenfassung

Farbstoffsolarzellen und farbstoffbasierte photoelektrochemische Zellen sind vielversprechende Technologien für die zukünftige Energieproduktion und ultradünne isolierende Schichten können deren Leistung deutlich verbessern. Hier wird ein wohldefiniertes Modellsystem für die Oberflächenforschung zur Untersuchung der Farbstoff/Isolator-Grenzfläche etabliert. Erste prototypische Experimente werden durchgeführt, um ein besseres Verständnis der Adsorptionsstrukturen von Farbstoffen und der auftretenden Ladungstransferprozesse zu erreichen.

Eine kristalline atomare Doppellage aus Aluminiumoxid kann auf der NiAl(110)-Oberfläche gewachsen werden, welche ein etabliertes gut verstandenes Substrat für Katalyse-Studien im Ultrahochvakuum (UHV) ist. Um Studien mit variablen Tunnelbarrieren zu ermöglichen, werden zwei Methoden genutzt, um die Dicke dieses Films auf definierte Weise zu erhöhen: Die Hochtemperaturoxidation der sauberen NiAl(110)-Oberfläche und die weitergeführte Oxidation der kristallinen Aluminiumoxid-Doppellage. Letztere gleicht die relevanten thermodynamischen Prozesse vorteilhafter aus und ermöglicht die Herstellung von dickeren geordneten Filmen. Das Filmwachstum wird mittels quantitativer Röntgen-Photoelektronenspektroskopie (XPS) überwacht und die topographische Struktur der Filme wird mit der Beugung niederenergetischer Elektronen (LEED) und Röntgen-Photoelektronenbeugung (XPD) untersucht. LEED zeigt, dass die große Elementarzelle des Aluminiumoxid-Oxids in dem beobachteten Dickenbereich von bis zu 1.5 nm erhalten bleibt. XPD Daten und Simulationen impliziert die Bildung einer γ-$Al_2O_3(111)$-ähnlichen Nahordnung. Dies wird als die Formation von $Al_2O_3(111)$-Keimen in der grossen Einheitszelle interpretiert. Die elektronische Bandstruktur der dünnen Filme wird mit winkelaufgelöster Photoemission abgebildet und verändert sich kaum während des Filmwachstums.

Im nächsten Schritt werden diese Aluminiumoxidfilme mit metallorganischen Farbstoffmolekülen funktionalisiert. Die ultradünnen Aluminiumoxidfilme auf NiAl (110) sind in der Atmosphäre nicht stabil, da das NiAl unkontrolliert oxidiert. Dies beeinträchtigt die Funktionalisierung mit Farbstoffmolekülen aus Lösung als selbstorganisierende Monolage

(SAM). Eine Vakuumkammer wurde entwickelt, um diese Einschränkung zu überwinden und SAMs aufzubringen, ohne das Substrat aus dem UHV-System zu entnehmen und der Luft auszusetzen. Die unkontrollierte Oxidation des Substrats kann mit diesem Verfahren auf weniger als eine Atomlage reduziert werden. Die deponierte SAM wirkt als schützende Schicht und passiviert die Farbstoff/Isolator/Metall-Heterostruktur gegen Luft. Mit diesem Aufbau werden fünf verschiedene Farbstoffmoleküle auf ultradünnem Aluminiumoxid/NiAl(110) aufgebracht. Zwei prototypische Rutheniumfarbstoffe und drei Rheniumfarbstoffe werden mit XPS und Ultraviolett-Photoelektronenspektroskopie (UPS) charakterisiert, um ihre elektronische Struktur aufzuklären und die Moleküldichte in der Monolage zu vergleichen. Weiterhin wird auf die Koadsorption von Gegenionen von einem Rhenium- und einem Ruthenium-Farbstoff eingegangen.

Zeitaufgelöste Femtosekunden-Rumpfelektronen-Spektroskopie von Rhenium 4f-Elektronen in einer Farbstoff/Isolator/Metall-Heterostruktur wird verwendet, um die Oxidation des Metallzentrums bei optischer Anregung aufgrund des Ladungstransfers vom Metall zum Liganden zu beobachten. Ein oszillierendes Auftreten der oxidierten Spezies wird beobachtet. Es wird dargelegt, dass die zeitaufgelöste Femtosekunden-Rumpfelektronen-Spektroskopie eine vielversprechende Technik ist, um intramolekularen Ladungstransfer und die Ladungsträgerdynamik in solchen Heterostrukturen aufzuklären.

List of Acronyms

UHV	ultra-high vacuum
XPS	X-ray photoelectron spectroscopy
LEED	low energy electron diffraction
XPD	X-ray photoelectron diffraction
SAM	self-assembled monolayer
UPS	ultraviolet photoelectron spectroscopy
PES	photoelectron spectroscopy
STM	scanning tunneling microscopy
ESCA	electron spectroscopy for chemical analysis
ARPES	angle resolved photoelectron spectroscopy
TPP-2M	Tanuma-Powell-Penn equation
2PPE	two-photon photoelectron emission
tr-2PPE	time-resolved two-photon photoelectron emission
PC	positioning chamber
DC	deposition chamber
AC	analysis chamber
DFT	density functional theory
DCO$_2$bipy	2,2’-bipyridine-4,4’-dicarboxylic acid
SAMcham	SAM deposition chamber
bipy	diimine = 2,2’-bipyridine
DMPO3bipy	2,2’-bipyridine-4,4’-dimethylene phosphonate
OTf	trifluoromethane sulfonate
TBA	tetrabutylammonium
HOMO	highest occupied molecular orbital
LUMO	lowest unoccupied molecular orbital
MLCT	Metal-to-ligand charge transfer
EUV	extreme ultraviolet

Contents

1 Introduction and scope of the thesis

The global energy consumption increased steadily in the past and will likely continue to grow due to population and economic growth [1]. More than 60% of our current energy demand is covered by coal, oil, and gas [2], which is unsustainable due to their limited availability and the emission of greenhouse gases. Increasing usage of renewable energies can be a solution to this problem. Solar power has a special place among the renewable energy sources, as it has the highest potential among them to cover the global energy needs [3, 4]. The cost of photovoltaic modules and electricity produced by them decreased steadily since the 1970's [5, 6]. This trend is expected to continue [6] and might lead to a scenario where the cost of electricity produced by photovoltaic falls beneath the one of fossil fuels. After energy generation, energy storage from such renewable energy sources is a second challenge. Fig. 1.1 shows the Ragone plot for various methods of energy storage, where power and energy density of different storage systems are compared. The high energy density range is covered by chemical fuels, such as gasoline, methanol and hydrogen. Further, they are suited for long-term energy storage [7]. A sensible goal is the production and usage of such fuels in a carbon-neutral and sustainable way. This can be achieved by photocatalytic water splitting and CO_2 reduction [1, 8].

Photocatalytic water splitting uses the energy of light to generate hydrogen and oxygen from water. The first observed example of an overall water splitting system was reported by Fujishima and Honda on TiO_2 photoelectrodes under ultraviolet illumination in 1972 [9]. Since then various mostly inorganic materials and structures have been and are explored in order to find systems that achieve high solar light to hydrogen conversion efficiencies and that rely at best on abundant materials [10–14]. Dye-sensitized photoelectrochemical cells for water splitting are a comparably new field [14–16]. Similarly to dye-sensitized solar cells [10, 17], light absorption and charge carrier excitation is achieved in dye molecules. The absorption and electronic levels of these dyes can be tuned by molecular design and offer a high amount of flexibility. The working principle of a simple dye-sensitized photoelectrochemical cell for water splitting is depicted in Fig. 1.2: Solar light excites an electron in a dye. The hole is filled by an electron originating the water oxidation catalyst,

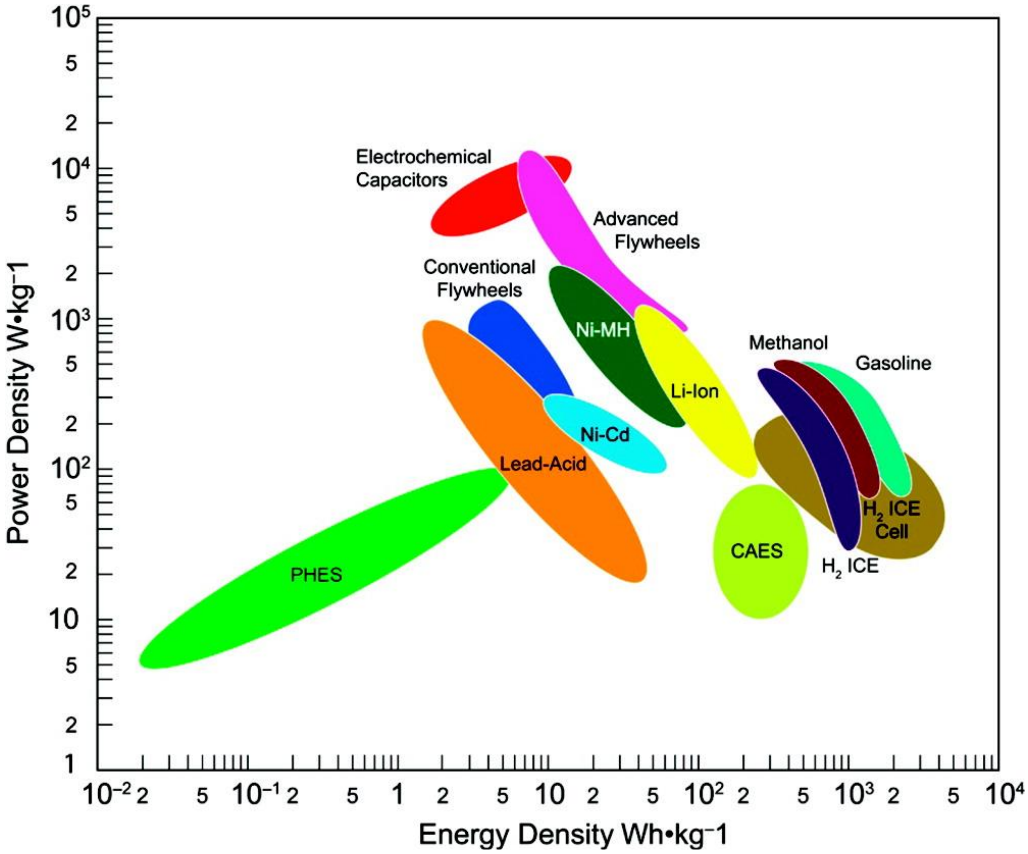

Figure 1.1: (a) Comparison of energy density and power density for different energy storage systems. Reprinted from Ref. [7].

which produces oxygen. The excited electron in the dye is transferred via the substrate to a counter electrode, where hydrogen is produced. Different configurations for such cells are possible [14–16]. Recently a first tandem cell for light-induced overall water splitting was reported, where organic dyes are used in the photocathode and the photoanode [18].

The efficiency of dye sensitized photoelectrodes is often determined by the kinetics of charge separation [10] and this kinetics play also a mayor role in dye sensitized photoelectrochemical cells [16]. Insulating layers can modify the performance of dye sensitized photoelectrodes [19–24], but a mechanistic understanding of the relevant processes is often not achieved. Occurring effects include i.e. the passivation of surface states, occupation of interface or intermediate states, and modulation of transfer rates through tunneling [22, 24–26].

The Nobel prize in chemistry was awarded in 2007 to Gerhard Ertl "for his studies of chemical processes on solid surfaces" [28]. He used surface science tools like low-energy electron diffraction (LEED), photoelectron spectroscopy (PES) and scanning tunneling microscopy (STM) to study the synthesis of ammonia and the oxidation of carbon monoxide on metal surfaces of well-defined single crystals and elucidated the relevant processes.

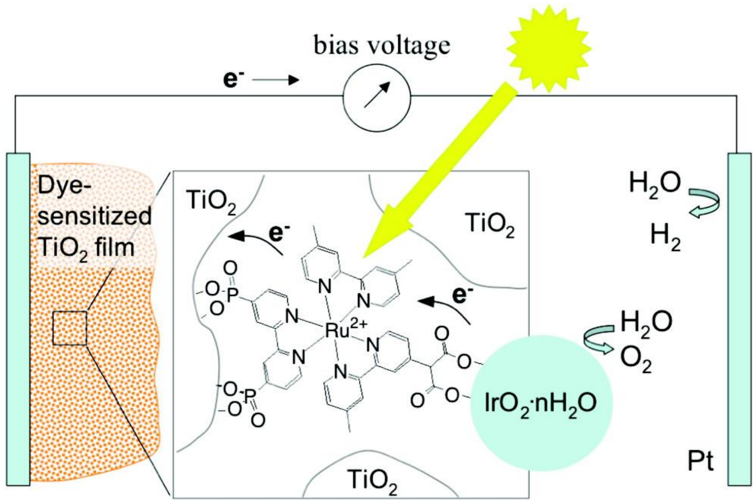

Figure 1.2: Schematics of a simple dye-sensitized photoelectrochemical cell for water splitting. Reprinted from Ref. [27].

Surface science had proven to give valuable insights into chemical processes at surfaces and interfaces. The scope of this thesis is to deliver a suitable surface science model system to study effects of an insulating layer in the dye-insulator interface of a photoelectrode. A prototypical ultrathin insulator is the alumina surface oxide of NiAl(110), which consists of two oxygen-aluminum-bilayers [29–33]. It is a well understood system [29–34] that has been used for various catalysis studies [34–36], making it the substrate of choice to start surface science investigations on the dye/insulator/metal interface.

Experimental results within this thesis are mostly based on photoelectron-based techniques, which are described in the following chapter. Experiments are conducted under ultra-high vacuum (UHV) conditions in an ESCA[1] laboratory. The structure of the thin film is described in detail. Two methods are explored with which the thickness of these alumina films can be varied: The established direct oxidation of the NiAl(110) surface at one temperature and oxygen pressure, and a multistep oxidation procedure. The later balances the relevant thermodynamic processes in a more favorable manner and produces films of higher crystallinity, as indicated by LEED. Structural changes within the thin film are observed with X-ray photoelectron diffraction (XPD) and interpreted as a transition to a more bulk-related structure. Further angle-resolved photoemission spectroscopy (ARPES) is used to elucidate the band structure of the alumina thin films. In a next step the ultrathin oxide films are functionalized with dye molecules from solution. As the NiAl substrate is prone to oxidation under ambient conditions, this involved the setup of a dedicated vacuum chamber, enabling the *in vacuo* deposition of self-assembled monolayers (SAM) from solution. The molecular overlayer passivates the oxide thin film against air. In the

---

[1] electron spectroscopy for chemical analysis (ESCA)

following, a total of five dye molecules based on rhenium and ruthenium are compared regarding coverage, counterion adsorption and electronic structure with X-ray photoelectron spectroscopy (XPS) and ultraviolet photoelectron spectroscopy (UPS). At last, ultrafast core-level spectroscopy on the metal center of a rhenium dye is implemented in collaboration with the HARMONIUM facility at the EPF Lausanne. The movement of electron density on the molecule induces a chemically shifted species, whichis used to study the dynamics of the excited molecule.

2 Photoelectron spectroscopy

2.1 Photoelectric effect

When light shines on a material, the energy of the photons can be transferred to electrons in the material. If the energy of the photons exceeds a certain threshold, the electrons can obtain enough energy to leave the material. Albert Einstein stated already in 1905 that the maximum kinetic energy an electron can obtain (E_{Max}) will be due to the energy conservation be equal to the energy of one incoming photon (E_{photon}). When these photo-excited electrons leave the material, they need to overcome a material-dependent potential barrier (Φ), thus reducing the maximum kinetic energy of the electrons [37]:

$$E_{Max} = E_{photon} - \Phi. \tag{2.1}$$

The material-dependent potential barrier Φ is the work function and the energy of the photon is given by its frequency ν:

$$E_{photon} = h\nu, \tag{2.2}$$

where h is the Planck constant. The process of the electron leaving the atom or material due to the photoelectric effect is called photoemission.

2.2 Three-step model of photoemission

In a solid, the photoemission process can be described by three steps [38, 39]:

1. excitation of the electron due to photon absorption
2. transport of the electron to the surface
3. escape of the electron into the vacuum

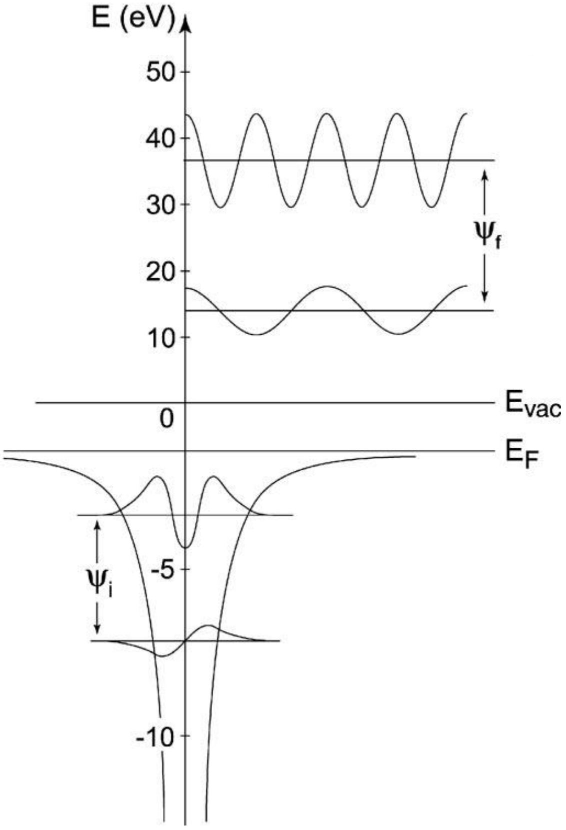

Figure 2.1: Excitation of an electron from the initial state $|\Psi_i\rangle$ into the final state $|\Psi_f\rangle$. Reprinted and modified from Refs. [39, 40].

2.2.1 Excitation of the photoelectron

The rapidly changing electric field can trigger the transition of an electron from the initial state $|\Psi_i\rangle$ with the energy E_i to a final state $|\Psi_f\rangle$ with the energy E_f by absorbing a photon. The transition rate $\Gamma_{i\to f}$ is given by Fermi's golden rule:

$$\Gamma_{i\to f} = \frac{2\pi}{\hbar}\left|\langle\Psi_f|H_{per}|\Psi_i\rangle\right|^2\rho, \tag{2.3}$$

and the density of the final states ρ is given by the energy conservation:

$$\rho = \delta\left(E_f - E_i - h\nu\right). \tag{2.4}$$

The perturbation Hamiltonian (H_{per}) of the electron due to the photon can in the absence of extremely high field strengths be written as [38, 39, 41]:

$$H_{per} = -\frac{e}{m_e c}\boldsymbol{A}\cdot\boldsymbol{p}, \tag{2.5}$$

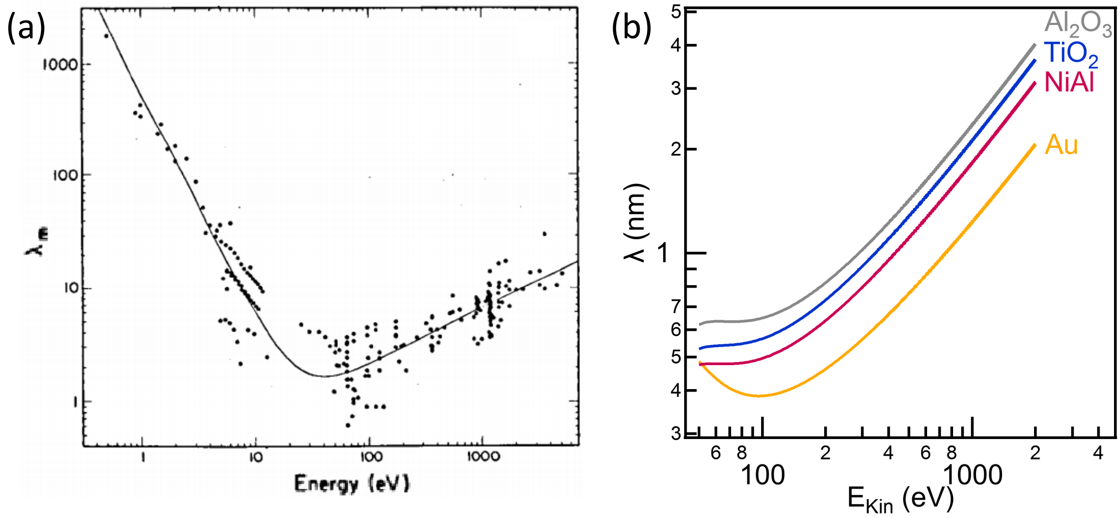

Figure 2.2: (a) Universal curve of the inelastic mean free path (in monolayers). Modified from Ref. [42]. (b) Calculated inelastic mean free paths for different materials using the TPP-2M equation (equation 2.7).

where **A** is the vector potential of the light and **p** is the electron momentum. The transition probability depends on the overlap of $|\Psi_i\rangle$ and $|\Psi_f\rangle$ and the wave function of $|\Psi_f\rangle$ will depend on the used photon energy, as indicated in Fig. 2.1. Thus the transition probability will be photon energy dependent [41].

2.2.2 Electron transport to the surface

Excited electrons moving in a solid can scatter due to various processes. An important characteristic summarizing these processes is the inelastic mean free-path λ, which describes the distance an electron with a certain energy can travel on average in a solid without scattering inelastically. This distance depends on the electron velocity $\hbar k/m_e$ and the lifetime due to inelastic scattering processes τ [43]:

$$\lambda = \left(\frac{\hbar k}{m_e}\right)\tau, \tag{2.6}$$

where k is the wave vector of the electron and m_e the electron mass. τ depends on the interaction of the electron with the surrounding. λ follows a universal trend as depicted in Fig. 2.2 (a).

For kinetic energies between 50 and 2000 eV, λ (in) can be predicted using the Tanuma-

Powell-Penn (TPP-2M) equation [43,44]:

$$\begin{aligned}
&\lambda(E_{Kin}) = \frac{0.1E_{Kin}}{E_P^2\left[\beta\ln(\gamma E_{Kin}) - (C/E_{Kin}) + \left(D/{E_{Kin}}^2\right)\right]} \text{ (in nm)},\\
&\beta = -0.10 + 0.944\left(E_P^2 + E_G^2\right)^{-0.5} + 0.069\rho^{0.1},\\
&\gamma = 0.191\rho^{-0.5},\\
&C = 1.97 - 0.91U,\\
&U = N_\upsilon\rho/M = E_P^2/829.4,\\
&E_P = 28.8(N_\upsilon\rho/M)^{0.5},
\end{aligned} \tag{2.7}$$

where E_P is the free-electron plasmon energy (in eV), N_υ is the number of valence electrons, ρ is the density (in g/cm^3), E_G the band gap (in eV), E_{Kin} the kinetic energy of the electrons (in eV), and the M is the atomic or structural unit weight (in g/mol). Fig. 2.2 (b) shows calculated values for different materials.

2.2.3 Escape to the vacuum

After excitation, the photoelectron with a wave vector $\boldsymbol{k}$ can be described with the dispersion of a free-electron:

$$E_f(\boldsymbol{k}) = \frac{\hbar^2\boldsymbol{k}^2}{2m_e} - E_0, \tag{2.8}$$

where E_0 refers to the energy between the bottom of the valence band and the Fermi level. After leaving the surface, the electron has a certain kinetic energy E_{Kin}. When considering it as a free electron in the vacuum, it has a wave vector $\boldsymbol{K}$:

$$E_{kin}(\boldsymbol{K}) = \frac{\hbar^2\boldsymbol{K}^2}{2m_e}. \tag{2.9}$$

The wave vectors are here separated in one component parallel to the surface and one perpendicular:

$$\begin{aligned}
E_f(\boldsymbol{k}) &= \frac{\hbar^2\left({k_\parallel}^2 + {k_\perp}^2\right)}{2m_e} - E_0,\\
E_{Kin}(\boldsymbol{K}) &= \frac{\hbar^2\left({K_\parallel}^2 + {K_\perp}^2\right)}{2m_e}.
\end{aligned} \tag{2.10}$$

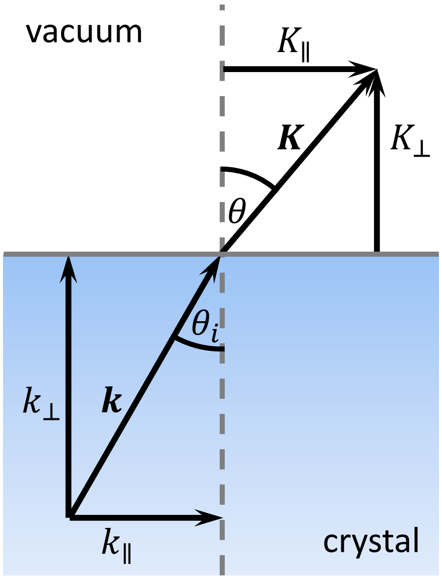

Figure 2.3: Wave vectors vector of an electron before and after it penetrates a surface.

When moving from the inside of the material to the vacuum, the electron needs to overcome the work function Φ. After that E_{Kin} is given by:

$$E_{Kin} = E_f - \Phi. \tag{2.11}$$

This reduces the energy of the electron and thus the wave vector shortens as indicated in Fig. 2.3. The parallel momentum of the electron and the corresponding wave vector are maintained due to energy conservation and translational symmetry at the surface [38, 39, 41]:

$$K_\parallel = k_\parallel. \tag{2.12}$$

Further, the parallel momentum in the crystal and in the vacuum can be expressed using equations 2.10, 2.11 and trigonometry:

$$\begin{aligned} K_\parallel &= \sqrt{\frac{2mE_{Kin}}{\hbar^2}}\sin(\theta), \\ k_\parallel &= \sqrt{\frac{2m\left(E_{Kin}+\Phi+E_0\right)}{\hbar^2}}\sin(\theta_i), \end{aligned} \tag{2.13}$$

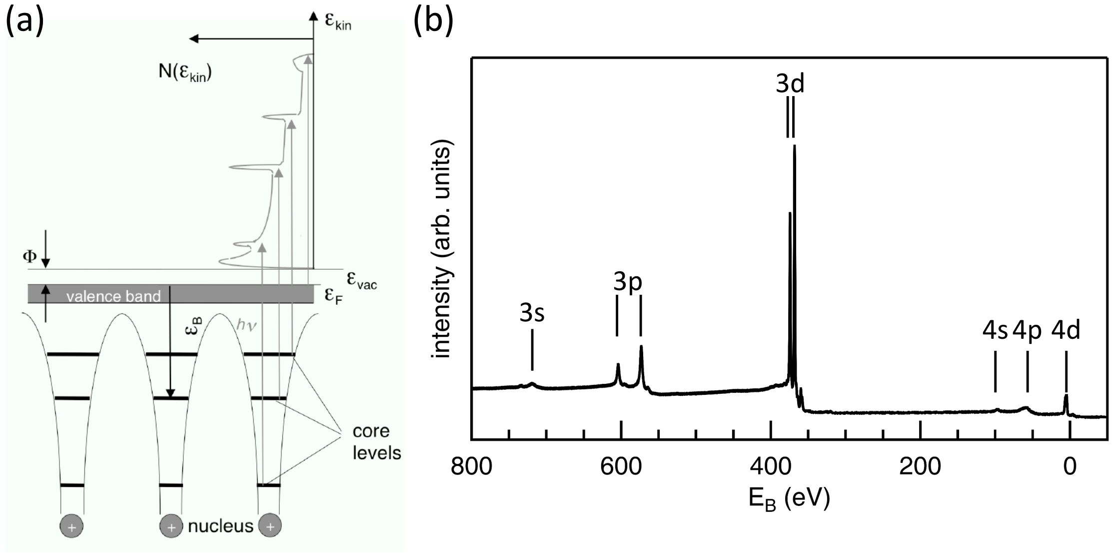

Figure 2.4: (a) Illustration of core-level states in a solid and the resulting photoelectron spectrum. Modified from Ref. [41]. (b) XPS of a silver sample. The observed states are marked.

where θ_i and θ are the polar angles as indicated in Fig. 2.3. From equation 2.13 follows a diffraction law for the electron waves:

$$\frac{\sin(\theta_i)}{\sin(\theta)} = \sqrt{\frac{E_{Kin}}{E_{Kin} + \Phi + E_0}}. \tag{2.14}$$

The perpendicular momenta in the crystal $k_\perp$ and the vacuum $K_\perp$ are given by [39]:

$$\begin{aligned} k_\perp &= \sqrt{\frac{2m}{\hbar^2}\,(E_{Kin}\cos^2(\theta) + E_0 + \Phi)}, \\ K_\perp &= \sqrt{\frac{2m}{\hbar^2}\,(E_{Kin})\cos(\theta)}. \end{aligned} \tag{2.15}$$

2.3 X-ray photoelectron spectroscopy

The photoelectric effect can be used to excite electrons from core-levels, as indicated in Fig. 2.4 (a). These photoelectrons are used for spectroscopy and bear information about the chemical environment of the atom. Generally X-rays are used for the excitation of photoelectrons from core-levels, resulting in the name X-ray photoelectron spectroscopy. The kinetic energy of a photoelectron produced is given by:

$$E_{Kin} = h\nu - E_B - \Phi. \tag{2.16}$$

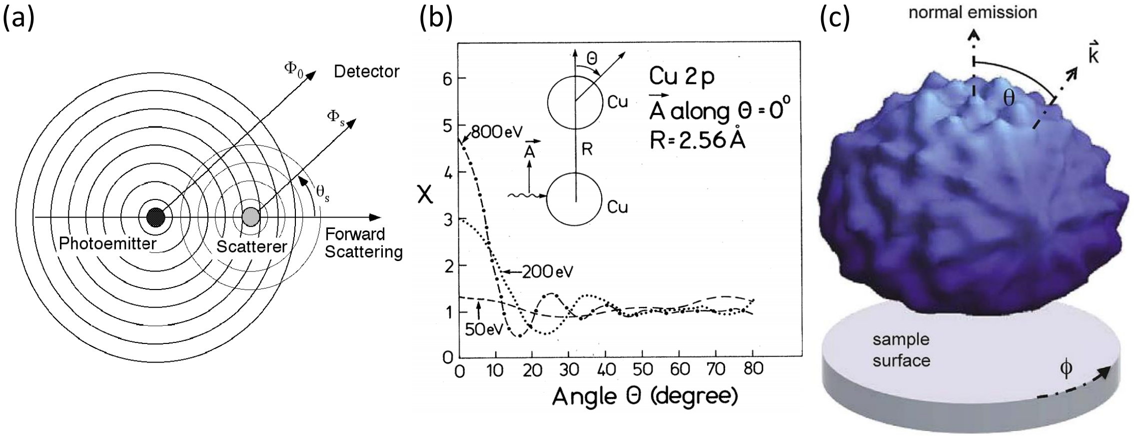

Figure 2.5: (a) Photoelectron wave from an emitter (Φ_0) and wave scattered at an neighboring atom (Φ_S). Reprinted from Ref. [41]. (b) Angle-dependent photoelectron enhancement for an emitting copper atom due to a neighboring copper atom for different photon energies. Reprinted from Ref. [45]. (c) Distribution of Bi 4f photoelectron intensity of a Bi(111) single crystalline surface. Reprinted from Ref. [46].

The binding energy E_B of the electrons is the energy difference between the Fermi level and the respective core-level. Fig. 2.4 (b) shows a measured XPS of a silver sample. Occurring binding energies are characteristic for certain elements. Thus this method can be used for elemental analysis. Binding energies also depend on the chemical environment and can give information about the chemical environment of the emitting atom. The inelastic mean free path of the photoelectrons is typically a few nanometers or less (see subsection 2.2.2), making it a surface sensitive method.

2.4 X-ray photoelectron diffraction

Photoelectrons from core-levels originate from specific atoms and thus have well-defined sources. The wave-particle dualism states that these photoelectrons have wave properties. Photoelectron waves can scatter at neighboring atoms and produce scattered waves, as depicted in Fig. 2.5 (a). Both waves will form an interference pattern, which will modulate the photoelectron intensity. Fig. 2.5 (b) shows the calculated intensity enhancement X of a copper atom due to a neighboring atom due to this effect [45]. For higher kinetic energies the intensity is increased more and more in the forward direction, which is called forward scattering enhancement. On single crystalline samples, this effect can result in highly anisotropic X-ray photoelectron diffraction pattern. Fig. 2.5 (c) shows the distribution of photoelectron intensity of the Bi 4f core-level electrons originating from a Bi(111) surface

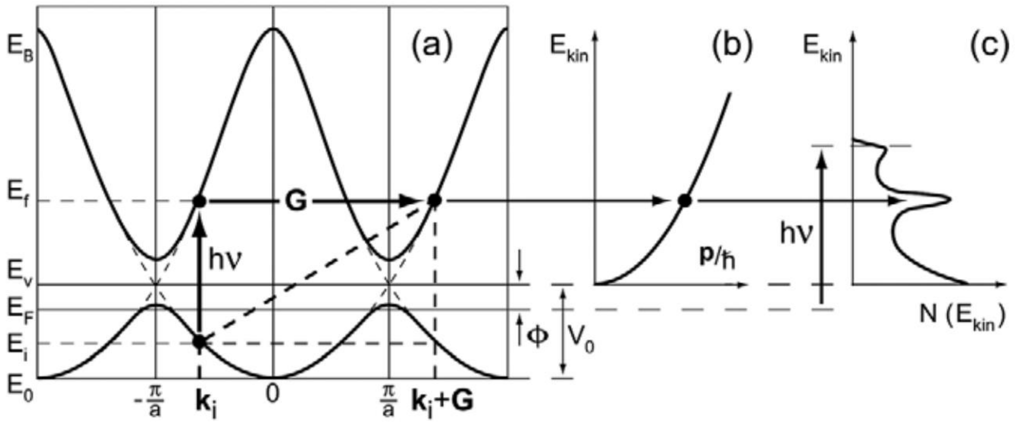

Figure 2.6: Scheme for recording the band structure of a solid with ARPES. (a) Transition from the initial state into the final state due to photon absorption. (b) After the electron is transferred into the vacuum it can be described as a free electron. (c) Detection of photoelectrons leads to a photoelectron spectrum of the valence band. Reprinted from Refs. [38,47].

over the hemisphere above the sample [46]. These interference patterns carry information about the position of the emitting and scattering atoms.

2.5 Angle-resolved photoemission spectroscopy

Valence band electrons and thus electrons close to the Fermi level define essential electric properties of a material. Ultraviolet photoelectron spectroscopy and in particular angle-resolved photoemission spectroscopy (ARPES) give direct information about the electronic structure of materials by measuring emitted photoelectrons in dependence of their kinetic energy, emission angle and photon energy. Photoelectrons originating from these electronic states have low binding energy and can according to equation 2.16 be measured with ultraviolet photons. As described in subsection 2.2.3, the electrons are excited in the solid and brought into the final state (Fig. 2.6 (a)). For low photon energies the momentum of the photon is negligible, and thus the momentum of the electron is nearly preserved. The photon is transferred to the vacuum (Fig. 2.6 (b)), and the photoelectron spectrum is detected (Fig. 2.6 (c)). By recording spectra for different emission angles and photon energies it is possible to vary $k_{||}$ and $k_\perp$ according to equations 2.13 and 2.15 to elucidate the band structure.

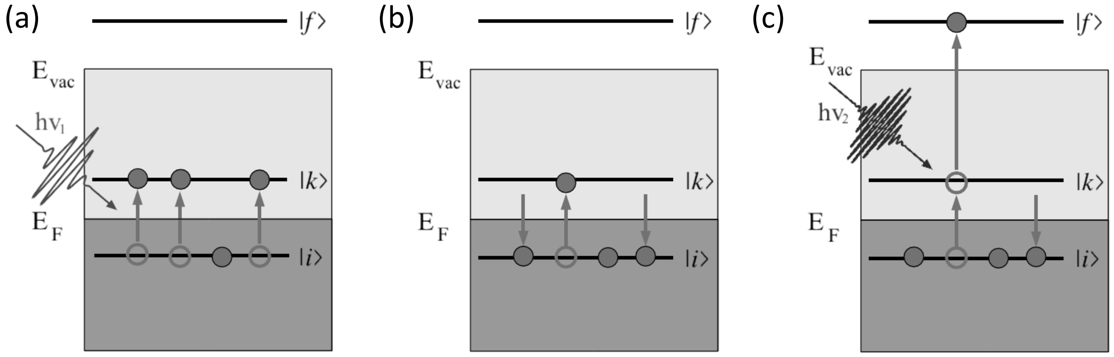

Figure 2.7: (a) Excitation of the system from the initial state to the intermediate state with the pump pulse. (b) Relaxation of the system. (c) The population of the final state from the intermediate state with the probe pulse after a certain time delay. Reprinted from Ref. [48].

2.6 Time-resolved photoelectron spectroscopy

Time-resolved photoelectron spectroscopy gives insights into ultrafast dynamical processes. Pulsed light sources excite the system of interest with a pump pulse, and probe photoelectrons from the excited system after a certain time delay. Varying the time delay between both pulses allows studying the temporal evolution of processes. Fig. 2.7 shows the principle of time-resolved two-photon photoelectron emission (tr-2PPE). The population of the final state $\left|\Psi_f\right\rangle$ does not happen in one step (as in ARPES or XPS), but rather in three steps:

1. A pump pulse brings electrons from the initial state $|\Psi_i\rangle$ into an excited intermediate state $|\Psi_k\rangle$.
2. The intermediate state has a certain lifetime. The occupancy of $|\Psi_k\rangle$ changes over time, as the system relaxes.
3. The system is probed after a certain time delay by a second photon pulse, bringing electrons from the intermediate state $|\Psi_k\rangle$ into a final state $\left|\Psi_f\right\rangle$ above the vacuum level.

The number of electrons that are transferred from the intermediate state $|\Psi_k\rangle$ into a final state $\left|\Psi_f\right\rangle$ depends on the occupancy of $|\Psi_k\rangle$. When varying the time delay between pump and probe pulse, the population of $|\Psi_k\rangle$ is probed as a function of time. It is also possible to probe electrons that were not excited by the pump pulse, when the photon energy of the probe pulse is higher then the work function.

3 ESCA laboratory

The experiments described in chapters 4 to 6 were performed in a user modified ESCA laboratory in the surface physics group of the University of Zürich, as well as the sample preparation for the experiments described in chapter 7. The base pressure is below $3 \cdot 10^{-10}$ mbar. A photograph is shown in Fig. 3.1 (a) and for clarity a scheme is depicted in Fig. 3.1 (b). This UHV system consists of various chambers which are separated by gate valves and have different functions:

- **Positioning chamber (PC):** The PC is the center of the system with the function of transferring up to three samples at the same time between the chambers. It hosts a manually-operated manipulator which can perform a 360° rotational movement and has an extendable and retractable arm, on which samples are placed. This chamber also hosts a commercial LEED setup.

- **Deposition chamber (DC):** The purpose of this chamber is the sample cleaning and preparation. A sputter gun is attached for sample cleaning and the samples can be heated to temperatures above 1300 K. Gas bottles and evaporators are attached to perform further sample preparation steps, like gas exposure or material deposition.

- **Analysis chamber (AC):** The AC hosts the tools for photoemission experiments. It is equipped with a hemispherical six-channeltron detector for photoelectron detection. The performance is described in detail in Ref. [49]. A twin anode X-ray source delivers non-monochromatic Mg and Si K_α radiation, with photon energies of 1253.6 eV, and 1740.0 eV respectively. Further a monochromatized Al K_α source is available with a photon energy of 1486.6 eV. A helium discharge lamp delivers light which is monochromated with a grating for ARPES and UPS experiments.

- **STM chamber:** The STM chamber hosts a room temperature STM.

- **Entry lock:** The entry lock can be vented with nitrogen, while the other chamber remain under vacuum. It is used to exchange samples.

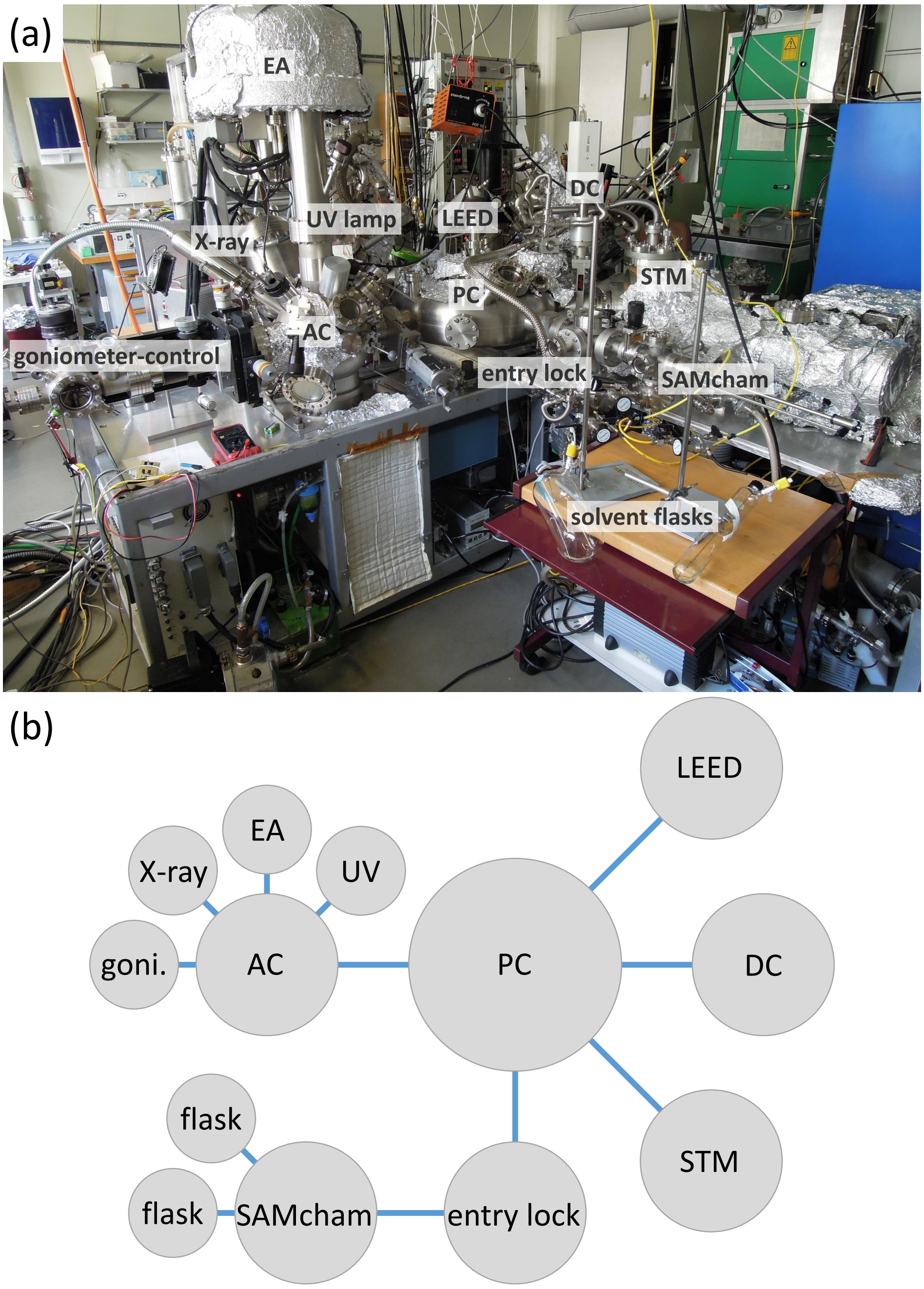

Figure 3.1: (a) Photograph of the ESCA laboratory (as of 29th May 2018). (b) Corresponding scheme.

- **SAMcham:** Within the scope of this thesis, a further chamber was added to the system to deposit SAMs on samples without exposing them to air. Two flasks are attached for SAM deposition with molecule solution and solvent for rinsing.[1] The molecule deposition is described in detail in section 5.2.

---

[1] These flasks were prepared by Mathias Mosberger (bioorganometallic & radiochemistry group, University of Zürich).

4 Ultrathin alumina films on NiAl(110)

This chapter describes the growth and structure of ultrathin alumina films grown by selective oxidation of a single crystalline NiAl(110) surface. A film with a thickness of two atomic bilayers[1] can be grown on NiAl(110), hence termed 2L-alumina within this thesis. It is among the thinnest homogenous alumina films [50]. A brief introduction to the structure of 2L-alumina/NiAl(110) and occurring defects is given. Precise control of the alumina layer thickness is important to control tunneling processes through these insulating films. Thus two methods are discussed to obtain thicker films. The high-temperature oxidation of NiAl(110) is described, with the goal to grow homogenous crystalline tunneling barrier of various thickness. The results with this method are not satisfactory. A paper is included which describes a multistep oxidation procedure for growing thicker films which are of higher quality [51]. The paper further describes structural changes occurring in thicker films and the bandstructure measured with ARPES.

4.1 Structure of 2L-alumina/NiAl(110)

Ultrathin alumina films consisting of two aluminum-oxygen-bilayers can be grown homogeneously on NiAl(110) surfaces. The growth and structure was first described by Jaeger *et al.* in 1991 [29]: The clean NiAl(110) surface is oxidized at 550 K and an alumina surface oxide forms. Subsequent annealing at 1200 K results in the crystallographic ordering of the oxide thin film [29]. It has a large unit cell and a complex nonstoichiometric structure, which was resolved by a combination of STM and density functional theory (DFT) in 2005 by Kresse *et al.* [31]. The structure of 2L-alumina/NiAl(110) is shown in Fig. 4.1 (a). The large unit cell contains 92 atoms and has a stoichiometry of $Al_{10}O_{13}$. The interfacial Al atoms bind with one electron to underlying Ni atoms and anchor with two electrons the oxide film, leading to an ionicity of $+2$ for these atoms [31]. They are arranged in pentagon and heptagon pairs [53]. The oxygen atoms in the interface layer are located

---

[1] one bilayer consists of one oxygen and one aluminum layer

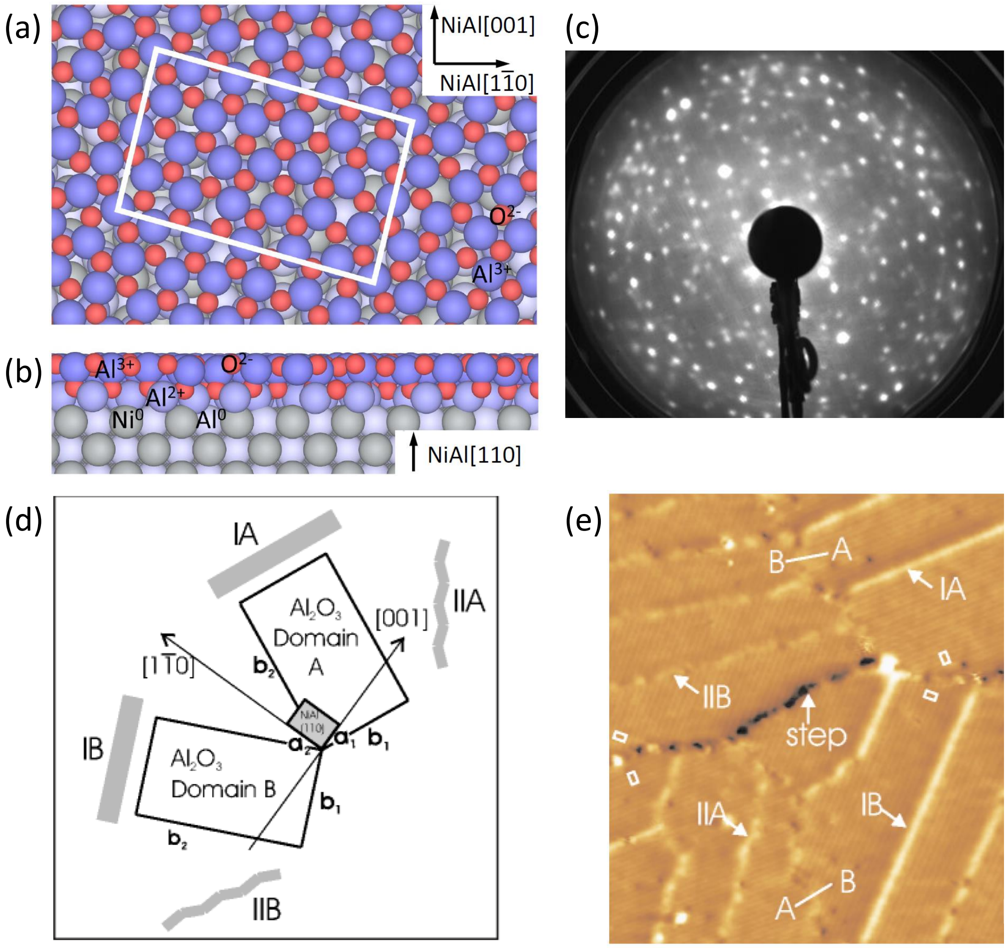

Figure 4.1: Top (a) and side view (b) of 2L-alumina/NiAl(110) based on the structural model from Kresse *et al.* [31]. Reprinted from a submitted paper [52]. (c) LEED pattern (E=67.2 eV) of 2L-alumina/NiAl(110). (d) Dimensions of 2L-alumina and NiAl(110) unit cells. Both reflection domains (A and B) are indicated. The orientation of straight (I) and zigzagged (II) antiphase domain boundaries are indicated. (e) STM of 2L-alumina/NiAl(110) showing the different line defects. The unit cell is marked in several domains as a white rectangle. (d) and (e) Modified from Kulawik *et al.* [32].

between two interfacial Al atoms. The surface Al atoms are located above the interfacial oxygen atoms. They have either three or four neighboring surface oxygen atoms, forming thus either tetrahedral or pyramidal structural units. The stacking can be described in total as $O_{s7}{}^{2-}Al_{s6}{}^{3+}/O_{i6}{}^{2-}Al_{i4}{}^{2+}$/NiAl(110), where X_s denotes atoms in the surface and X_i at the interface. The unit cell vectors enclose an angle of 89° and the mesh is rotated by 24° to the substrate [29]. Due to the symmetry of the substrate, this induces the growth of reflection domains [29], which together with the large lattice vectors cause the complex LEED pattern shown in Fig. 4.1 (c).

The 2L-alumina unit cell is commensurate along the $\left[1\bar{1}0\right]$ direction of the substrate, but

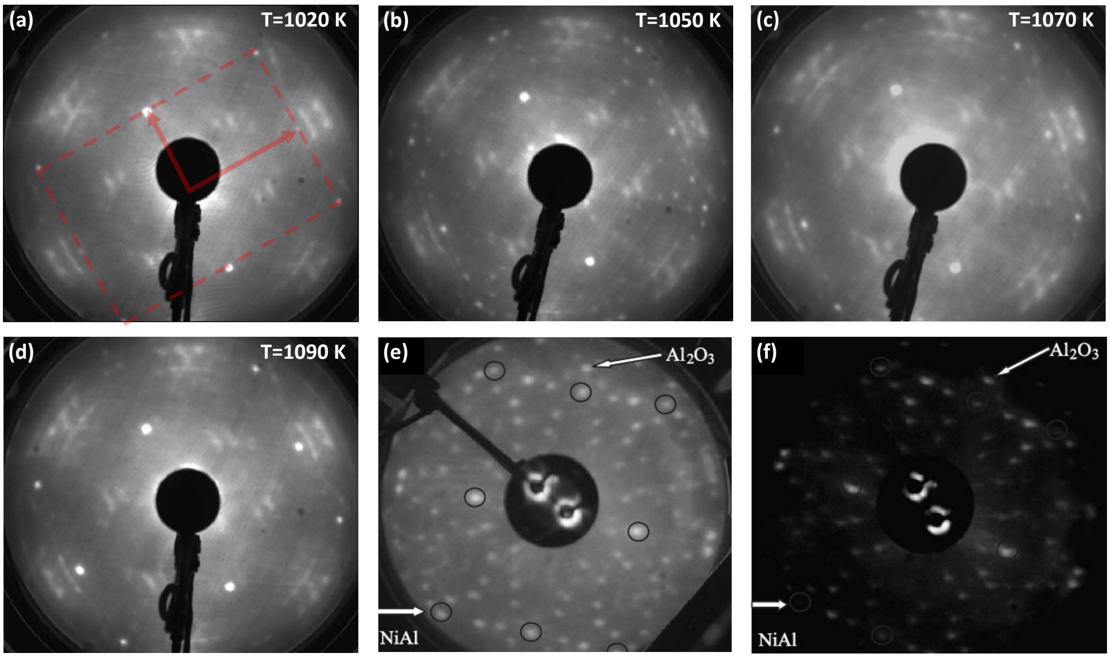

Figure 4.2: LEED pattern (E=67.2 eV) of a NiAl(110) surface oxidized at an oxygen pressure of $6.6 \cdot 10^{-7}$ mbar (dosage of 1200 L) at (a) 1020 K, (b) 1050 K, (c) 1070 K and (d) 1090 K. The surface Brillouin zone and reciprocal lattice vectors of NiAl(110)(1×1) are indicated in (a) with red. (e) LEED pattern (59 eV) of NiAl(110) oxidized at 1020 K, $6.6 \cdot 10^{-8}$ mbar, 1200 L. (f) As (e) but D=4000 L. (d) and (f) modified from Song *et al.* [54].

is incommensurate along the [001] direction [29]. This lattice mismatch and the domain boundaries cause a characteristic line defect network, as indicated in Fig. 4.1 (d) and (e). Reflection domain boundaries separate the both reflection domains and do not show a characteristic structure [32]. Two types of antiphase domains boundaries were previously observed within the same reflection domain and are the result of an additional rows of atoms [32, 33]. Antiphase domains can be straight or zigzagged [32].

4.2 High-temperature oxidation of NiAl(110)

A previously followed approach to form ordered alumina films of variable thickness is the direct high temperature oxidation of the NiAl(110) [54–57]. The NiAl(110) is exposed to oxygen at a fixed pressure and at a fixed temperature. Ordered films can be formed with that method. Crucial are the used temperature and oxygen pressure, which appear difficult to balance when a fixed pressure and temperature is used during the film growth [54–56]. For crystallization and supply of aluminum atoms from the bulk, a high temperature is required. Too high temperatures facilitate the reduction of the surface oxide and reduces the sticking coefficient of oxygen. Fig. 4.2 (a) to (d) show LEED pattern of four different preparations, where the oxidation temperature was varied systematically. Clean NiAl(110) surfaces were exposed for 40 minutes to an oxygen pressure of $6.6 \cdot 10^{-7}$ mbar at different temperatures. Fig. 4.2 (b) exhibits the sharpest LEED spots, indicating that at 1070 K the crystallinity is the highest. When comparing Fig. 4.2 (b) to a typical LEED for the in section 4.1 described low temperature oxidation with subsequent annealing (Fig. 4.1 (c)) it becomes obvious that the resulting films are of lower crystallinity.

Better results using the high-temperature oxidation have been reported by Song *et al.* [54] with lower oxygen pressures (see Fig. 4.1 (e)) [54, 55], but the crystallinity decreases for longer oxygen exposures (Fig. 4.1 (f)). Further, the growth rate is impracticable: The film from Fig. 4.1 (f) had a thickness of 1.1 nm after exposing the NiAl(110) surface to an oxygen pressure of $6.6 \cdot 10^{-8}$ mbar for more than 22 hours. To overcome this limitation and to grow thin films in an acceptable time and quality, a multistep oxidation procedure was developed.

4.3 From two- to three-dimensional alumina: Interface templated films and formation of γ-Al_2O_3(111) nuclei

The content of this section and its belonging supplementary (Appendix A.1) are published as an article[2]. The reference is in the bibliography [51]. The XPD simulation code used in this paper was improved at a later stage (Appendix A.2), which led to better quantitative results.

4.3.1 Abstract

Oxide thin films are of fundamental importance due to their applications in material science, optics, corrosion protection, catalysis, and microelectronics. A new multi-step oxidation procedure is employed to precisely tune the alumina (Al_2O_3) thickness on a NiAl(110) alloy from two atomic bilayers to 1.5 nm. Structural changes are analyzed with X-ray photoelectron diffraction and low-energy electron diffraction. The long-range order does not relate to any bulk structure and is imposed by the

---

[2] Minor changes were made to improve the readability of this section in the context of this thesis. Further, the experimental section was shifted to the end.

crystallized interface. The large unit cell formed at the interface persists in thicker films. In contrast, the local order changes at a thickness above 0.5 nm from the complex structure of this pre-layer under formation of subnanometer-sized γ-$Al_2O_3(111)$-type nuclei. The band structure is monitored with angle-resolved photoelectron spectroscopy. Increasing film thickness results in a slight decrease of the work function but does not lead to significant changes of the electronic band structure. The presented multi-step procedure opens a route for the synthesis of thin film structures in general and in particular, provides fundamental insight into the surface structure of spinel-based transition Al_2O_3.

4.3.2 Introduction

Many oxide materials are electrically insulating, which renders the characterization of their surface properties difficult with most of the surface science tools that are typically electron- or ion-based [35]. This insulating character can be overcome by studying these materials in the form of a few atomic layer thick ultrathin films prepared on conducting substrates. In heterogeneous catalysis, this approach has been used extensively in the last decades and many of these model ultrathin oxide films were studied under UHV conditions with great control [58, 59], providing fundamental insights into the structural and electronic properties of these materials [60].

However, the properties of ultrathin oxide films often deviate from their respective bulk counterparts [61], and can significantly change depending on the film thickness. This was demonstrated for gold adatoms on MgO ultrathin films epitaxially grown on Ag(100), where both the preferred adsorption site as well as the charge state can be altered by increasing the oxide film thickness [62–64]. Similar concepts also apply to molecules adsorbed on insulating ultrathin films: The gap between the highest occupied and lowest unoccupied molecular orbital as well as the charge transfer upon adsorption depend not only on polarization effects at the interface, but to a large extent also on the thickness of the insulating layer [65–67]. Catalytic activity can also change drastically in such systems: Recently it was shown that due to changes in the electronic properties the CO oxidation activity of palladium clusters deposited on alumina (Al_2O_3) films on Re(0001) strongly depends on the film thickness [68]. To fully understand which properties of the adsorbed species rely on the adsorbate/oxide interface and which are influenced by the underlying substrate material, the oxide thickness needs to be varied in a controlled manner [69].

Al_2O_3 is one of the most technologically relevant oxide materials. The stable bulk phase is α-Al_2O_3, also called corundum or sapphire. Several further metastable phases exist, e.g.

γ-, δ-, θ-, χ-, κ-, κ'- and η-Al_2O_3 [70]. γ-Al_2O_3 is of special technological importance, as it is the most frequently used catalyst support for hydrotreating [71]. Despite its relevance, the detailed structure of γ-Al_2O_3 is still under debate [70,72]. It is generally described as a defective spinel structure, however no general agreement exists on the detailed location of cation vacancies and the occupation of interstitial sites [70, 72]. Recently, the growth of well-defined crystalline (100)-oriented spinel alumina films was demonstrated on a $MgAl_2O_4(100)$ surface [73]. They deliver a satisfactory model system for spinel-based transition alumina (γ-, δ-, and η-Al_2O_3) [73], but the insulating nature of the $MgAl_2O_4$ substrate limits its application as model system.
A viable approach for the synthesis of ultrathin oxide films is based on the selective oxidation of suitable bimetallic alloys [29,74–77]. The prototypical example is an ultrathin alumina film on the NiAl(110) substrate [29,31], which has been widely used as a support in model catalytic studies [34–36,78]. This ultrathin surface oxide has an $Al_{10}O_{13}$ stoichiometry, consists of two atomic bi-layers and has a ${O_s^{2-}}_7\,{Al_s^{3+}}_6/{O_i^{2-}}_6\,{Al_i^{2+}}_4$/NiAl(110) stacking ($X_s$ and X_i refer to surface and interface species, respectively). In the following, this thin film will be denoted as 2L-alumina [31]. Its complex unit cell contains 92 atoms with Al_s bound either pyramidally or tetrahedrally, adapting a structure that cannot be clearly assigned to any bulk phase [31]. The unique structure and the non-stoichiometric nature of this 2L-alumina oxide layer recently raised questions to what extent this surface oxide could be an approximant of γ-Al_2O_3 [71]. If the thickness of the alumina film could be increased, the influence of the substrate and the interface on the surface weakens, which is expected to result in alumina films that better represent the properties of bulk Al_2O_3 phases. Several routes to increase the thickness of 2L-alumina were studied previously: It was shown that metal clusters on 2L-alumina can bind and dissociate oxygen, which then spills over from the clusters and oxidizes the bimetallic substrate [79–81]. Further, oxidizing molecules such as water [82,83] and nitrogen dioxide [84,85] were shown to adsorb, dissociate and react with subsurface aluminum atoms. Exposure to water [83] and oxygen [86] in the millibar range or atomic oxygen [85] can significantly increase the oxide thickness, but this approach does not result in ordered thin films. Previous routes for thicker crystalline films included deposition and subsequent oxidation of aluminum atoms [57] and the direct oxidation of the substrate [55]. These studies indicate the feasibility of growing ordered alumina films, but it appears to be difficult to balance the processes of oxidation, crystallization, atomic diffusion and oxide decomposition in a favorable manner at one fixed temperature and chemical potential [55,56].

In this paper, we describe a new method for the synthesis of thicker alumina films with excellent crystallinity on the NiAl(110) substrate: The as-grown 2L-alumina/NiAl(110) system is annealed in UHV at elevated temperature to ensure a high degree of crystallographic order at the interface. The oxidation is continued after this at lower temperature and higher oxygen pressures to increase the thickness and to avoid oxygen desorption. The film growth is monitored stepwise by XPS. The damping of the substrate peaks indicates the formation of a homogenous overlayer. LEED confirms excellent crystallinity. XPD reveals changes in the short-range atomic order: While increasing the film thickness, the local formation of subnanometer-sized γ-$Al_2O_3(111)$-nuclei is observed. Surprisingly, the complex surface unit cell of the 2L-alumina film [29, 31] is maintained when increasing the film thickness, implying that the new layers follow the arrangement of the interface layer. The subnanometer γ-$Al_2O_3(111)$-nuclei manifest themselves in the LEED pattern as hexagonal building blocks of octahedrally-coordinated aluminum within the 2L-alumina unit cell. A spreading of these motifs is observed with increasing thickness of the oxide film, delivering the first experimental contribution to elucidate the structure of the γ-$Al_2O_3(111)$ surface. Band structure measurements by ARPES reveal no significant changes in the electronic structure upon increasing film thickness.

4.3.3 Data and discussion

Fig. 4.3(a) shows the Al 2p and Ni 3p core level spectra for the different preparation steps during the oxide growth. The spectrum of the NiAl(110) surface exhibits the metallic Ni^0 and Al^0 peaks, to whose height all spectra are normalized. During the whole oxidation procedure these peaks and their ratios show no significant change, indicating that the supplied thermal energy is sufficient to enable diffusion inside the substrate. Oxidation of 2L-alumina films yield additional signals at higher binding energies which originate from interfacial ${Al_i}^{2+}$ and ${Al_s}^{3+}$ atoms [53]. With continued oxidation, the Al^{3+} intensity at a binding energy of 75.3 eV rises. The oxide thickness (d) is calculated by the intensity ratio of the oxidized Al species (I_O) and the metallic Al^0 peak (I_M) according to equation (1):

$$d = \lambda_O \cdot \cos(\theta) \cdot \ln\left[\frac{N_M \lambda_M}{N_O \lambda_O} \frac{I_O}{I_M \exp\left(\frac{d}{\lambda_O \cos(\theta)}\right)} + 1\right], \tag{4.1}$$

where θ refers to the electron emission angle with respect to the surface normal, λ_x to the inelastic mean free path and N_x to the density of Al atoms in the material x. Eq. (1) is similar to the one in Ref. [87] but additionally considers the observed attenuation of

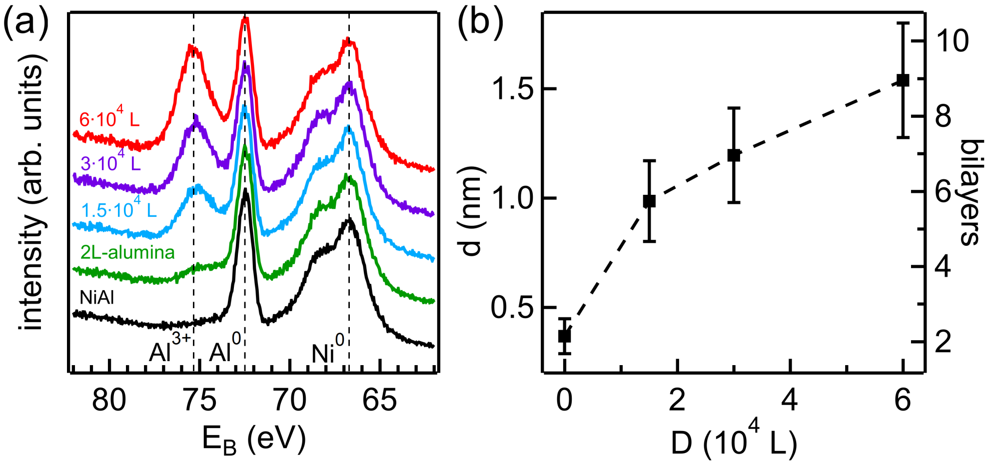

Figure 4.3: (a) Al 2p and Ni 3p core level spectra of NiAl(110), 2L-alumina/NiAl(110) and of thicker alumina films on NiAl(110). An increase of the Al^{3+} signal indicates oxide formation. (b) Increase of the alumina film thickness versus the total oxygen dosage D.

photoelectron intensity from the metal substrate below the oxide. λ_x is calculated with the TTP-2M equation [88]. Fig. 4.3(b) displays the evolution of the alumina thickness. After an oxygen dosage of $6 \cdot 10^4$ L, the film thickness increases from two atomic bilayers (0.4 nm) to nine atomic bilayers (1.5 nm). The indicated error bars are mainly attributed to uncertainties of λ_M [88]. A slight saturation behavior is observed, as the growth rate decreases according to the Cabrera-Mott theory for oxidation with increasing thickness [89]. However, a further growth beyond 1.5 nm under the used experimental conditions appears possible.

Non-normalized spectra shown in Fig. A.1 (Appendix A.1.1) illustrate the exponential attenuation of the two substrate peaks by the oxide overlayer. The resulting damping constant of 2.24 ± 0.07 nm is in good agreement with the calculated value of 2.67 ± 0.47 nm obtained from a continuous overlayer model with the inelastic mean free path from the TPP-2M equation [88, 90, 91]. This indicates a high degree of film uniformity and flatness. A strong corrugation of the film surface would lead to substantially longer damping constants.

To gain insight into the short-range order, we employ angle-scanned XPD [92]. Fig. 4.4(a) shows XPD patterns of the oxygen 1s peak from 2L-alumina and from a 1.0 nm thick film, which were recorded at the corresponding peak maxima while subtracting the spectral background (Fig. 4.4(c) right panel). Mainly forward scattering contributes at the given kinetic energy to the detected intensity modulation [92]. Due to the large unit cells involved in the system, and the concomitantly huge number of inequivalent oxygen emitter sites,

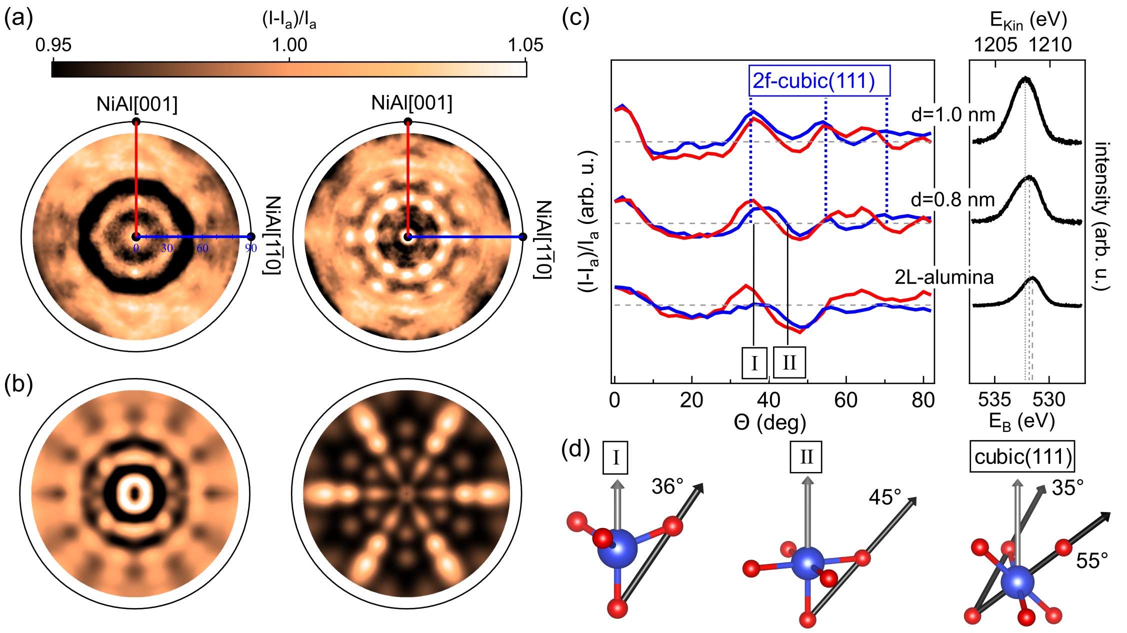

Figure 4.4: (a) Experimental O 1s XPD pattern of 2L-alumina (left) and a 1.0 nm thick film (right). (b) Forward scattering simulations of 2L-alumina (left) and γ-Al_2O_3(111) with a two-fold symmetry (right). (c) Left: Polar cuts along the $\langle 001 \rangle$ and $\langle 1\bar{1}0 \rangle$ azimuthal directions of the NiAl(110) substrate (red and blue as marked in (a) for different film thicknesses). In 2L-alumina tetrahedral (I) and octahedral (II) building blocks are present [31]. For thicker films we observe the formation of a two-fold cubic(111) structure. Right: Corresponding core level spectra. Dotted lines denote the intensity maxima. (d) Occurring building blocks as marked in (c). Oxygen and aluminum atoms are colored red and blue, respectively. The gray and black arrows indicate normal emission and forward scattering directions, respectively.

we limit the modelling of these patterns to a simple forward scattering simulation, where all interatomic vectors originating from oxygen atoms are projected onto the unit sphere and represented in stereographic projection for comparison with the experimental data. The simulation is based on the structural models from Ref. [31, 93]. The code considers a scaling of the total elastic scattering cross section as given by Browning et al. [94], an exponential intensity decrease with the distance between emitter and scatterer due to the inelastic scattering of electrons [88], and a decrease of the forward scattering amplitude with the square of the distance between emitter and scatterer. A Gaussian blur of $\sigma_\theta = 5°$ and $\sigma_\phi = 5°/\sin(\theta)$ is used for the binning of the forward scattering maxima onto the same grid of polar and azimuthal angles as used for the data acquisition. The goal of these simulations is not a perfect reproduction of the measured XPD patterns, but to qualitatively reproduce the dominating features responsible for the photoelectron intensity modulation.

When comparing these forward scattering calculations with experimental XPD data, the focus lies on the identification of dominant interatomic vectors within these highly complex surface structures.

In the case of 2L-alumina, and while neglecting weak interference fringes [41], oxygen emitters in the surface layer (O_s) should not contribute to the intensity modulation, but they contribute to the XPD pattern as scatterers. Likewise, oxygen atoms from the interface layer (O_i) contribute only as emitters and not as scatterers. Their photoelectrons undergo forward scattering off the aluminum and oxygen atoms in the surface layer (O_s and Al_s). Polar cuts for alumina films of different thickness are shown in Fig. 4.4(c). For 2L-alumina, the short-range order is dominated by tetrahedral and pyramidal building blocks [31], as shown in Fig. 4.4(d) I and II. Tetrahedrally-coordinated aluminum is also present in most bulk phases, however, the pyramidally-coordinated aluminum can be regarded as a precursor of octahedrally-coordinated aluminum [31]. For both of these building blocks, photoelectrons emitted from an O_i-atom will undergo forward scattering off an Al_s-atom on top, leading to the observed intensity increase at normal emission ($\theta = 0°$). As the blocks are highly distorted in 2L-alumina, the Al_s are placed not directly above O_i, leading to the small inner circle in the simulation (Fig. 4.4(b), left pattern). For higher thicknesses, the feature at normal emission narrows significantly in the experimental data, indicating an increased local ordering.

In an ideal tetrahedral block (I), the photoelectrons from O_i will undergo forward scattering at O_s under an emission angle of $\theta = 36°$. In the case of a pyramidal block (II), the ideal emission angle would be $\theta = 45°$. Since the building blocks in 2L-alumina are highly distorted, the scattering angles range according to the model of Kresse et al. [31] from 30° to 40° for tetrahedral blocks and from 40° to 48° for pyramidal blocks (Fig. A.2, [31]). A clear forward scattering maximum is observed at $\theta = 34°$ in the NiAl $\langle 001 \rangle$ direction (red curve), which is caused by a preferred ordering of the tetrahedral blocks. For thicker films, a further increase of this signal is observed in the measured data, indicating the presence of more or better aligned tetrahedral blocks. The forward scattering maximum due to the pyramidal blocks occurs in 2L-alumina at 44° and can be observed best along the NiAl $\langle 1\bar{1}0 \rangle$ direction (blue curve in Fig. 4.4(c) and Fig. A.2 (b) [31]).

For a 0.8 nm thick alumina film the pyramidal signature is still present in the measured data (Fig. 4.4(c)), while typical scattering angles for a cubic(111) structure start to appear and become well recognizable for the 1.0 nm thick film ($\theta = 0°$, 35°, 55° and 71°). This indicates that a critical thickness is required for the orientation change of the octahedral blocks from $\{100\}$ to $\{111\}$. In Fig. 4.5 the polar cuts of the 1.0 nm thick film from Fig. 4.4(c) are compared to forward scattering calculations of γ-$Al_2O_3(111)$ with a two-

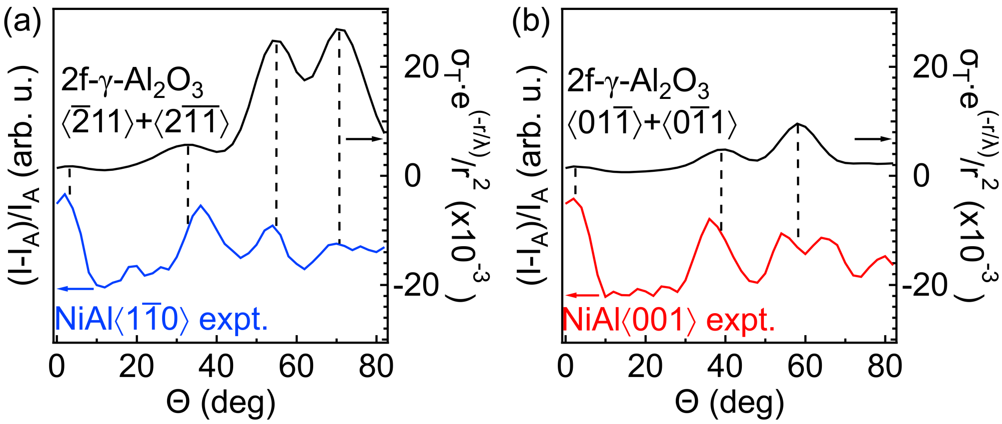

Figure 4.5: (a) O 1s polar cut of the 1.0 nm thick film along the $\langle 1\bar{1}0\rangle$ azimuthal direction of the NiAl(110) substrate (blue line, see Fig. 4.4 (c)) compared with forward scattering calculations for γ-Al$_2$O$_3$(111) with a two-fold symmetrization (black line, γ-Al$_2$O$_3\langle\bar{2}11\rangle$ and $\langle 2\bar{1}\bar{1}\rangle$ direction). (b) Corresponding polar cut along the $\langle 001\rangle$ azimuthal direction of the NiAl(110) substrate (red line, see Fig. 4.4 (c)) compared with forward scattering calculations for γ-Al$_2$O$_3$(111) with a two-fold symmetrization (black line, γ-Al$_2$O$_3\langle\bar{1}10\rangle$ and $\langle 1\bar{1}0\rangle$ direction).

fold symmetrization (Fig. A.3 (b) [93, 95, 96]), which shows a better agreement than α-Al$_2$O$_3$(0001) (Fig. A.3 (c), [93,95,96]). The scattering features of the γ-Al$_2$O$_3$ $\langle\bar{2}11\rangle$ and $\langle 2\bar{1}\bar{1}\rangle$ direction appear along the $\langle 1\bar{1}0\rangle$ azimuthal direction of the NiAl(110) substrate (Fig. 4.5(a)), and scattering features of the γ-Al$_2$O$_3$ $\langle\bar{1}10\rangle$ and $\langle 1\bar{1}0\rangle$ direction are visible along the $\langle 001\rangle$ azimuthal direction of the substrate. The maximum at $\theta = 64°$ can be attributed to an interference fringe [41].

After the orientation change of the octahedral blocks, the short-range order is thus best described as γ-Al$_2$O$_3$(111)-like. Forward scattering maxima along the $\langle 1\bar{1}0\rangle$ azimuthal direction of the NiAl(110) substrate (Fig. 4.5(a)) match well with those predicted for the bulk material. Differences between predicted and measured scattering angles might be attributed to further unconsidered bonds, interface induced distortion, surface relaxation or reconstruction. Further it should be noted that the measured intensity anisotropies become significantly smaller for bigger polar angles θ. A reduced order between photoelectron emitters and scatterers in larger distance is a reasonable interpretation, indicating the formation of small γ-Al$_2$O$_3$(111)-nuclei.

The complex structure of the 2L-alumina film was previously resolved by using scanning tunneling microscopy and ab-initio density functional theory [31]. Compared to the NiAl(110) substrate, the film has large unit cells and grows in two rotational domains as shown in Fig. 4.6(a). The large real space lattice vectors of 2L-alumina lead to comparably small reciprocal lattice vectors. A complex LEED pattern shown in Fig. 4.6(b) is the result.

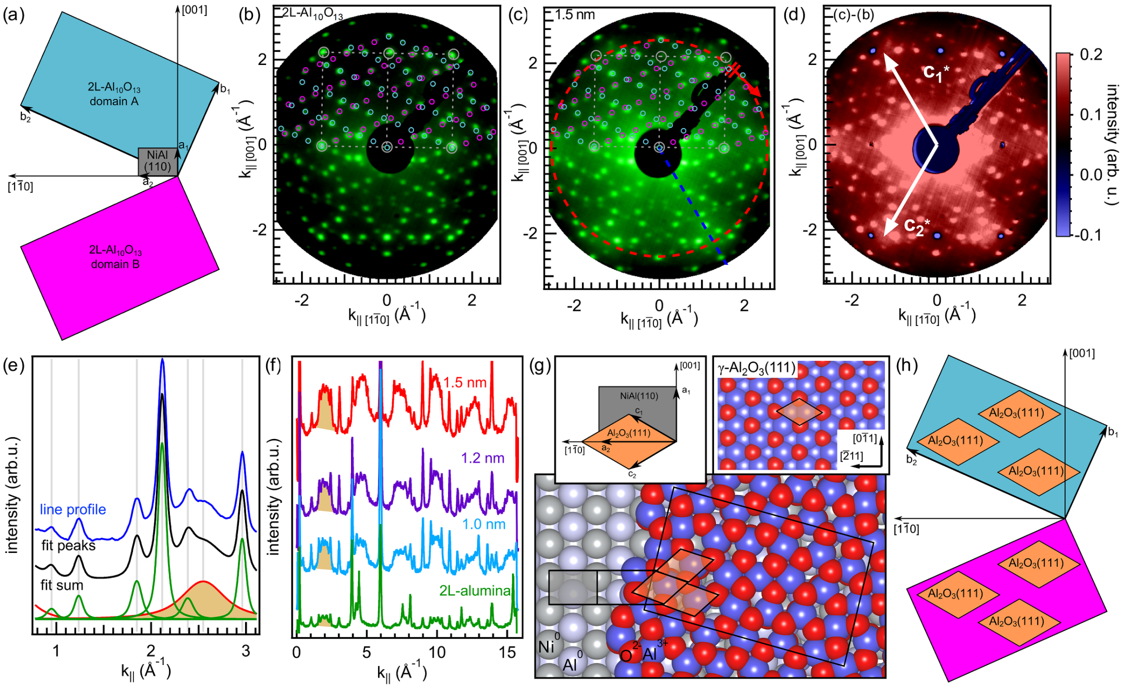

Figure 4.6: (a) Dimension and domains of the 2L-alumina surface unit cell with respect to the NiAl(110) substrate ($a_1 = 2.89\,\text{Å}$, $a_2 = 4.08\,\text{Å}$, $\sphericalangle(a_1, a_2) = 90°$, $b_1 = 10.6\,\text{Å}$, $b_2 = 17.9\,\text{Å}$, $\sphericalangle(b_1, b_2) = 88.6°$, $\sphericalangle(a_2, b_2) = 24.1°$ [30]). (b) LEED pattern of 2L-alumina/NiAl(110). The theoretical pattern is indicated in the top half, with red and blue circles representing spots of the two domains as defined in (a). (c) LEED pattern of a film with a thickness of 1.5 nm. (d) Intensity difference pattern between (c) and (b). We observe an intensity decrease (blue) of the NiAl(110) substrate spots as well as a signal gain (red) belonging to the 2L-alumina pattern and a new and diffuse hexagonal structure. Reciprocal lattice vectors of the hexagonal phase are indicated. (e) Line profile (blue) as marked in (c) with blue dashed line and corresponding fit (black). Green fit peaks belong to the large 2L-alumina unit cell. The broad orange-shaded peak is attributed to the hexagonal structure with a maximum at $k_\| = 2.55\,\text{Å}^{-1}$. (f) Line profiles along the dashed red circle in (c) for $\sqrt{k^2_{\|001} + k^2_{\|1\bar{1}0}} = 2.55\,\text{Å}^{-1}$ for different thicknesses. The hexagonal structure exhibits broad peaks (one is shaded in orange), indicating domain sizes on the sub-nanometer scale. Furthermore, numerous sharper peaks are visible belonging to the 2L-alumina pattern. (g) Model of the hexagonal structure based on the 2L-alumina/NiAl(110) structure of Ref. [31]. The left inset shows the found unit cell with respect to the substrate. The right inset shows a model of γ-Al$_2$O$_3$ terminated along the [111] direction. (h) Structural model of the thin film after the orientation change of the octahedral blocks and the formation of γ-Al$_2$O$_3$(111) nuclei.

The LEED pattern of a film with a thickness of 1.5 nm is shown in Fig. 4.6(c) and indicates that the symmetry of the 2L-alumina is maintained. The peak width does not change markedly, indicating that domain sizes in the homogeneous film do not change. In addition, a blurred hexagonal structure is observed. Fig. 4.6(d) shows the difference of the normed intensities between Fig. 4.6(c) and Fig. 4.6(b). A marked intensity decrease is observed for the NiAl(110) (1×1) contribution, as the substrate is buried beneath a thicker oxide layer. An intensity enhancement is observed for the 2L-alumina lattice, which suggests that an increasing number of atoms form the corresponding unit cell. Further, the new hexagonal structure also contributes to the intensity gain, with reciprocal lattice vectors $\vec{c}_1{}^*$ and $\vec{c}_2{}^*$ indicated in Fig. 4.6(d).

Fig. 4.6(e) shows the line profile and a fit along the blue dashed line of Fig. 4.6(c). Several narrow peaks associated with the 2L-alumina unit cell are visible (green), and a comparatively broad peak (orange shaded) associated with the hexagonal structure. The reciprocal lattice constant is $k_{\|} = 2.55 \pm 0.02\,\text{Å}^{-1}$, resulting in a real space lattice plane distance of $2.46 \pm 0.02\,\text{Å}$ and a lattice constant of $2.85 \pm 0.02\,\text{Å}$. The fact that the peak of the hexagonal structure is rather broad indicates that the respective structural domains are on the sub-nanometer scale. Fig. 4.6(f) displays circular line profiles as marked in Fig. 4.6(c) by the red dashed line $\left(\sqrt{k^2_{\|001} + k^2_{\|1\bar{1}0}} = 2.55\,\text{Å}^{-1}\right)$ for different oxide thicknesses. Numerous narrow peaks from the 2L-alumina structure are visible in all line profiles. Further six broad peaks are visible due to the hexagonal structure, with the sixth peak partly obstructed by the electron gun. This structure is visible for all examined thicknesses and can even be traced back to the 2L-alumina film, indicating that it is part of the bigger unit cell. By considering the known structure of 2L-alumina [31], we attribute the hexagonal structure to a surface unit cell with one tetrahedrally-bound Al_s atom and one O_s as depicted in Fig. 4.6(g).

Smrčok et al. [93] proposed a model of the bulk γ-Al_2O_3 structure. We find a possible planar section along the [111] direction with an average oxygen-oxygen distance of 2.81 Å, as shown in the right inset of Fig. 4.6(g). The measured hexagonal structure shows a lattice constant between the one of the substrate and the one implied by the bulk oxide. Like the overall crystal structure, the structures of the low index surfaces of γ-Al_2O_3 are still discussed controversially in literature [71, 97] and based mostly on theoretical work [98–100]. According to the authors' knowledge, this is the first experimental evidence towards an atomistic understanding of the γ-Al_2O_3(111) surface. Fig. 4.6(h) depicts the structural motifs of the thin film after the orientation change of the octahedral building blocks: The local ordering can be best described by subnanometer-sized γ-Al_2O_3-nuclei. These nuclei are formed inside of the homogenous film and are arranged as parts of a bigger unit cell. This unit cell is the same as in the case of 2L-alumina and is thus implied by the interface.

In a recent study an anomalous hexagonal superstructure of alumina was found by scanning tunneling microscopy after two cycles of oxidation of 2L-alumina at 550 K and annealing at 920 K [101]. Krukowski et al. [101] found a hexagonal arrangement with a periodicity of 2.7 ± 0.2 Å. The similar lattice constant indicates that this structure is closely related to the hexagonal structure we identified in Fig. 4.6. A different approach for growing alumina thin films of variable thickness on NiAl(110) is the direct oxidation of the substrate at the annealing temperature [54, 55], but it appears to be difficult to balance the processes of oxidation, crystallization, atomic diffusion and oxide decomposition in a favorable manner at one fixed chemical potential and temperature. High temperatures are required for sufficient diffusion of Al-atoms in the substrate [75] and for crystallization. However, thicker films might not be stable at a given temperature, as the adhesion energy at the interface provides extra stabilization [102]. This interface energy on the other hand increases the crystallization temperature of thinner film [103]. Our approach combines both of these principles: The 2L-alumina system and thus the interface is crystallized at higher temperature. After this, thicker films are grown at lower temperature where they are more stable and the crystallization energy is lower. The thermal energy is still sufficient to allow atomic diffusion and to avoid Al depletion in the substrate.

Fig. 4.7(a) shows ARPES data measured on 2L-alumina and on a 1.5 nm thick film. Energy distribution curves for substrate and alumina films of different thicknesses at the high symmetry points of the substrate surface Brillouin zone (SBZ) are displayed in Fig. 4.7(b). 3d states of the NiAl(110) substrate appear at $E - E_F < 4\,\mathrm{eV}$ [29, 104]. After oxidation, additional states appear at $E - E_F > 4\,\mathrm{eV}$ forming the valence band of alumina, which are mainly of antibonding oxygen 2p character [105, 106]. The measured band structure of 2L-alumina is in good agreement with previously published work [29]. Rather weak dispersions indicate comparably localized states. The valence band maximum of 2L-alumina is formed by a state of low spectral weight, best recognizable in the energy distribution curves recorded at the $\bar{Y}$ and $\bar{X}$ points of the substrate SBZ. The corresponding peak maximum is located with the 2^{nd} derivative in energy at $E - E_F = -4.7(9)\,\mathrm{eV}$ and no clear dispersion is observed (Fig. A.4). As the valence band has a higher spectral weight at the $\bar{Y}$-point, the peak onset was determined at this position and is found to be $E - E_F = -4.2(4)\,\mathrm{eV}$ (Fig. A.5 (a)). According to Krause et al. [107] this value describes the position of the valence band maximum, since it represents the fully relaxed state of the system. Previous work located the valence band onset at $E - E_F = -4.5\,\mathrm{eV}$ [91], but did not consider this state. Changes in the spectral weight are observed for thicker films,

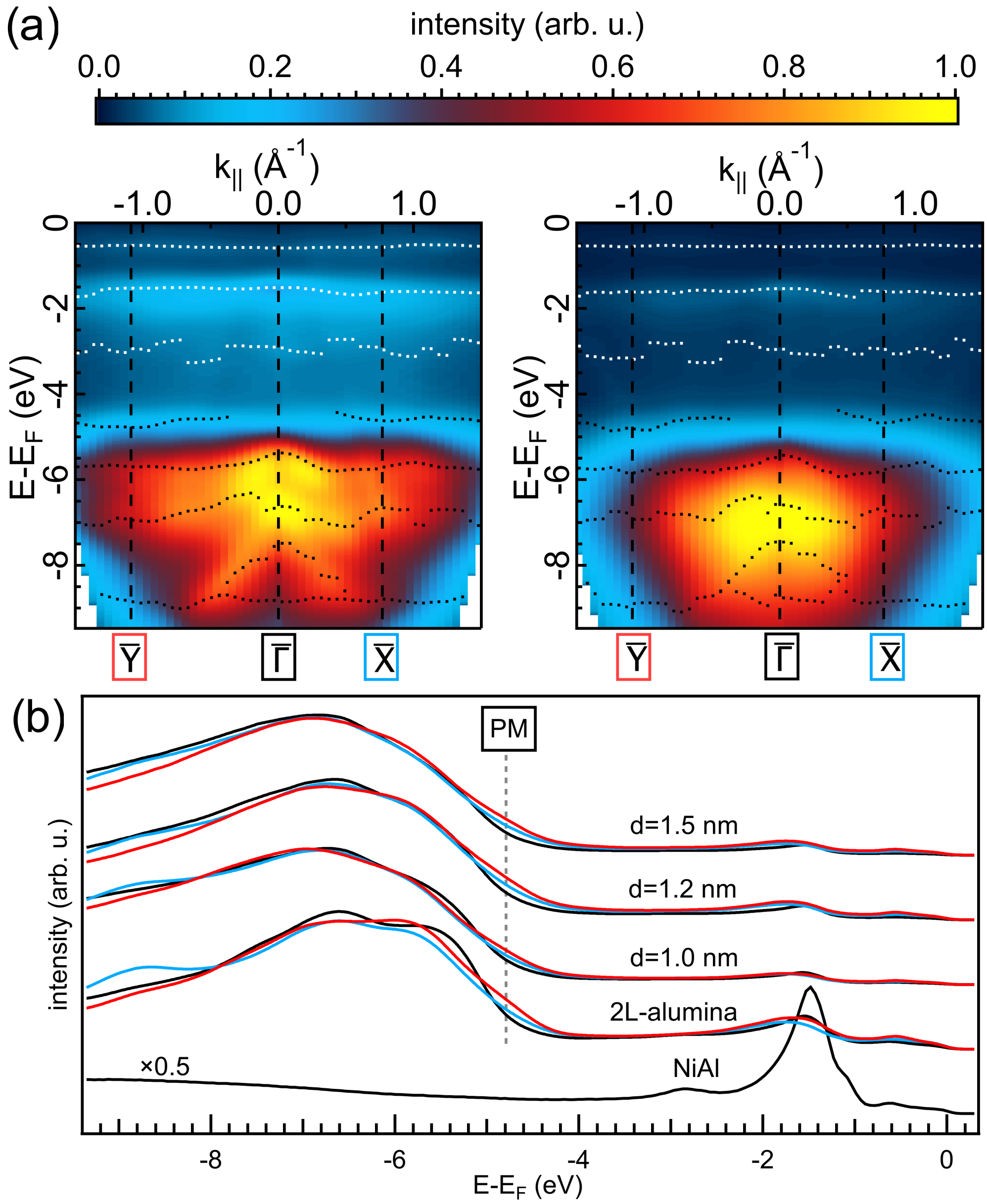

Figure 4.7: (a) ARPES data from 2L-alumina (left) and from a 1.5 nm thick film (right). Identified bands of the NiAl(110) substrate and of alumina (obtained by following local minima in the 2nd derivative in Fig. A.4) are marked with white and black dots, respectively. (b) Energy distribution curves (normalized to their integral) at $\bar{\Gamma}$ (black), $\bar{Y}$ (red) and $\bar{X}$ (blue) of the substrate surface Brillouin zone. The peak maximum (PM) of the valence band with minimum binding energy is indicated by a gray dashed line.

however within the experimental resolution no new bands are observed. The change of the valence band onset while increasing the thickness to 1.5 nm is 0.08 ± 0.09 eV (Fig. FigSuppWorkfunction (a)) and thus negligible. A slight work function decrease from

$\phi = 4.1(6)\,\mathrm{eV}$ to $\phi = 3.9(3)\,\mathrm{eV}$ is observed (Fig. FigSuppWorkfunction (b)). In total, we conclude that despite of the structural changes, increasing the film thickness does not change the valence band structure markedly. This finding is of particular interest for the application of ultrathin alumina as a controlled tunneling barrier in prospective two-dimensional devices [108, 109], especially when considering the recently demonstrated PMMA-assisted transfer of Al_2O_3-layers for highly stretchable and transparent transistors [110].

4.3.4 Summary

In summary, a new multi-step oxidation procedure is used to increase the thickness of 2L-alumina from two atomic layers to 1.5 nm. The resulting films are homogeneous and show excellent crystallinity. The large unit cell of 2L-alumina is maintained in the observed thickness range, indicating the fundamental importance of the interface for the ordering of successive layers. The atomic short-range order changes while adding additional atomic layers: Octahedral building blocks change their crystallographic direction from $\{100\}$ to $\{111\}$, indicating the formation of subnanometer-sized γ-$Al_2O_3(111)$-nuclei arranged as compartments of the bigger 2L-alumina unit cell. Despite of the structural changes, we find that while increasing the film thickness the band structure does not change significantly. First experimental evidence towards a surface model of γ-$Al_2O_3(111)$ is provided here by interpreting a hexagonal surface structure in the LEED pattern based on the 2L-alumina structure and finding structural analogies to γ-Al_2O_3. The resulting alumina films can be used as tunneling barrier in model studies, serve as substrate to study the γ-$Al_2O_3(111)$-adsorbate interaction and to elucidate the effect of the metal substrate on catalytic processes. The sequential preparation of the interface and the following layers opens a route to synthesize previously unknown thin film structures.

4.3.5 Experimental

The experiments were conducted in a modified VG ESCALAB 220 UHV system with a base pressure of $2 \cdot 10^{-10}\,\mathrm{mbar}$ [49]. The 2L-alumina films were prepared by oxidizing the clean NiAl(110) surface in $5 \cdot 10^{-6}\,\mathrm{mbar}$ oxygen at 530 K and subsequent annealing in UHV at 1150 K. The thickness of the thin films was increased systematically by oxidation in $10^{-5}\,\mathrm{mbar}$ oxygen at 1050 K. Thicker films were grown at the same temperature, but at an oxygen pressure of $2 \cdot 10^{-4}\,\mathrm{mbar}$. LEED was performed with a kinetic energy of $E =$

64.5 eV. XPS measurements were carried out at normal emission with a monochromatized Al Kα source, providing photons with an energy of h$\nu = 1486.6$ eV. The energy scale was calibrated as described in [111]. XPD patterns were collected with a non-monochromatic Si Kα source (h$\nu = 1740.0$ eV). The angle-resolved valence band spectra have been recorded with a helium discharge lamp (He I$_\alpha$, h$\nu = 21.2$ eV).

5 Functionalization of ultrathin alumina films on NiAl(110) with self-assembled monolayers

The next step for building the dye/alumina/NiAl(110) heterostructure is the deposition of dye molecules. Common techniques for molecule deposition are evaporation, electrospray deposition or SAM deposition from a solvent. Complex molecules like dye molecules can be prone to pyrolysis, which discards evaporation as a possible deposition technique[1]. Electrospray deposition is a promising technique for the deposition of large molecules and compatible with the UHV standard [112, 113]. Further the deposition of the N3 ruthenium dye (*cis*-diisothiocyanato-bis(2,2'-bipyridyl-4,4'-dicarboxylic acid) ruthenium(II)) with this method was previously reported [114]. However, major drawbacks of this method are possible damage of the molecules during the deposition [113] and inhomogeneous covering on the sample [112]. A reliable low-tech technique is the deposition as a SAM from a solvent, which is here the method of choice. The conventional SAM deposition requires it to take the sample out of the UHV-system and dip it into solution. It will be shown that this procedure leads to uncontrolled oxidation of the 2L-alumina/NiAl(110) system. A dedicated vacuum chamber is described, which enables the SAM deposition from purified solvent without exposing the sample to air. This method for molecule attachment can be extended to a broad class of molecules vulnerable to pyrolysis and presents an elegant method for attaching molecular layers on solid substrates that are sensitive to air. Fig. 5.1 shows the resulting 2D-heterostructure.

Content of this chapter and the belonging supplemental material (Appendix B) are submitted as an article [52].

---

[1] The evaporation of the rhenium dye [Re(NCS)$(CO)_3$(bipy)] was tried, but the molecule decomposed during the attempt. The deposition of [Re(OTf)$(CO)_3$(bipy)] was demonstrated together with Arian Sanusi within his semester project.

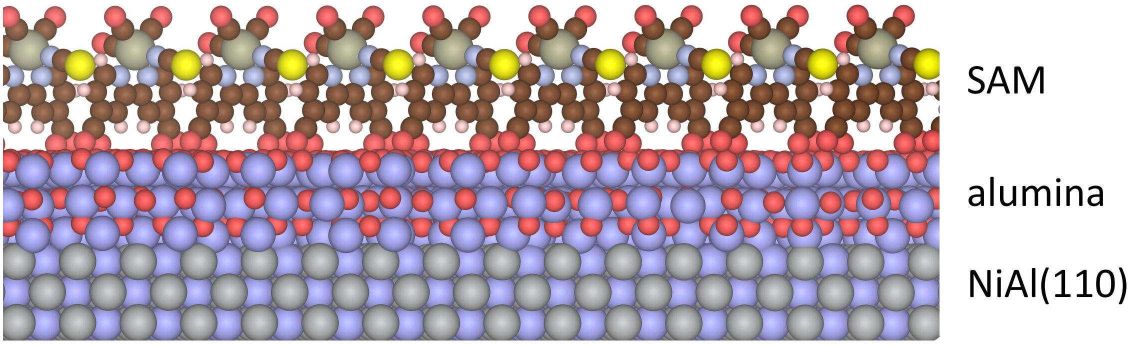

Figure 5.1: Scheme of the SAM/alumina/NiAl(110) heterostructure with rhenium dyes as SAM.

5.1 Introduction

Two-dimensional materials and atomic scale engineering allow the fabrication of a new plethora of heterostructures with exciting prospects in fundamental science and application [115–117]. A versatile method to integrate molecular building blocks into functional devices is surface and interface modification with SAMs [118, 119]. Numerous applications exist in various fields, *e.g.* sensor technology [120, 121], electrochemistry [122, 123], catalysis [124], electronic devices [125, 126] and doping of 2D-materials [127–130]. Another surface and interface modification commonly used in heterostructures are insulating ultrathin oxide films of few atomic layer thickness. They attained significant attention as tunnel junctions at interfaces [131–133], and on crystalline metal substrates as model systems for catalysis under UHV conditions [34, 36, 58, 59, 78]. Controlled oxidation of suitable metallic substrates is a viable approach for the growth of such ultrathin oxide films [29, 34, 51, 74, 75, 77, 134]. Unfortunately, not all oxide structures produced under UHV are stable under ambient conditions [83, 135–137]. As a prototypical example, ultrathin alumina films on NiAl alloys are prone to uncontrolled oxidation when exposed to ambient conditions [83, 135–137], thus limiting the scope for applications of ultrathin films with controlled thickness.

In this report, we present a procedure that overcomes this limitation by attaching a dedicated SAM deposition chamber (SAMcham) to our UHV system. It contains two stainless steel bowls that can be filled with the intended SAM solution and with the pure solvent for rinsing, and it allows direct transfer to and from UHV without contact to air. As an example, we demonstrate the immobilization of a rhenium tricarbonyl type chromophore containing a 2,2'-bipyridine-4,4'-dicarboxylic acid (DCO_2bipy) for surface binding on a well ordered ultrathin alumina film and characterize it with XPS. A passivating effect due to the SAM is observed.

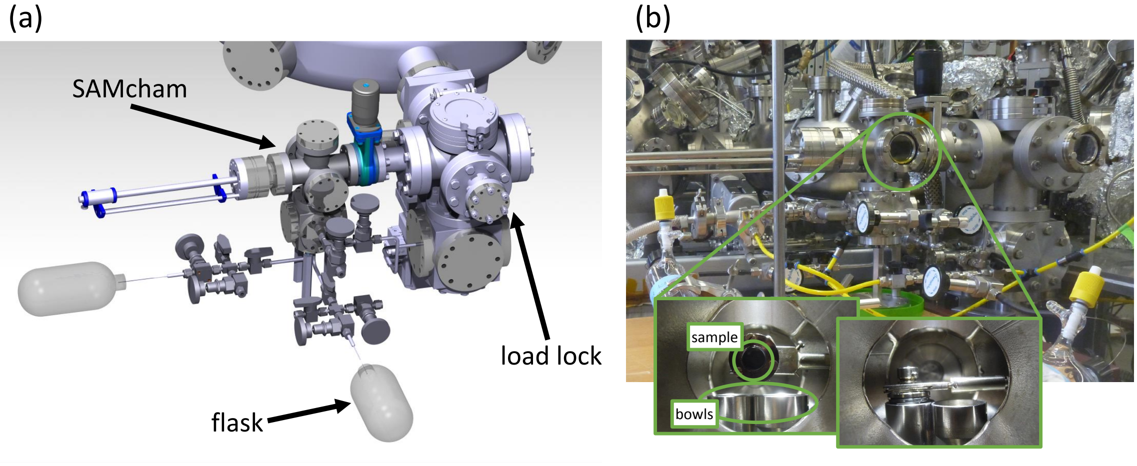

Figure 5.2: (a) Computer-aided design drawing of the SAMcham. (b) Photograph of the SAMcham. The insets show the inside of the chamber, containing the two bowls for SAM deposition and sample rinsing. A sample is placed with the wobble stick inside the left bowl.

Diimine rhenium(I) tricarbonyl complexes are synthetically versatile photo- and redox-active compounds, which can be incorporated into supramolecular systems, polymers, biomolecules [138–140], and efficient photocatalytic systems for CO_2 reduction [141, 142] as well as H_2 production [143–145]. A derivative of the previously studied *fac*–[Re(NCS)$(CO)_3$(diimine)] (diimine = 2,2'-bipyridine (bipy)) [144, 146, 147] featuring carboxyl linker groups is employed as SAM on the 2L-alumina.

5.2 *In vacuo* SAM deposition

The samples are transferred from the UHV system via the load lock to the SAMcham (Fig. 5.2)[2]. The pressure in the SAMcham is in the range of 10^{-6} mbar during the sample transfer. Two flasks are attached via needles to the setup: One with a 0.1 mM solution of the molecule dissolved in acetonitrile for SAM deposition, and one with pure acetonitrile for sample rinsing. When opening the connecting valves between flask and SAMcham, the solvent is pressed into the SAMcham and can splash on the sample. During this procedure, the vapor pressure is established in the chamber. After molecule deposition, the chamber is pumped down again, and the sample is transferred back into the UHV system. XPS

---

[2] The connection to the entry lock was changed at a later stage for better accessibility, as can be seen in Fig. 3.1.

indicated in first experiments a silicon contamination, which can be avoided by using teflon-coated septa for the solvent flasks.

5.3 Results and discussion

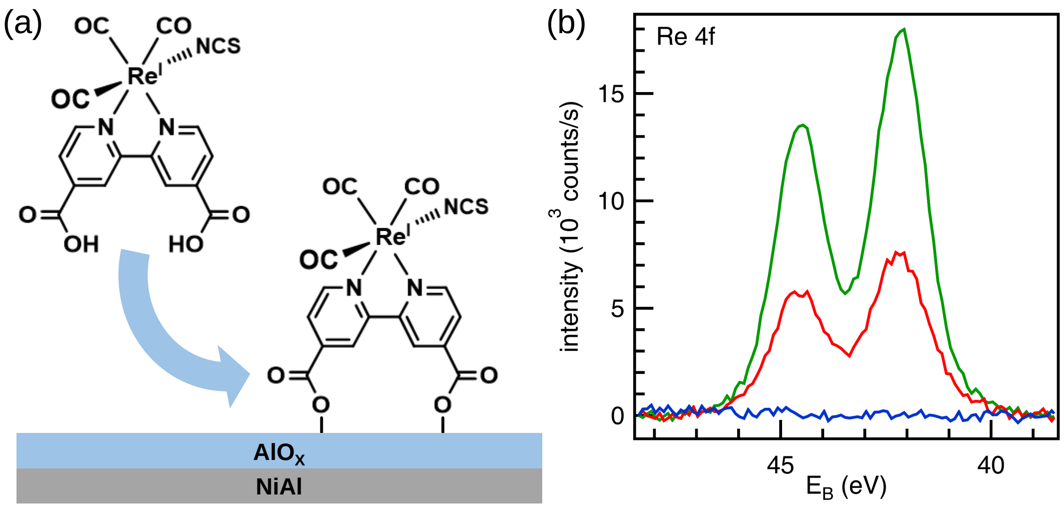

Figure 5.3: (a) Structure of *fac*-[Re(NCS)(CO)$_3$(DCO$_2$bipy)] featuring two carboxyl linker groups and scheme of molecule anchoring onto the alumina thin film. The carboxyl groups of the molecule bind to the oxide surface. (b) Re 4f core-level spectra before (blue) and after solvent deposition of the photosensitizer (green). After rinsing (red), the chemisorbed monolayer remains on the sample.

The scheme in Fig. 5.3 (a) shows the structure of the used derivative of *fac*-[Re(NCS)(CO)$_3$(DCO$_2$bipy)] featuring carboxyl linker groups in the 4 and 4’ position of the bipy system and pictures the simplified attachment of the photosensitizer onto the ultrathin oxide film. After the preparation of the 2L-alumina thin films in our UHV system, the sample is brought to the SAMcham while maintaining a high vacuum standard. Two flasks with molecule solution and solvent are connected to the chamber via needles and valves. When the valve between SAMcham and flask is opened, the liquid is pressed inside onto the sample, and the vapor pressure is established in the chamber. After this procedure, the solvent is pumped out of the chamber. Fig. 5.3 (b) shows the XPS of the Re 4f peak of the clean 2L-alumina (blue), directly after the molecule deposition from acetonitrile (green). Rinsing of the sample removes physisorbed molecules and only the chemisorbed monolayer remains (red). For the multilayer, the intensity of the Re 4f peak is 2.4 times higher. This value gives a lower estimate for the number of layers in

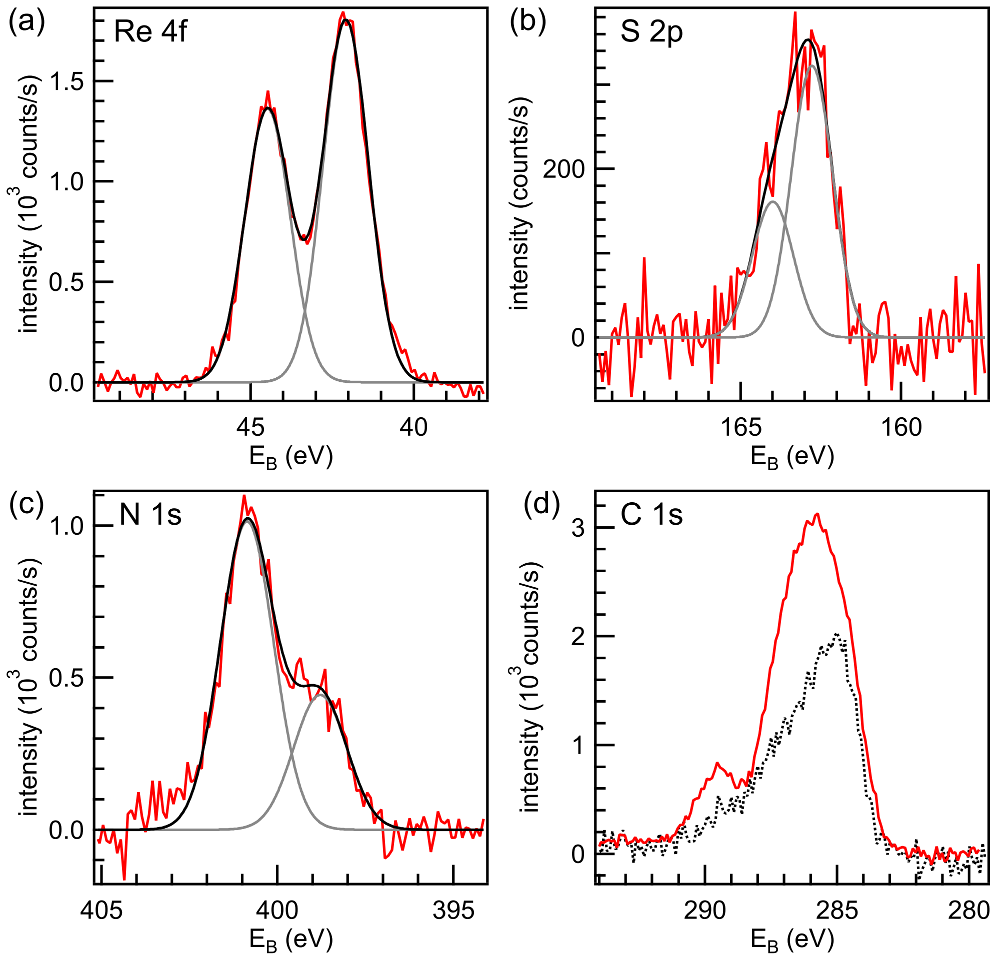

Figure 5.4: XPS of the SAM (red): (a) Re 4f, (b) S 2p, (c) N 1s (difference spectrum), and (d) C 1s. Fits (black and gray) indicate the spin-orbit splitting of the Re 4f and S 2p peaks, and the two components of the N 1s peak. The black dashed line in (d) shows the C 1s contamination which occurs if 2L-alumina is rinsed in acetonitrile without molecules.

the multilayer, neglecting the scattering of photoelectrons within the molecules. After rinsing, the rhenium coverage is (1.29 ± 0.28) atoms/nm^2. Considering the dimensions of the molecule, this indicates the formation of a dense monolayer.

Fig. 5.4 shows the (a) Re 4f, (b) S 2p, (c) N 1s, and (d) C 1s core-level spectra of a SAM prepared in this way. For the N 1s peak the difference spectrum using a normalized spectrum of clean 2L-alumina is plotted, as a Ni LMM Auger line occurs in this region with the used Mg Kα X-ray source. The photosensitizer has a chemical formula of $C_{16}H_8N_3O_7ReS$. It contains one rhenium atom in the center, one sulfur atom in the axial thiocyanate ligand and three nitrogen atoms, two of them in the bipy and one in the axial thiocyanate ligand. The binding energies and the stoichiometry of the molecule are summarized in Table 5.1 and refer to data recorded before radiation damage alters the spectra. Radiation damage of the molecule is observed during the photoemission experiments and discussed in detail in the Supplemental material (see Appendix B.1). The stoichiometry of the constituting components is obtained from integrated intensities divided by the respective photoionization cross-sections [148] and is normalized to the Re 4f peak (see Table 5.1). The main source for the errors is attributed to uncertainties in the photoionization cross-sections, which can deviate up to 20 % in molecules due to intramolecular inelastic scattering processes and multielectron excitations [149]. An excess of nine carbon atoms is observed, compared to the 16 carbon atoms of the molecule. The dashed black line in Fig. 5.4 (d) indicates the effect of a preparation with pure solvent, but without molecules (spectrum scaled to the same substrate intensity). Several carbon species are found on the sample when the sample leaves the UHV. Binding energies between 284 and 290 eV are observed, indicating the formation of carbon bonded to oxygen (286 to 291 eV) and other carbon atoms (285 eV) [150]. Bonding of carbon to aluminum would lead to the formation of carbides (282 eV), which is not observed. We conclude that the observed excess carbon is most likely due to carbon species on the oxygen-terminated alumina surface, but other origins and locations of the remaining carbon cannot be excluded. The binding energy of 162.7 eV of the S $2p_{3/2}$ is in good agreement with the binding energy found for thiocyanate in the N3 dye on 2L-alumina/NiAl(110) [151], indicating that here similarly the thiocyanate group is not involved in the bonding. Thiocyanate involved in bonding to the substrate delivered in the case of the N3 dye on $TiO_2(110)$ an additional contribution at 0.7 eV higher binding energies [114]. Also, the here found binding energies of 400.9 and 398.8 eV for the nitrogen in the bipy and in the thiocyanate compare well to the binding energies observed in N3/2L-alumina/NiAl(110) [151]. The carbon peak contains a multitude of contributions due to contamination and a great number of carbon species inside the molecule, however the carboxyl groups at a binding energy of 289.4 eV can unambiguously be identified. In total, these results show that the molecules undergo the deposition procedure undamaged and attach to the surface via the carboxyl groups.

Fig. 5.5 (a) shows the Shirley background-subtracted Al 2p and Ni 3p spectra of the clean NiAl(110) substrate (black) with the metallic peaks. The spectra are normalized to the average height of the metallic aluminum peak (Al^0) and the metallic nickel peak (Ni^0). After growing the 2L-alumina film (blue) additional contributions are observed at higher binding energies due to the presence of Al^{2+} in the interfacial oxide layer and Al^{3+} in the second layer (blue) [29,53]. The shaded area indicates the difference to the bare NiAl(110) substrate. During SAM deposition with short transfer through the air (magenta), a significant intensity increase of oxidized aluminum is observed, corresponding to a thickness of

Table 5.1: Binding energies measured by XPS, the atomic ratios (obtained from integrated peak intensities and divided by the respective photoionization cross-sections), and comparison to the stoichiometry of the molecule.

corelevel	E_B (eV)	ratio to Re	expected stoichiometry
Re $4f_{7/2}$	42.1	1.0	1
S $2p_{3/2}$	162.7	0.93 ± 0.19	1
N 1s	400.9	2.3 ± 0.5	2
	398.8	0.99 ± 0.21	1
C 1s	-	25 ± 5	16

four atomic layers. The shaded area indicates that a significant intensity decrease occurs for the Al^0 peak, and an increase for the Ni^0 peak. This can be explained by depletion of metallic aluminum at the interface during the oxide formation. As a consequence, a higher amount of metallic nickel is left at the interface. These effects are reduced when SAM deposition is accomplished by *in vacuo* (red) in the dedicated SAMcham. Here, the alumina thickness changes only by one atomic layer and the aluminum depletion and nickel enrichment at the interface are significantly reduced. At a later stage, it was possible to reduce this uncontrolled oxidation to half an atomic layer due to the use of two septa in the flask lid (Fig. 6.2).

The reaction of 2L-alumina with water vapor was previously studied by Shavorskiy *et al.* [83] using ambient pressure X-ray photoelectron spectroscopy. It was found that relative humidities above 0.01 % lead to a drastic increase of the oxide thickness, and to aluminum depletion as well as nickel enrichment in the near surface region. When the SAM deposition is done with a transfer through the air (Fig. 5.5 (a), magenta), a similar change of the surface region is observed. These authors further observed a small thickness increase at a relative humidity of 10^{-5} %, associated with surface hydroxylation/oxidation at defect sides of the film present due to reflection and antiphase domain boundaries [30, 32, 33]. For straight antiphase domain boundaries an oxygen-deficiency was proven, making it very favorable adsorption sides for new oxygen atoms [33]. In the case with sample transfer through air, the oxygen can originate from the atmosphere. In the case of the *in vacuo* SAM deposition oxygen might come from the solvent. The molecule attachment can also promote the oxidation of further aluminum atoms: Formation of aluminum-oxygen-carbon bonds are a viable scenario during the molecule attachment [152–154]. In the case of hydroxylated alumina surfaces chemisorption of carboxyls will occur via an esterification-like reaction, which releases water molecules [152–155]. Here, the chemisorption of the carboxyl groups on the 2L-alumina surface might also release hydroxyls or water and oxidize the aluminum film further. A shift of the oxygen 1s peak to higher binding energies

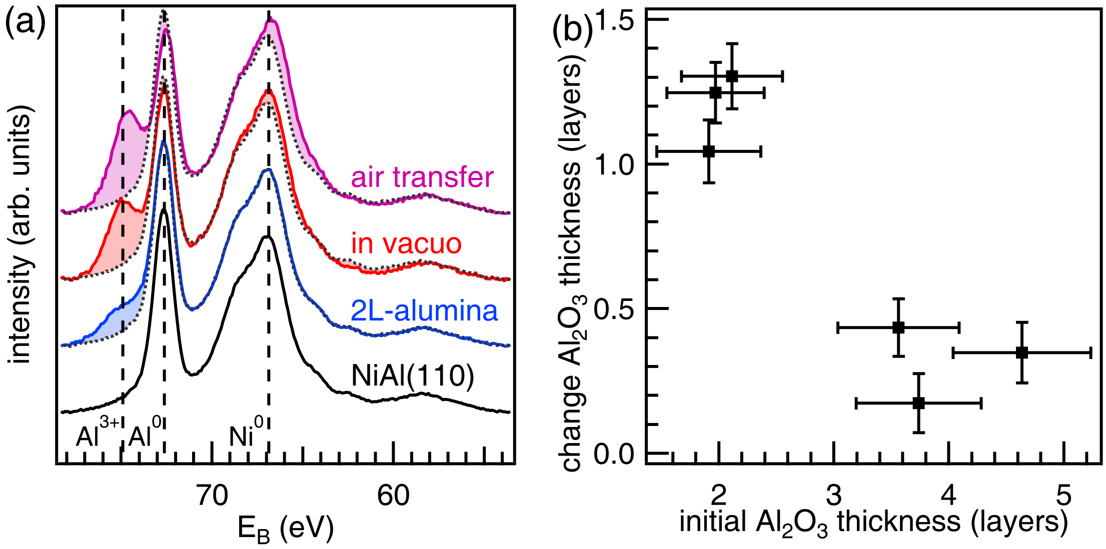

Figure 5.5: (a) Al 2p and Ni 3p XPS of the NiAl(110) substrate (black), 2L-alumina (blue), after SAM deposition from solvent on 2L-alumina *in vacuo* (red) and conventional SAM deposition with transfer through the air (magenta). The shaded area indicates the change compared to the clean NiAl(110) substrate (dashed line). (b) Change of the alumina film thickness during *in vacuo* SAM deposition in dependence of the initial oxide film thickness.

(see Appendix B.2) supports the formation of further oxide or hydroxide.

The thickness of 2L-alumina can be systematically increased via high-temperature oxidation of 2L-alumina/NiAl(110) [51]. Fig. 5.5 (b) shows the change of the alumina thickness during *in vacuo* SAM formation depending on the initial oxide thickness. For thicker alumina films the thickness change decreases significantly. Limiting factors for the oxide film thickening could be the rate of charge transfer from the oxide surface to the metal interface [83], the aluminum availability at the interface [83, 156], or the limited mass transport [157]. As no charging was observed during the XPS measurements on these samples and samples with thicker alumina films [51], we exclude the rate of charge transfer as a limiting factor. Further, the aluminium to nickel ratio was the same for samples with different thicknesses [51]. We conclude that the transfer of oxygen and aluminum atoms through thicker oxide films is likely to limit the thickness change.

Fig. 5.6 compares two different samples: One was directly transferred back to the UHV after SAM attachment in the SAMcham (red). For the other sample, the SAM attachment was followed by air exposure for five minutes (black). No significant difference (grey) between both preparations was detected by means of XPS. Slight changes in the area of the Re 4f peaks of the molecule are due to different stages of radiation damage (see

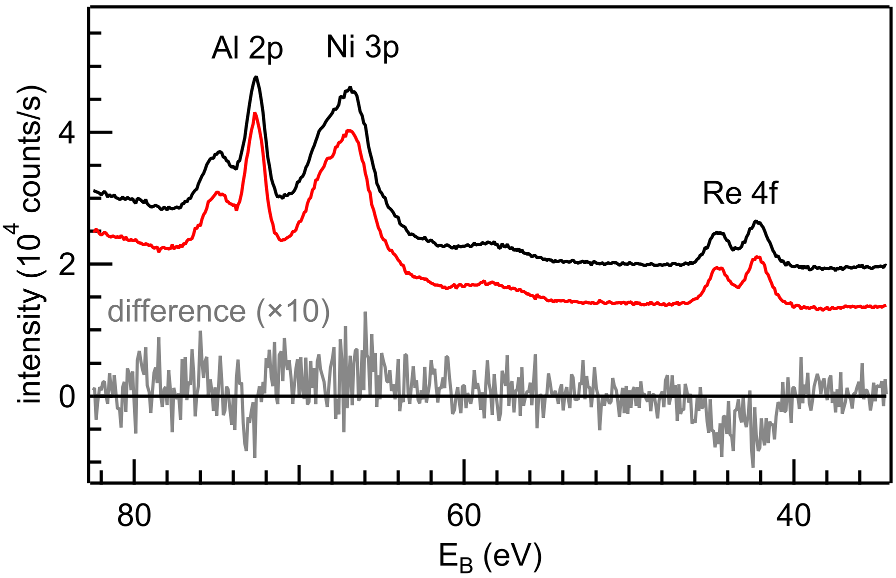

Figure 5.6: Al 2p, Ni 3p and Re 4f peak after *in vacuo* SAM deposition (red). Air exposure directly after SAM deposition (black, vertical offset) does not alter the heterostructure.

Appendix B.1). The intact SAM acts as a capping layer, protecting the substrate from further oxidation under ambient conditions. When the molecules are damaged by radiation, this passivation effect is lost (see Appendix B.1).

5.4 Summary and outlook

In summary, a method is established for the functionalization and passivation of ultrathin oxide films with SAMs. Exposure of ultrathin oxide films to air leads to a significant increase in thickness of the oxide, which can be reduced to one additional atomic layer of oxide by depositing the SAM in a dedicated chamber *in vacuo*. This enables us to produce a metal-insulator-SAM heterojunction with a precise thickness control of the insulating ultrathin film. The resulting heterostructure is stable in air, making further handling and processing of samples outside of UHV possible without altering of the oxide thin film. The *in vacuo* attachment of SAMs can be extended to a broad class of molecules vulnerable to pyrolysis upon evaporation and presents an elegant method of attaching molecular layers on solid substrates that are sensitive to air. Diimine rhenium(I) tricarbonyl complexes can be incorporated into efficient homogenous photocatalytic systems for CO_2 reduction [141, 142] and H_2 production [143–145], and their attachment as SAM is a step towards their integration into a heterogeneous system. The thickness of the ultrathin alumina films on NiAl(110) used here can be systematically controlled [51, 158]. This can enable high-precision tuning of the electron transfer between excited molecules and the substrate, as the lifetime of excited charges in the molecule should depend on the thickness of the insulating tunneling layer at the interface.

5.5 Experimental Section

NiAl(110) single crystals were purchased from *MaTecK - Material-Technologie & Kristalle GmbH*. The experiments were conducted in the modified VG ESCALAB 220 UHV system described in chapter 3. The NiAl(110) surface was cleaned with cycles of argon sputtering and subsequent annealing at 1270 K. The 2L-alumina films were prepared by oxidizing the clean NiAl(110) surface in $5 \cdot 10^{-6}$ mbar oxygen at 530 K and subsequent annealing in UHV at 1070 K. The thickness of the thin films was increased systematically by oxidation in $9 \cdot 10^{-5}$ mbar oxygen at 970 K, similarly as described in detail in chapter 4.
XPS was conducted at normal emission with an non-monochromatized Mg Kα source, providing photons with an energy of h$\nu = 1253.56$ eV. The energy scale was calibrated as described by Seah [111]. UPS measurements were performed under normal emission with a helium discharge lamp (He I$_\alpha$, h$\nu = 21.22$ eV).
The coverage of rhenium atoms N_{Re} is calculated by comparing the intensity of the Re 4f peak (I_{Re}) to the intensity of a polycrystalline silver reference sample (I_{Ag}) using equation 5.1:

$$\begin{aligned} N_{Re} =& \frac{I_{Re}}{\sigma_{Re}} \cdot \frac{\sigma_{Ag}}{I_{Ag}} \cdot \lambda_{Ag}, \cdot \cos(\theta) \cdot n_{Ag} \\ =& \frac{I_{Re}}{\sigma_{Re}} \cdot A, \end{aligned} \tag{5.1}$$

where, σ_X refers to the corresponding subshell photoionization cross-section [148], θ refers to the electron emission angle with respect to the surface normal, $n_{Ag} = 58.7\,\mathrm{atoms/nm^3}$ is the density of silver atoms, and λ_{Ag} is the inelastic mean free path calculated with the Tanuma-Powell-Penn (TPP-2M) equation [44]. The constant A was evaluated for the range of silver peaks from 3s to 4p. The X-ray flux was kept constant.
The oxide thickness (d) is calculated numerically by the intensity ratio of the oxidized Al

species (I_O) and the metallic Al^0 peak (I_M) according to equation 5.2:

$$d = \lambda_O \cdot \cos(\theta) \cdot \ln \left[\frac{n_M}{n_O} \cdot \frac{\lambda_M}{\lambda_O} \cdot \frac{I_O}{I_M \exp\left(\frac{d}{\lambda_O \cos(\theta)}\right)} + 1 \right], \tag{5.2}$$

where λ_x refers to the respective inelastic mean free path of the photoelectrons and n_x to the density of Al atoms in the material x ($n_M = 41.6\,\mathrm{atoms/nm^3}$, $n_O = 42.7\,\mathrm{atoms/nm^3}$, calculated based on structural models from Taylor *et al.* [159] and from Smrčok *et al.* [93]). $\lambda_O = (2.67 \pm 0.47)\,\mathrm{nm}$ was calculated with the TPP-2M equation. $\lambda_M = (1.99 \pm 0.21)\,\mathrm{nm}$ was normalized by referencing the intensity ratio in the case of 2L-alumina, and is in good agreement with the value obtained with the TPP-2M equation ($\lambda_{M_{PPT-2M}} = (2.08 \pm 0.43)\,\mathrm{nm}$). A lattice plane distance of $0.172\,\mathrm{nm}$ was used to calculate the number of alumina layers, which is the lattice plane distance of γ-Al_2O_3 in (111) direction based on the structural model from Smrčok *et al.* [93]. Equation 5.2 is similar to the one introduced by Strohmeier [87] for determining the oxide thickness on aluminum alloys, but additionally considers the attenuation of photoelectron intensity from the metal substrate below the oxide in the oxide film.

6 Rhenium and ruthenium dyes with covalent linkers on alumina/NiAl(110)

The in section 5.2 presented method for molecule deposition enables a high-throughput characterization of different molecules. Five organometallic dyes are characterized with XPS and UPS. Coverage, counterion coadsorption, and electronic structure are analyzed. Most content of this chapter is from a manuscript *in preparation* [160].

6.1 Motivation

Molecular systems have great potential for applications in dye-sensitized solar cells [10, 17] for the electric power generation and in dye-sensitized photoelectrochemical cells [14–16] for energy storage. The anchoring of the dye molecules is crucial to ensure coupling of the molecule to the substrate and enable the transport of excited charge between the molecule and electrode [161]. Most PES and STM based studies previously focused on the dye/titania interface [114, 162–167]. Recently a number of studies emphasized the role of insulating layers, which can reduce charge carrier recombination [19–23] and apparently promote thus charge carrier separation. Computational efforts on the dye/alumina/titania systems indicated that the adsorption geometry of the dyes can also be altered by interfacial alumina layers, as was shown for the N3 ruthenium dye [25, 168, 169].

In this work, the adsorption of five organometallic dyes on 2L-alumina is studied with XPS and UPS to deliver experimental insights about the dye/alumina interface. Fig. 6.1 shows their chemical structures. We compare three rhenium-based dye molecules. The first dye (1) is [Re(NCS)$(CO)_3$(DCO_2bipy)], and is the same dye used in chapter 5. Molecule (2) is [Re(NCS)$(CO)_3$($DMPO_3$bipy)] (DMPO3bipy = 2,2'-bipyridine-4,4'-dimethylene phosphonate). The carboxyl linkers are exchanged with methylene phosphonate linkers.

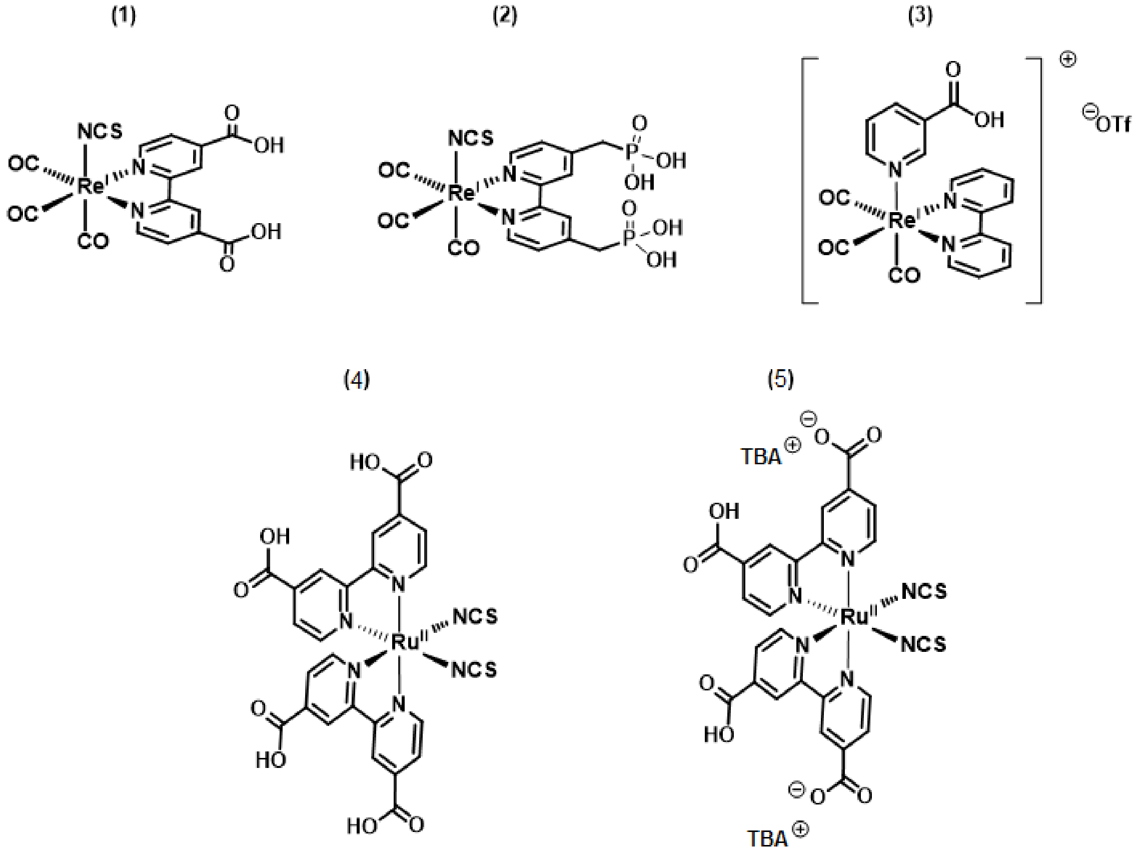

Figure 6.1: Structures of the used metalorganic dyes. Courtesy of Mathias Mosberger.

Molecule (3) is [Re(niacin)$(CO)_3$(bipy)]. The thiocyanate is replaced by a niacin group, to bind the molecule not via the bipy but via the axial ligand. It is accompanied by trifluoromethane sulfonate (OTf) counterion to maintain charge neutrality. Molecule (4) is the prototypical N3 ruthenium dye. (5) is N719, a deprotonated version of N3 with two tetrabutylammonium (TBA) counterions. With XPS the molecular density is determined and the coadsorption of the counterions of molecule (3) and (5) is discussed. Further, their electronic structure is compared using UPS.

6.2 Results and discussion

Fig. 6.2 (a) shows the XPS of the Al 2p, Ni 3p and Re 4f core-level for the 2L-alumina substrate and SAMs of the rhenium dyes. The metallic Al 2p and Ni 3p substrate peaks at 72 and 67 eV dominate the spectra. Interfacial Al^{2+} and Al^{3+} in the 2L-alumina film delivers a contribution at higher binding energies [53]. During the SAM deposition, a rise

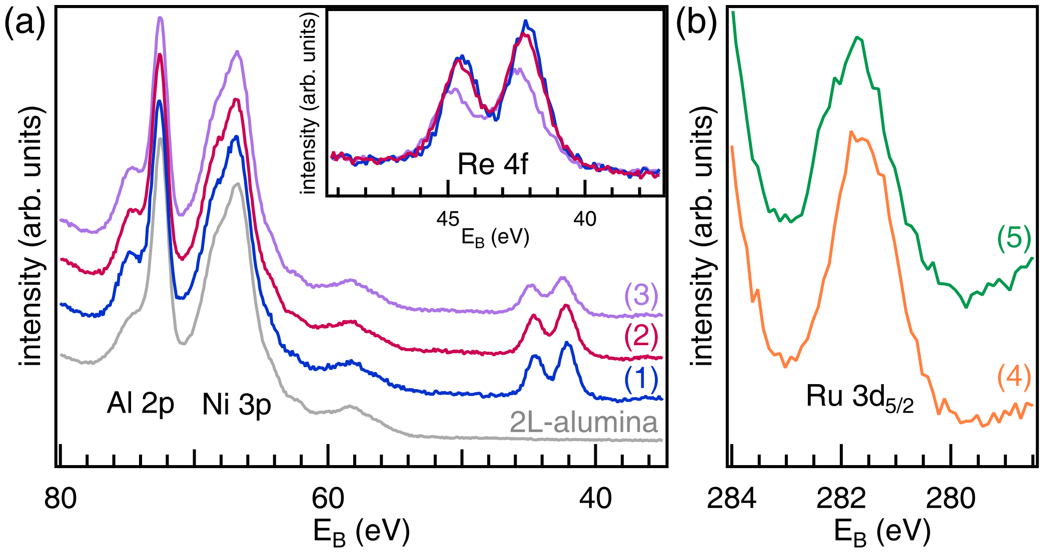

Figure 6.2: (a) XPS of Al 2p, Ni 3p and Re 4f peaks for 2L-alumina (grey) and monolayers of molecule (1) (blue), (2) (red) and (3) (green). The inset compares the intensity of the Re 4f peak. (b) XPS of the Ru $3d_{5/2}$ for molecule (4) (orange) and (5) (green).

of the Al^{3+} between 74 and 75 eV is observed, similarly as described earlier [52]. This rise is identical for all three molecules and we quantify the total thickness after molecule deposition to be 2.5 atomic oxide layers. This is a reduction of the thickness increase by 0.5 layer when compared to the results presented in section 5.3 (Fig. 5.5) and is attributed to the use of two septa in the flask lid. The Re 4f peaks for molecule (1), (2) and (3) are compared in the inset of Fig. 6.2 (a). No significant difference is observed between molecule (1) and (2) regarding binding energy and intensity. Both molecules have two covalent linkers located at the bipy: (1) has carboxyl groups and (2) methylene phosphonate groups. Apparently, the additional atoms in the methylene phosphonate groups are accommodated beneath the bipy, not requiring significantly more space on the surface. A shift to higher binding energies is observed for the Re 4f of molecule (3), when compared to the other two rhenium dyes. In a multilayer of (3) this shift is revoked (see Appendix C.1). As (3) is positively charged, this shift might be caused by a remaining positive net-charge if there is a lack of counterions on the surface. Further, a lower coverage is obtained for this molecule, where one carboxyl linker is attached on the axial pyridine. Apparently the molecule requires significantly more space, probably the dimension of the molecule on the axial direction is increased when the thiocyanate is replaced with pyridine. Fig. 6.2 (b) displays the XPS of the Ru $3d_{5/2}$ peak of the both ruthenium dyes (4) and (5). Both dyes have the same structure, and (5) is the deprotonated version of (4), having two

Table 6.1: Density of the molecules in the monolayer coverage and the average spacial separation between two molecules.

molecule	density (nm^{-2})	separation (nm)
(1)	1.27±0.32	0.95±0.24
(2)	1.27±0.32	0.95±0.24
(3)	0.99±0.26	1.08±0.29
(4)	0.60±0.15	1.38±0.34
(5)	0.58±0.15	1.41±0.35

TBA counterions. The difference in the intensity is slightly lower for (5), but cannot be accounted as significant.

When comparing the density of the molecular monolayers (Table 6.1) we find that the the rhenium dyes exhibit a significantly higher coverage than the both ruthenium dyes. The adsorption of molecule (4) was extensively studied on titania, showing multi-conformational adsorption [165, 167]. Further, Ikeda *et al.* showed that most molecules are located with a separation of 1.2 to 1.6 nm [163], which is in good agreement with the average separation obtained from the molecular density (see Table 6.1). For molecule (4) and (5) no drastic change in the density is observed. This is surprising, as the TBA counterions have a significant size and their co-adsorption would intuitively require a significant amount of space.

In a next step, we look at the coadsorption of the counterions. A Ni LMM Auger line from the substrate is present in the energy window of the N 1s peak. The difference spectra shown in Fig. 6.3 (a) are formed using a normalized substrate spectrum and by subtracting it from the spectra after molecule deposition. Molecule (1), (2) and (4) have nitrogen atoms in the bipy and the thiocyanate in a ratio of 2:1, which can be clearly identified at 401 and 399 eV [52]. Molecule (5) exhibits a third peak at 403 eV due to the adsorption of TBA. The intensity ratio of 1.0:2.0:1.0 between them indicates a stoichiometric adsorption of dye molecules and TBA counterions. On nanostructured TiO_2 [162, 164] and on $TiO_2(001)$ [170] XPS indicated a significant loss of TBA counterions upon adsorption, when compared to the stoichiometric ratio. Molecule (3) contains nitrogen atoms in the bipy and in the axial niacin ligand. The N 1s spectrum of the multilayer exhibits one distinct peak due to these three nitrogen atoms (see Appendix C.1), which are chemically in the same coordination. In the monolayer, the peak broadens significantly. A measurement with a monochromatic source also confirmed the presence of only one compatibly broad peak. We speculate that the molecule binds via the carboxyl group on the axial pyridine ligand and that different adsorption geometries might rotate the bond between the pyridine

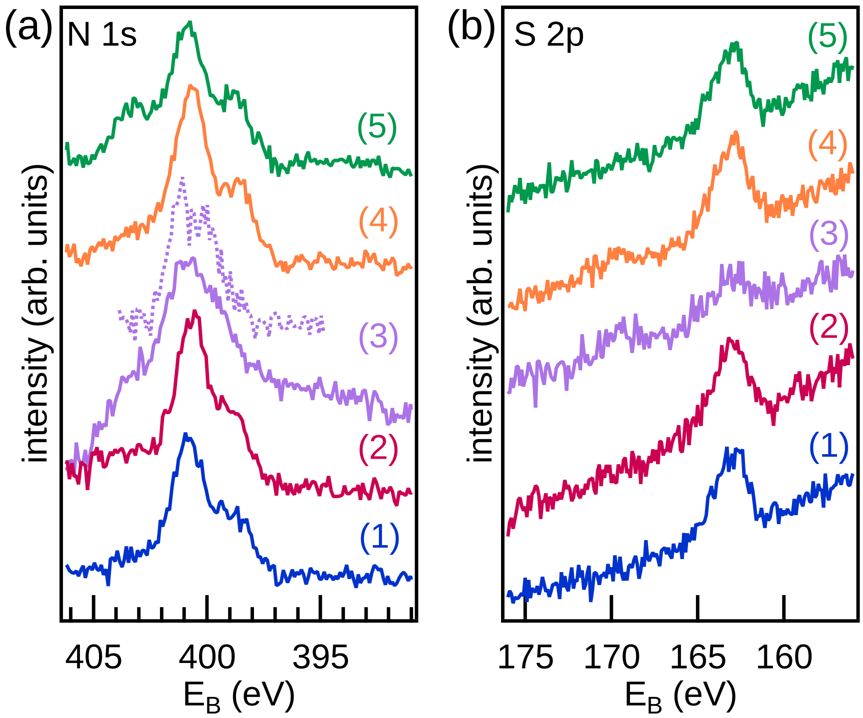

Figure 6.3: (a) Difference spectra of the N 1s peak . The dashed line is a reference measurement with Al Kα source for molecule (3). (b) XPS of the S 2p peak for the monolayer coverage of all molecules.

and the rhenium, leading to a plethora of different conformations of the nitrogen atoms. Fig. 6.3 (b) shows the XPS of the S 2p peak. Molecule (1), (2), (4) and (5) all contain thiocyanate, showing a distinct peak at 163 eV [52]. Molecule (4) showed previously a by 0.7 eV shifted species on $TiO_2(110)$, which was associated with thiocyanate binding to the surface [114]. This is not observed here. A second feature at 169 eV is visible. A similar shift has been previously observed for molecule (5) on titania, indicating that sulfur atoms in the thiocyanate binds to oxygen [170]. It appears reasonable to associate a similar bonding for (4) on 2L-alumina. Interestingly this interaction seems to be revoked for molecule (5), probably due to the counterions. Molecule (3) itself does not contain sulfur, it only is contained in the OTf counterion ($CF_3SO_3^-$). Two sulfur species are observed at 163 and 170 eV. The smaller peak at 170 eV is identified in the multilayer as the intact OTf counterion (see Appendix C.1). The second feature appears to be a remnant of a decomposed counterion, which is underlined by a lack of fluorine in the monolayer (see Appendix C.1). When comparing the total amount of rhenium to the amount of adsorbed sulfur we find a ratio of 1.0:0.8, indicating a nearly stoichiometric adsorption of the counterions. We speculate about a decomposition of the OTf at oxygen deficient line

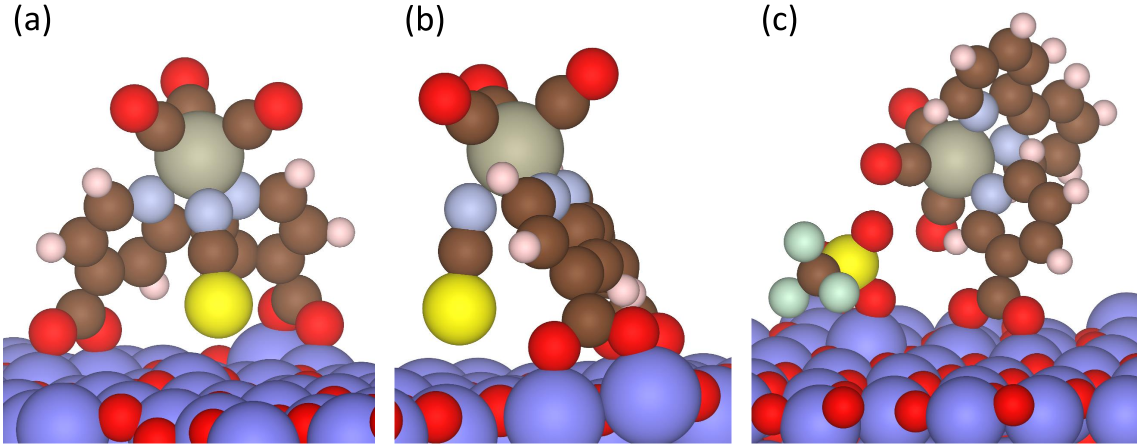

Figure 6.4: DFT optimized structure of (a) molecule (1) adsorbed on 2L-alumina. (b) Same as (a), but rotated. (c) DFT optimized structure of molecule (3) on 2L-alumina. Coordinates are courtesy of Tiziana Musso.

defects occurring in 2L-alumina, which show the behavior of a native electron donor [33]. This might facilitate the release of fluorine and thus the OTf decomposition.

Fig. 6.4 compares DFT optimized structures of molecule (1) and (3). The oxygen atoms from the carboxyl groups anchor the molecule by binding to aluminum atoms (Fig. 6.4 (a)). It is likely that a plethora of adsorption configurations are possible, as was demonstrated for molecule (4) on $TiO_2(101)$ [167]. The thiocyanate of (1) tends to point to an oxygen atom in the surface in this configuration, but the sulfur binds not to the surface. Molecule (3) stands on the niacin group. The OTf ion binds with one oxygen to an aluminum atom and remains intact. Both molecules seem to pull out aluminum atoms above the surface plane as their coordination number increases.

In view of using this molecular system as photoelectrodes, the molecular energy levels and the band alignment in the heterojunction were studied by UPS. Fig. 6.5 (a) shows UPS under normal emission of the 2L-alumina/NiAl(110) substrate (blue), a monolayer (red) and a multilayer (green) coverage of molecule (1). Two molecular features can be identified in mono- and multilayer samples (multilayer as shown in Fig. 5.3 (b)). A fit with two Gaussian functions and an exponential background locates the highest occupied molecular orbital (HOMO) in the SAM 2.8 eV beneath the Fermi level. The work function of the SAM is measured using the secondary electron cutoff and decreases as a result of the radiation damage over time. The initial work function is 4.3 eV (see Appendix B.3).

Fig. 6.5 (b) shows the UPS of the different parts of the heterojunction. The metal substrate (black) dictates the position of the Fermi level. As previously determined, the insulating alumina film has a valence band onset 4.2 eV below [51], and a conduction band onset of 2.2 eV above the Fermi level [91]. The observed molecular states appear similarly for the mono-

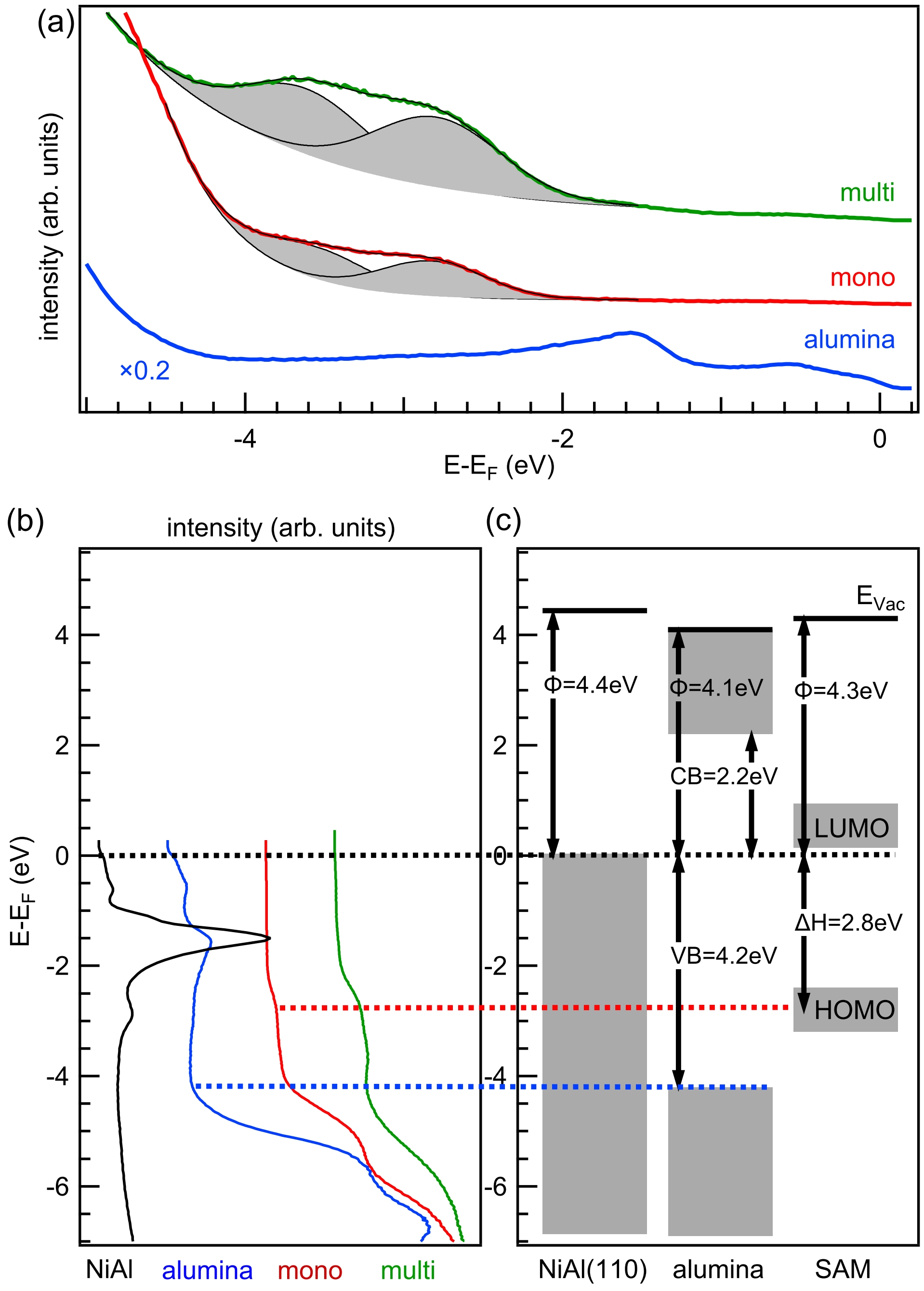

Figure 6.5: (a) UPS of 2L-alumina, of a monolayer (red) and a multilayer (green) of (1) . Two molecular features are identified with Gaussian fits (gray shaded, exponential background). (b) UPS of NiAl(110) (black), 2L-alumina (blue), monolayer (red) and a multilayer (green) of (1). (c) The derived band alignment for the multijunction.

and multilayer coverage, indicating that polarization effects due to the metal substrate are screened and do not alter the electronic structure of the molecule significantly [65,66]. The same applies for charge transfer between the substrate and molecule [133]. We conclude that the electronic structure of the SAM is not influenced drastically by the substrate. Blanco Rodríguez *et al.* [146] previously calculated by DFT one-electron energies and compositions of relevant molecular orbitals of *fac* – [Re(NCS)(CO)$_3$(bipy)], which is the core of the molecule used here. These authors concluded that the HOMO and HOMO-1 have a mixed Re/NCS character, are Re-NCS π-antibonding, and are only separated by 50 meV. Distinguishing the HOMO and the HOMO-1 is not possible within the energy resolution of our analyzer, and we assign these molecular orbitals to the first observed feature at 2.8 eV beneath the Fermi level. The lowest observed singlet electronic transition for *fac* – [Re(NCS)(CO)$_3$(bipy)] by ultraviolet-visible absorption spectroscopy was reported to be 3.3 eV [146]. For *fac*-[Re(NCS)(CO)$_3$(DCO$_2$bipy)] this transition occurs at 3.0 eV (see Appendix B.4), which indicates a 10 % smaller gap between the HOMO and the lowest unoccupied molecular orbital (LUMO). This downshift for the optical excitation is likely due to the attached carboxyl groups, which reduces the electron density on the bipy. The LUMO of *fac* – [Re(NCS)(CO)$_3$(bipy)] was calculated by Blanco Rodríguez *et al.* [146] to be an antibonding π^* orbital that is mainly located on the bipy at approximately 3.7 eV higher energy. Taking a 10 % smaller HOMO-LUMO gap into account, we locate the LUMO for *fac*-[Re(NCS)(CO)$_3$(DCO$_2$bipy)] to be 3.3 *eV* above the HOMO, which is 0.5 eV above the Fermi level. Fig. 6.5 (c) summarizes the found electronic band alignment for the metal-insulator-SAM heterostructure. The molecular orbitals are located inside the band gap of the alumina thin film.

Figure 6.6 (a) compares the UPS of the three rhenium dyes in the mono- and multilayer coverage. The UPS of molecule (2) can, similarly to molecule (1), be well described with two peaks in the mono- and multilayer coverage. HOMO positions and work functions are summarized in Appendix C.4. As the HOMOs are comparably far away from the linker groups, it appears reasonable that they are not drastically affected by them. Molecule (3) does not possess the thiocyanate as an axial ligand, but the niacin. The multilayer can in contrast to the two previous molecules be well described by one peak, which underlines the previous assignment of the first peak in the UPS of molecule (1) and (2). The monolayer of molecule (3) shows one more peak at lower binding energies (shaded area), which could be due to an interface state or be caused by the decomposed OTf.

The electronic structure of molecule (4) was previously discussed in the literature [171–173]. The highest molecular orbitals are generally ascribed to a set of three quasi generated antibonding orbitals based on contributions from the thiocyanate and the ruthenium center. At higher binding energies, occurs another set a three quasi-generated orbitals, which is the bonding counterpart. In between there is a further contribution from the

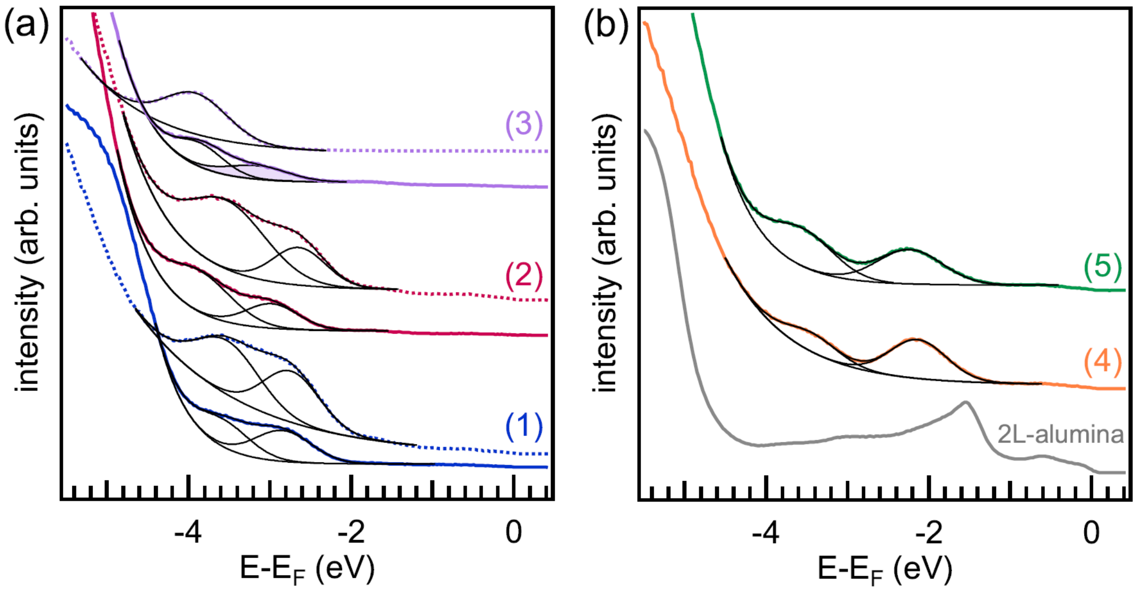

Figure 6.6: (a) UPS of monolayer (solid line) and multilayer (dashed line) coverage of the rhenium dyes (1) (blue), (2) (red), (3) (magenta), and corresponding fits (black). The shaded area indicates the new appearing feature of (3) in the monolayer. (b) UPS of the 2L-alumina substrate (grey), and monolayer coverage of the ruthenium dyes (4) (orange), (5) (green), and corresponding fits (black).

thiocyanate. In the UPS of molecule (4) in Fig. 6.6 (b) two peaks separated by 1.3 eV are identified. In analogy to the previously described electronic structure, we ascribe the first to the the antibonding orbitals and the second to the bonding counterpart. Multiconformational adsorption as observed on TiO_2(101) [167] might broaden the peaks. For molecule (5) the recorded UPS appears qualitatively very similar, but is shifted by approximately 100 meV to higher binding energies.

6.3 Summary and Outlook

Five organometallic dyes were studied on ultrathin alumina films: Three rhenium dyes with systematically changed linker groups and two prototypical ruthenium dyes. When the carboxyl linkers on the bipy are exchanged with methylene phosphonate, the same density of molecules is found in the monolayer coverage. When the linker is attached to the axial ligand, the molecule required more space on the surface. No significant change in the molecular density is observed between the both ruthenium dyes, despite that the large TBA counterion of molecule (5) coadsorbs stoichiometrically. The rhenium dyes require significantly less space on the surface when compared to the ruthenium dyes. The

OTf counterion of molecule (3) also coadsorbs nearly stoichiometric, but decomposes on the surface. We speculate that the defect network in the alumina thin film causes the decomposition. The HOMOs of the rhenium dyes are not drastically affected when the linkers at the bipy are exchanged. However, if the axial ligand is exchanged, the HOMOs are affected. The electronic structure of both ruthenium dyes appears to be nearly the same, but a shift of approximately 100 eV is observed. Further it can be concluded that the deposition procedure presented in the previous chapter 5 enables a high throughput comparison of different molecules.

6.4 Experimental Section

Experiments were conducted in a user modified ESCA lab described in chapter 3. The 2L-alumina films were grown on single crystalline NiAl(110) substrates as described in section 4.1. The molecules were deposited from solution in a dedicated vacuum chamber as described in section 5.2. The ruthenium dyes were obtained from *Solaronix SA*.
XPS was conducted at normal emission with an achromatic Mg Kα source, providing photons with an energy of $h\nu = 1253.56\,\text{eV}$. The energy scale of the spectra was calibrated as described by Seah [111]. The thickness of the alumina films was determined based on the Al^{3+} shoulder of the Al 2p peak as described in [51]. We determine the coverage of rhenium atoms $N_{(3)}$ for molecule (3) by comparing the intensity of the Re 4f peak (I_{Re}) to the intensity of several peaks from a polycrystalline silver reference sample (I_{Ag}) according to:

$$
\begin{aligned}
N_{Re} =& \frac{I_{Re}}{\sigma_{Re}} \cdot \frac{\sigma_{Ag}}{I_{Ag}} \cdot \lambda_{Ag} \cdot \cos(\theta) \cdot n_{Ag}, \\
=& \frac{I_{Re}}{\sigma_{Re}} \cdot A.
\end{aligned}
\tag{6.1}
$$

θ is the emission angle of the photoelectrons with respect to the surface normal, σ_X is the corresponding photoionization cross-section [148], $n_{Ag} = 58.7\,/\text{nm}^3$ is the density of silver atoms, and λ_{Ag} is the inelastic mean free path calculated with the Tanuma-Powell-Penn (TPP-2M) equation [44]. The constant A was evaluated for the range of silver peaks from 3s to 4p.

The density of rhenium atoms $N_{(3)}$ for molecule (3) was determined by comparing the intensity of the Re 4f peak with the intensity obtained from a polycrystalline silver reference sample as described in section 5.5. The density of other molecules was calculated by comparing the intensities of the Re 4f or Ru $3d_{5/2}$ peaks to the intensity of the Re 4f peak of molecule (3). The intensity was normalized to the Ni 3p and Al 2p substrate peaks. The different photoionization cross-sections [148] were considered for the ruthenium dyes. The average separation S_x is calculated here based on the density of metal centers N_x of the respective molecules (see Appendix C.5 for details). Ratios between different atomic species were calculated based on integrated peak intensities and their respective photoionization cross-sections [148]. UPS was recorded with a helium discharge lamp (He I_{α}, $\mathrm{h}\nu = 21.22\,\mathrm{eV}$).

7 Metal-to-ligand charge transfer observed with ultrafast time-resolved core-level spectroscopy

The next task is to study the charge carrier dynamics in the formed heterojunction. After optical excitation in the dye, various processes are possible, which are indicated in Fig. 7.1. One option is that the excited electron-hole pair on the molecule recombines (K_1). The excited electron can also be transferred to the metal substrate (K_2), leaving a positively charged molecule. The hole can also be filed with electrons from the metal substrate (K_3). If this happens before the excited electron left the molecule, the molecule can be negatively charged. If this happens after the excited electron is transferred to the metal substrate, the molecule is again in the ground state. Intersystem crossing and thus a spin flip of the excited electron is a further effect that can occur.

The binding energy of electrons on the metal center in the previously studied dye molecules should be sensitive on the electronic configuration of the molecule. For instance, optical excitation of the rhenium dyes should shift electron density on the molecule which can result in a chemical shift. Charging of the molecule should also modify the electrostatic potential of the electrons in the metal center, and thus the binding energy of the electrons. Ultrafast time-resolved core-level spectroscopy might have the potential to study these effects. First prototypical experiments are performed, and the metal-to-ligand charge transfer (MLCT) is observed as a chemical shift in the 4f electrons of a rhenium dye. The oxidized rhenium appears and vanishes with a periodicity of 180 fs, indicating the oscillation of charge on the molecule. In total, ultrafast time-resolved core-level spectroscopy appears to be a promising method to study charge transport phenomena with chemical sensitivity.

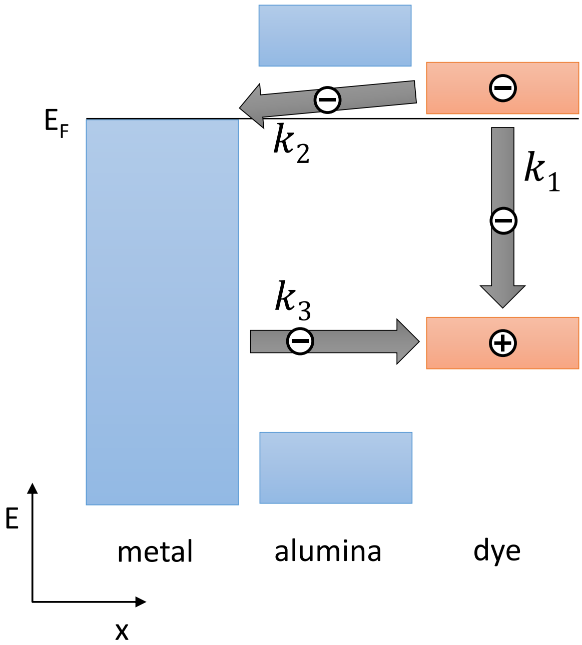

Figure 7.1: Scheme indicating possible electron transfers after excitation of the dye in the dye/alumina/NiAl(110) heterojunction.

7.1 Introduction

X-ray photoelectron spectroscopy is a powerful tool to analyze the electronic structure and chemical composition of surfaces and interfaces [174, 175]. The emergence of ultrafast ultraviolet, extreme ultraviolet and soft-X-ray pulses enables the monitoring of processes on surfaces with pump-probe experiments in the femtosecond regime [176]. A current scientific frontier is the usage of such pulses produced by high-harmonic generation or free-electron lasers to observe core-level shifts [177–181]. This approach can also be applied to large molecules adsorbed on surfaces to probe the local chemical environment of specific atoms [182, 183]: Dachraoui *et al.* performed time-resolved spectroscopy of the 4d core-level of iodine in an adsorbate molecule and unveiled a molecular configuration cycle after excitation [182]. Siefermann *et al.* observed a chemical shift of the ruthenium 3d peak in the N3 dye (molecule (4) introduced in chapter 6) adsorbed on zinc oxide after optical excitation and associated it with an interfacial charge transfer state [183]. Photoinduced transfer of charge carriers is a common process in metal-organic dyes: The MLCT is a process in metallorganic dyes occurring after light absorption. Due to different locations of the HOMO and the LUMO, the electron density is shifted during an electronic transition, which can reduce or oxidize different parts of the molecule. A range of processes can follow the MLCT, such as intersystem crossing, the population of long-lived triplet states or

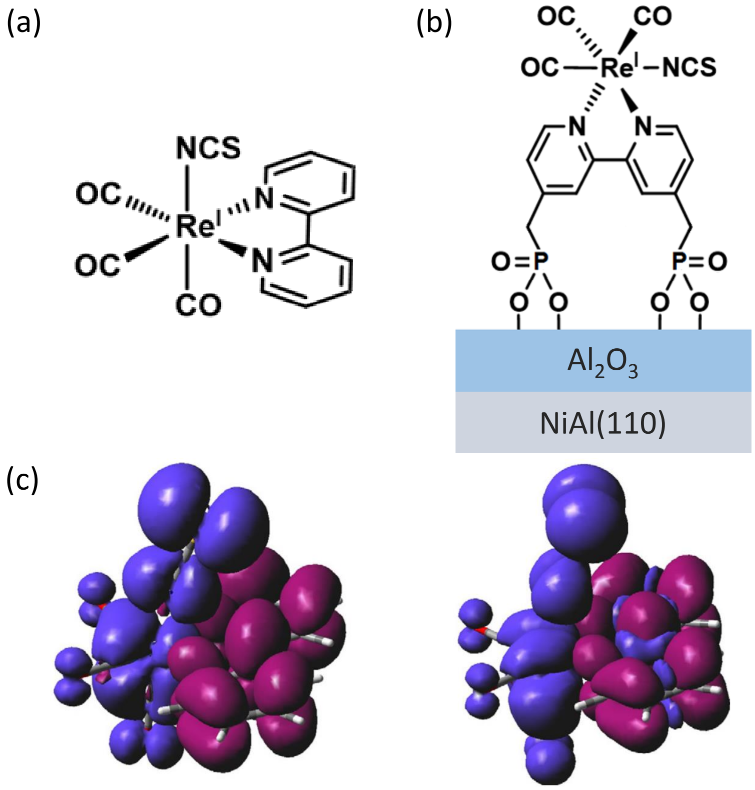

Figure 7.2: (a) Structure of [Re(NCS)(CO)$_3$(bipy)]. (b) [Re(NCS)(CO)$_3$(2CPO$_3$bipy)] /Al$_2$O$_3$/NiAl(110) heterostructure. (c) Change of electron density during the $a^1A' \rightarrow a^3A'$ (left) and $a^1A' \rightarrow a^3A''$ (right) electronic transition [Re(NCS)(CO)$_3$(bipy)]. Blue indicates a decrease and violet an increase of electron density. Panel (c) reprinted from Vlček and Záliš [187].

high spin states, structural reorganization of the molecule and coherent coupling between energetically close states [140, 184–186]. Siefermann *et al.* [183] calculated that the MLCT should induce a core level binding energy shift of the Ru 3d peak between 0.5 and 1.4 eV due to the removal of electron density at the ruthenium center of the N3 dye, indicating that this process can also be observed by time-resolved core-level spectroscopy.

Here, we investigate the MLCT of the rhenium-based dye molecule [Re(NCS)(CO)$_3$(bipy)] on ultrathin alumina films with time-resolved core-level spectroscopy. The rhenium 4f core-level has a binding energy of 42.1 eV [52], making it accessible for probing with ultrashort extreme ultraviolet pulses generated by the Harmonium beamline at the Lausanne Centre for Ultrafast Science at the Ecole Polytechnique fédérale de Lausanne [188, 189]. The structure of [Re(NCS)(CO)$_3$(bipy)] is displayed in Fig. 7.2 (a), which is the core of the molecules used here. The modified molecule featuring phosphate linker groups ([Re(NCS)(CO)$_3$(2CPO$_3$bipy)]) is attached to an ultrathin alumina film on a NiAl(110) substrate, as shown in Fig. 7.2 (b). Previous work [146, 187] demonstrated that optical

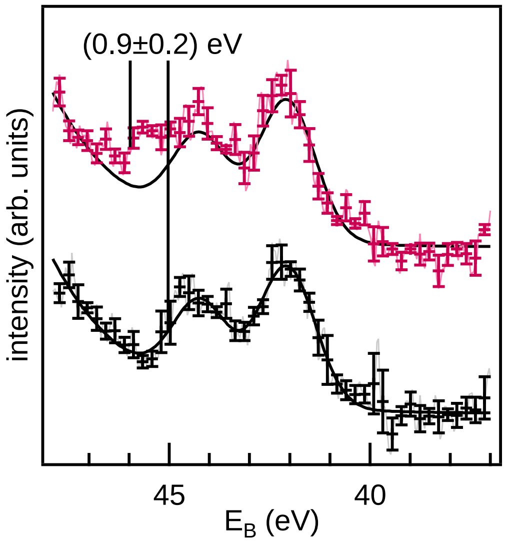

Figure 7.3: Re 4f spectrum of a multilayer coverage of molecules before (grey, black) and 500 fs after excitation (red). The recorded data (thin lines) was binned (markers). A fit (black line) with an exponential background describes the Re 4f prior to excitation.

excitation initiates a shift of electron density in [Re(NCS)(CO)$_3$(bipy)] from the metal center and the axial thiocyanate ligand to the bipy (Fig. 7.2 (c)). We observe a chemical shift of approximately 0.9 eV after the optical excitation and associate it with the MLCT. We further find that the signal of the oxidized rhenium species oscillates with a period of 180 fs, indicating that charge is transferred back and forth on the molecule. A possible interpretation is discussed involving vibrations of the molecule, but it is concluded that further experiments and a better understanding of the photoemission process in excited molecules are required.

7.2 Results and discussion

Fig. 7.3 shows the spectrum of the Re 4f peak of a multilayer coverage [Re(NCS)(CO)$_3$(DCO$_2$bipy)] (molecule (1) in Fig. 6.1) prior to excitation (black), a fit of the binned data, and comparison to a spectrum after excitation (red). An exponential background is used to account for the increase of secondary electrons. The branching ratio is the intensity ratio between the two spin-orbit-split peaks. A value of 1.54±0.15 is deducted from the fit and is significantly higher than 1.25, which is the expected value based on the degeneracy of an f-peak. Similar effects were already observed by Ausmees *et al.* [190] for the 4d branching ratio of Xenon for low photon energies and were explained within the relativistic random-phase approximation [191, 192]. After excitation (red), the spectrum shows an additional feature at higher binding energies. Fitting the spectrum with two rhenium doublets having the same spin-orbit splitting, branching ratio and peak width did not lead to satisfying results. Dachraoui *et al.* [182] observed strong changes in the branching ratio of the I 4d peak in iodo-phenylphenol while exciting the molecule, and proposed an explanation based on the changes in the electronic configuration and the population of magnetic sub-levels of the spin-orbit-split core-levels during the excitation [182]. Similar effects might also occur in our case. To quantify the chemical shift, the turning point at the high binding energy side of the Re 4f peak is determined, as indicated in Fig. 7.3. We find a shift of $0.9 \pm 0.2\,\mathrm{eV}$.

A MLCT state, where the electron density is shifted from the rhenium, the axial thiocyanate ligand, and the carbonyls of the molecule to the bipy, is predicted to induce a chemical shift of 0.8 eV (see Table 7.1). Other possible scenarios are the injection of the excited electron into the substrate or the reception of an electron being transferred from the metal substrate into the hole of the molecule. Both scenarios require interaction of the molecule with the metal substrate, which we do not expect for a multilayer sample to be dominant. Further, they would lead to significantly different chemical shifts (see Table 7.1).

In a next step, we study the excitation of a monolayer of [Re(NCS)(CO)$_3$(2CPO$_3$bipy)] (molecule (2) in Fig. 6.1)at different time delays. Fig. 7.4 (a) shows the average of two spectra recorded 450 and 850 fs before the pump pulse reaches the sample. The data points in the recorded spectra are binned to markers, and the error bars correspond to the respective standard deviations. One marker at 42 eV was removed for this and all following spectra, as a "‘hot pixel"’ of the channel plate detector (see Fig. 7.4 (a), gray line). A fit with an exponential background is applied to account for the edge of the channel plate detector at the low binding energy side of the spectrum. The branching ratio is here 1.66±0.10. A slight deviation from the previous experiment can be explained by the higher photon energy used for this experiment. No drastic change is observed in the spectrum directly after excitation (Fig. 7.4 (b)). The most significant change is observed 350 fs after

Table 7.1: Binding energy shift (ΔE) of the Re 4f peak for the excited molecule in the triplet state (M^*), the positively charged molecule (M^+), and the negatively charged molecule (M^-). Courtesy of Marcella Ianuzzi.

state	ΔE (eV)
M^*	+0.8
M^+	+4.2
M^-	−3.4

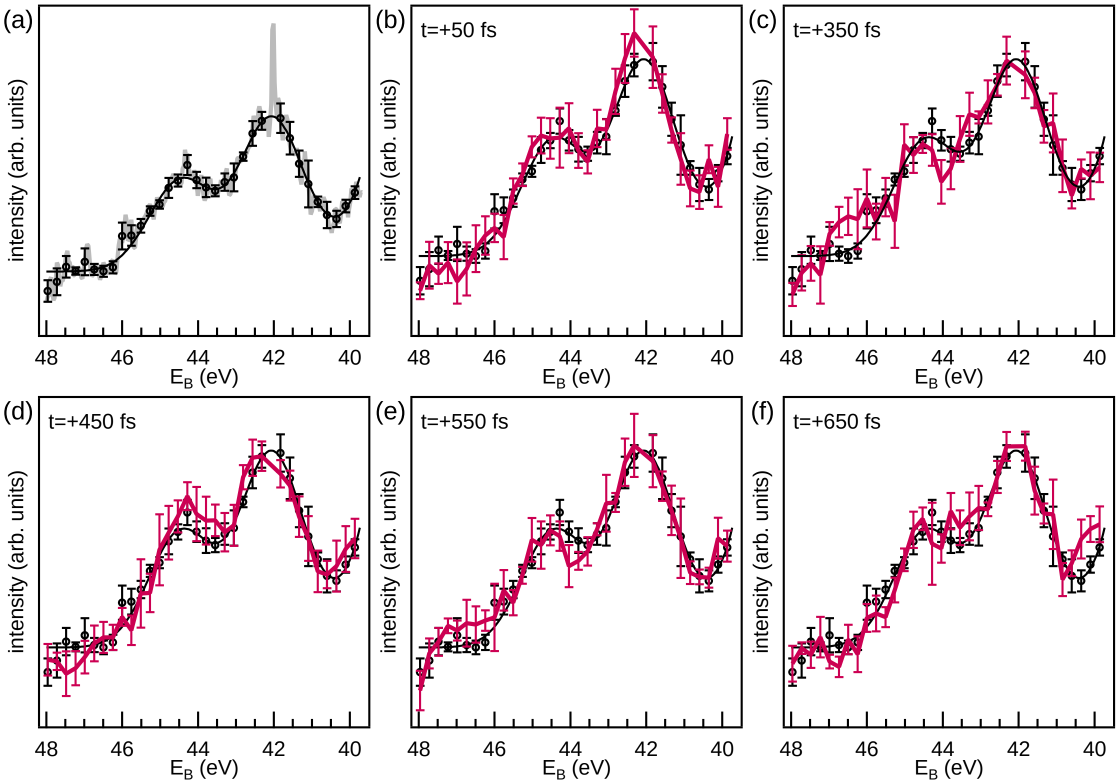

Figure 7.4: (a) Re 4f spectrum before excitation (gray), binned data (black markers), and fit (solid black line). (b) to (f) display binned data for different time delays (red). Binned data and the fit of the molecule prior excitation from (a) is attached to each graph to enable a better comparison.

excitation (Fig. 7.4 (c)), similarly as observed previously in the multilayer coverage (Fig. 7.3). This additional intensity vanishes again within 100 fs (Fig. 7.4 (d)). However, it seems to reappear after additional 100 fs again (Fig. 7.4 (e)) and vanishes again within 100 fs (Fig. 7.4 (f)).

Fig. 7.5 (a) shows the difference spectrum 350 fs after the excitation. Two new features appear, which we attribute to a shift of the Re 4f duplet. The shifted component of the $4f_{7/2}$ is significantly smaller than the one from the $4f_{5/2}$, as it needs to compensate a depletion of the unexcited species in this region. The additional intensity occurring from the $4f_{5/2}$ between 46.1 and 46.8 eV thus seems to be the best indicator for tracking the temporal evolution of the oxidized rhenium caused by the MLCT for different time delays (gray shaded area in Fig. 7.5 (a)). Fig. 7.5 (b) Shows the integrated intensity between in this area for different time delays in five independent angle ranges of the detector. All traces show a similar signature, indicating an oscillation which has a maximum at approximately 350 fs, and decays later. Fig. 7.5 (c) summarizes the five traces. Intensity beneath zero might be due to a depletion of the neighboring peak of the unexcited species or due beam walk on

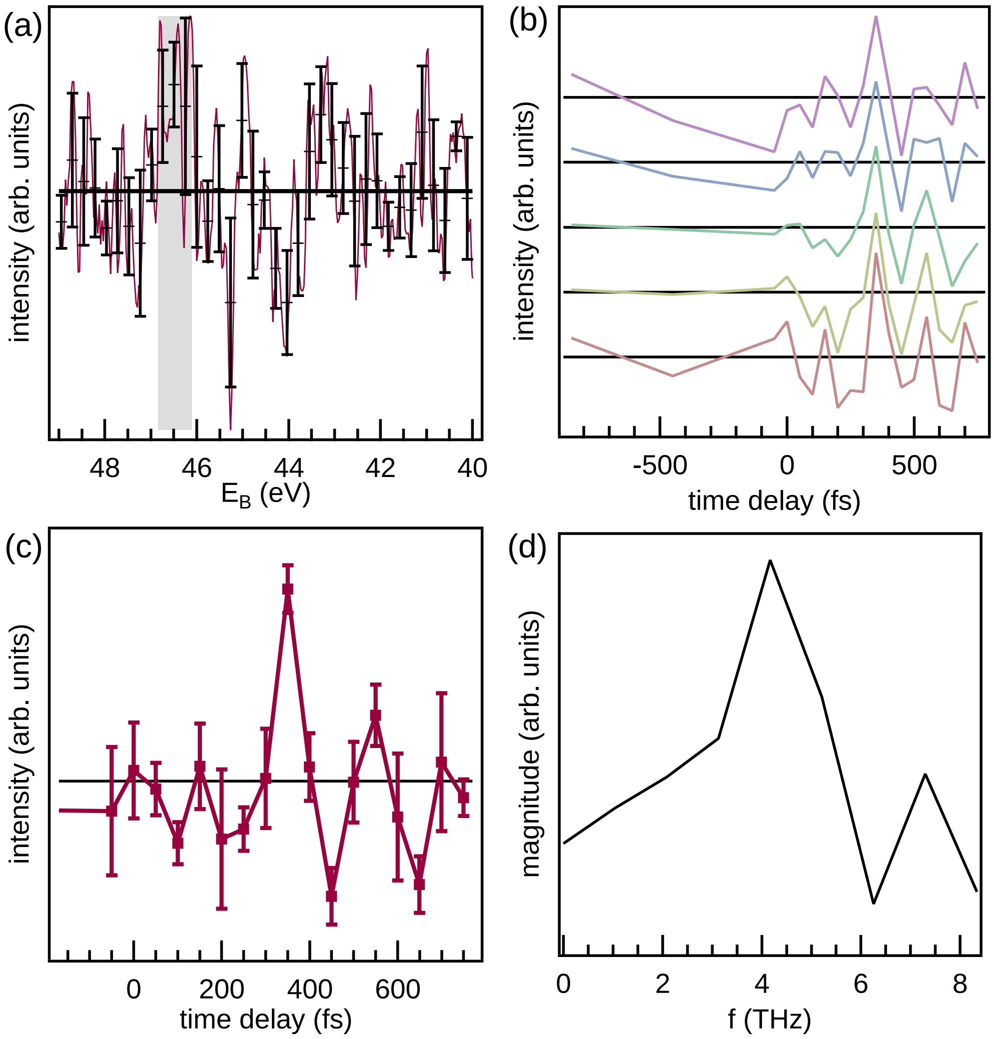

Figure 7.5: (a) Difference spectra for t=+350 fs (red) and bined data (black markers). The black line indicates zero. The gray marked energy range is used for analyzing the intensity at different time delays. (b) Intensity evolution for different time delays in the gray marked energy range in (a) for different angle ranges of the channel plate detector (orange: -9° to -5°, yellow: -5° to -1°, green: -1° to 3°, blue: 3° to 7°, magenta: 7° to 11°). (c) Average of the five curves shown in (b). The errorbars correspond to the standard deviation. (d) Fourier transform of (c).

the sample for different delays. Modulation of the shown transient due to the presence of the $4f_{7/2}$ peak from fully ionized molecules cannot be excluded, but the appearance of the second feature between 43 and 44 eV (in 7.5 (a)) indicates that this could only be a minor contribution. The period of the oscillation is approximately 180 fs. This indicates that charge is transferred away from and back to the rhenium atom in regular time intervals. A Fourier transform (Fig. 7.5 (d)) of the transient confirms an oscillation with a frequency

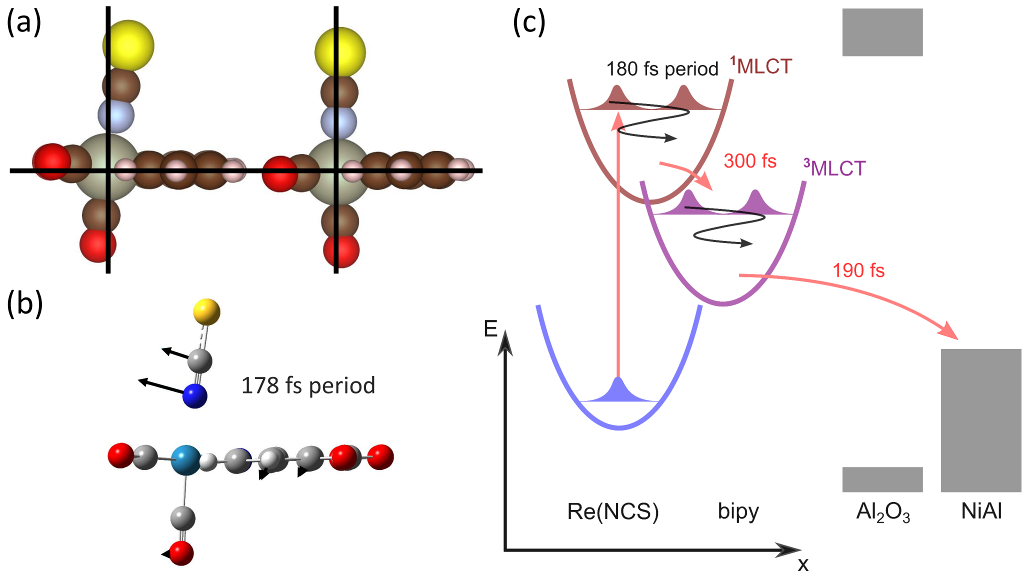

Figure 7.6: (a) Structure of [Re(NCS)(CO)$_3$(bipy)] in the ground state (left) and in the lowest triplet excited state (right) (coordinates from Kvapilová *et al.* [147]). (b) Representation of a NCS displacement during a molecule vibration in [Re(NCS)(CO)$_3$(DCO$_2$bipy)] with a periodicity of 178 fs (courtesy of Ricardo J. Fernández-Terán). The black arrows indicate the displacement vectors. (c) Scheme of the the proposed scenario. X represents the spatial or nuclear coordinate.

of approximately 4 to 5 THz.

In a next step, a possible interpretations for the periodical occurrence of the oxidized rhenium is discussed based molecular vibrations. Molecules can undergo significant structural changes during light exposure and during electronic excitations [184, 185]. Fig. 7.6 (a) shows the side view of [Re(NCS)(CO)$_3$(bipy)] in the ground state and in the lowest triplet-excited state, as calculated by Kvapilová *et al.* [147]. The molecule was rotated for clarity so that the bipy in both models are in the same plane. In the ground state, the thiocyanate is inclined to the bipy. During the MLCT, a significant amount of electron density is transferred to the bipy from both, the thiocyanate and the rhenium. This leads to a repulsion between the thiocyanate from the bipy an reshapes the molecule (see Fig. 7.6 (a)). Both these structures represent the initial and the final state of the MLCT. The hypothesis is that the initial MLCT triggers a motion in the molecule. Fig. 7.6 (b) pictures how the thiocyanate is displaced in [Re(NCS)(CO)$_3$(DCO$_2$bipy)] during a molecular vibration with a periodicity of 178 fs (singlet ground state, in acetonitrile). Further similar lattice vibrations can occur with periodicities of approximately 180 fs [193]. Even though the vibration frequency can change due to the environment and although a different linker group was used, we speculate that a similar molecular motion could be initiated during the optical excitation[1]. The scheme in Fig. 7.6 (c) summarizes this hypothetical scenario. Electrons are excited from the ground state (blue) into the ^{1}MLCT (brown). According to the Franck–Condon principle, the electron movement can be considered instantaneous when compared to a nuclear motion. The electronic transition into the ^{1}MLCT state brings the molecule into a new vibrational level, triggering in the here given case oscillations of the molecule. The movement of the electron on the molecule defines the rise and fall of the feature observed in the time-resolved core-level spectroscopy at binding energies between 46 and 47 eV (Fig. 7.5 (a)). Thus, the observed 180 fs period can be interpreted as a charge carrier oscillation, which could be connected or triggered by a molecular vibration. After approximately 300 fs a significant rise is observed in the amplitude of the signal (in Fig. 7.5 (b) and (c)). Intersystem crossing leading to the occupation of triplet states is observed in the similar [Re(L)(CO)$_3$(bipy)] (L=Cl, Br, I) complexes in solution at time scales between 80 and 170 fs [140, 194] (depending on the axial ligand and the solvent environment). This process, or the occupation of an interface state, could drive the electron further away from the metal center, making the chemical shift in the time-resolved core-level spectra after 300 fs more pronounced. After this rise, the amplitude decays with a lifetime of approximately 190 fs. A decay through interaction with the metal substrate seems to be a reasonable interpretation. Excited electrons from the molecule can tunnel through the ultrathin alumina layer into the substrate. After this process, additional contributions due to the fully ionized molecule might occur (see Table 7.1), but could not be detected within these measurements.

7.3 Summary and Outlook

Time-resolved core-level spectroscopy is used as a tool to observe ultrafast charge transfers in rhenium based dye molecules. The oxidation of the metal center during the MLCT causes a measurable chemical shift, which is in agreement with the calculated value. An oscillating appearance of oxidized rhenium with a periodicity of 180 fs is observed in the [Re(NCS)(CO)$_3$(DCPO$_3$bipy)]/Al$_2$O$_3$/NiAl(110) heterostructure. We speculate about a possible structural rearrangements of the molecule which could induce molecular vibrations and cause these periodic changes, but a final explanation of the observed phenomena cannot be given.

Further experimental and computational work is required to give a clear picture of the

---

[1] Further, the influence of the metallic substrate could alter these vibrations.

processes following the optical excitation in rhenium dyes. Further, it is not possible to clearly differentiate between properties of the isolated molecule and properties of the [Re(NCS)(CO)$_3$(DCPO$_3$bipy)]/Al$_2$O$_3$/NiAl(110) heterostructure. Interaction of molecules with metal surfaces can change both, their vibration frequency and damping [195–197]. Further, the influence of the a surface dipole change during the MLCT and the change of the image dipole are not assessed here. Also a better understanding of how excitations in molecules can affect the branching ratio during photoemission experiments is needed to interpret the changes in core-level spectra.

In future, the lifetime of the excited electrons could be increased in this system by using thicker alumina films, making it possible to observe the oscillations on a longer timescale. Semiconducting substrates could be used to promote electron injection from the molecule into a substrate or from the substrate to the molecule to study ultrafast charge transfers at the interface and processes in the charged molecule. Higher energies for the probe pulse (accessible, e.g., at free-electron lasers) would enable the detection of more core-levels. Charge transfer between different atoms could thus be observed as a change of oxidation state with high temporal resolution and elemental selectivity.

7.4 Experimental Section

Sample preparation was conducted in a modified VG ESCALAB 220 UHV system with a base pressure of $2 \cdot 10^{-10}$ mbar [49]. NiAl(110) single crystals were purchased from *MaTecK - Material-Technologie & Kristalle GmbH*. For the multilayer sample (Fig. 7.3) the NiAl(110) surface was cleaned with argon sputtering, oxidized for 1 minute in air, and a multilayer of [Re(NCS)(CO)$_3$(DCO$_2$bipy)] was deposited as described in section 5.2. For the monolayer sample (Fig. 7.4 and 7.5), a well defined ultrathin alumina film with a thickness of 0.5 nm was grown on a clean NiAl(110) surface, as described in detail in section 4.1. The ultrathin alumina film was functionalized with a monolayer of [Re(NCS)(CO)$_3$(DCPO$_3$bipy)] as described in section 5.2. The samples were transferred in a vacuum container to the Harmonium beamline and within a short air exposure mounted on a new sample holder.

The experiments were performed at the Harmonium-light source, for which a detailed description can be found elsewhere [188, 189]. The laser setup was operated with a 3 kHz repetition rate. A 3.1 eV pump pulse with a diameter of 1 mm was generated via second harmonic generation in a BBO crystal and had a power of 6 mW. The multilayer sample was studied with an 78 eV probe, and the monolayer with 88 eV. Radiation damage was observed over the course of the experiments and is discussed in Appendix D.1. A delay stage in the beam path of the pump beam was used to vary the time delay between pump and probe pulse.

8 Conclusion and Outlook

The goal of this thesis is to introduce a well-defined model system for surface science to study dye molecules on insulating thin films. The prototypical 2L-alumina/NiAl(110) system is used as a starting point and developed further by extending the alumina thickness in a well defined manner. A method for SAM deposition without exposing the substrate to air is developed, and tested during the characterization of a variety of dye molecules. As the last step, ultrafast time-resolved core-level spectroscopy is implemented as a method to study intramolecular charge transfer.

In a first step, the growth of alumina thin films on NiAl(110) is studied. Two methods are compared for growing films of variable thickness: The direct high-temperature oxidation of the clean NiAl(110) surface and the continued oxidation of 2L-alumina/NiAl(110). The latter balances the relevant processes during the film growth in a more favorable manner and delivers films of better quality. The large surface unit cell of 2L-alumina is maintained in the studied thicknesses range of up to 1.5 nm. The arrangement of the atoms inside of the unit cell changes for thicker films, which is assigned as the formation $\gamma\text{–}Al_2O_3(111)$ nuclei inside the larger unit cell. The band structure does not change drastically when the thickness of the alumina films is increased.

The resulting thin films are prone to further oxidation in air, which is an obstacle for the functionalization with dye molecules from solution. To overcome this limitation, a dedicated vacuum chamber was built. This new chamber enables the SAM deposition from solvent without exposing samples prepared in the UHV to air. A SAM of dye molecules can act as a capping layer and passivate the oxide layer.

Three rhenium dyes with systematically varied anchoring groups are deposited on 2L-alumina/NiAl(110) and are characterized with XPS and UPS. Exchanging carboxyl groups with methylene phosphonate groups on the bipy does not alter the molecular density of electronic structure of the HOMOs drastically. When the linker is attached at the axial ligand, the molecular coverage is reduced and the structure of the HOMO is affected. Further, two prototypical ruthenium dyes are adsorbed, which have a very similar electronic structure and molecular density. Compared to the rhenium dyes, the ruthenium dyes are

significantly larger and require more space on the surface.
Ultrafast core-level spectroscopy on the 4f electrons of a rhenium dye on an alumina thin film is used to study charge transfer processes. The oxidation of the metal center due to the MLCT can be observed by a chemically shifted species. This oxidized rhenium species shows an ultrafast oscillating behavior, for which no final explanation is given at the moment. It is speculated about a connection to a vibrational movement which is initiated during the optical excitation and causes intramolecular charge transfer.
Further effort is required to reach a satisfactory understanding of the observed oxidation state oscillations and charge transfer phenomena. Experiments with thicker alumina layers can increase the lifetime of the excited state to longer timescales. Varying the alumina thickness can also give insights about occurring tunneling processes. The usage of a semiconducting substrate can promote the oxidation or reduction of the excited molecule and give insight about the charged molecule, which are relevant species in homogeneous catalysis and could be used in heterogeneous catalysis. Modification of the dyes axial thiocyanate ligands could induce changes in the molecular vibrations and help to unravel the underlying mechanisms of the observed oscillations. Using pulsed light sources with higher photon energy, like free electron lasers, would make more core-levels accessible. This would enable the observation of charge carrier movement over the whole molecule, and possibly even the transfer to other catalyst molecules on the surface.

Bibliography

[1] N. S. Lewis and D. G. Nocera. Powering the planet: Chemical challenges in solar energy utilization. *Proc. Natl. Acad. Sci. U.S.A.*, 103(43):15729–15735, 2006.

[2] J. Farfan and C. Breyer. Structural changes of global power generation capacity towards sustainability and the risk of stranded investments supported by a sustainability indicator. *J. Clean. Prod.*, 141:370 – 384, 2017.

[3] D. Abbott. Keeping the energy debate clean: How do we supply the world's energy needs? *Proc. IEEE*, 98(1):42–66, 2010.

[4] G. R. Timilsina, L. Kurdgelashvili, and P. A. Narbel. Solar energy: Markets, economics and policies. *J. Renew. Sustain. Energy Rev.*, 16(1):449 – 465, 2012.

[5] M. Malinowski, J. I. Leon, and H. Abu-Rub. Solar photovoltaic and thermal energy systems: current technology and future trends. *Proc. IEEE*, 105(11):2132–2146, 2017.

[6] Andrei Ilas, Pablo Ralon, Asis Rodriguez, and Michael Taylor. *Renewable Power Generation Costs in 2017*. International Renewable Energy Agency, Abu Dhabi, 2018.

[7] T. R. Cook, D. K. Dogutan, S. Y. Reece, Y. Surendranath, T. S. Teets, and D. G. Nocera. Solar energy supply and storage for the legacy and nonlegacy worlds. *Chem. Rev.*, 110(11):6474–6502, 2010.

[8] S. Chu, Y. Cui, and N. Liu. The path towards sustainable energy. *Nat. Mater.*, 16(1):16, 2017.

[9] A. Fujishima and K. Honda. Electrochemical photolysis of water at a semiconductor electrode. *Nature*, 238(5358):37, 1972.

[10] M. Grätzel. Photoelectrochemical cells. *Nature*, 414(6861):338, 2001.

[11] A. Kudo and Y. Miseki. Heterogeneous photocatalyst materials for water splitting. *Chem. Soc. Rev.*, 38(1):253–278, 2009.

[12] M. G. Walter, E. L. Warren, J. R. McKone, S. W. Boettcher, Q. Mi, E. A. Santori, and N. S. Lewis. Solar water splitting cells. *Chem. Rev.*, 110(11):6446–6473, 2010.

[13] K. Maeda and K. Domen. Photocatalytic water splitting: Recent progress and future challenges. *J. Phys. Chem. Lett.*, 1(18):2655–2661, 2010.

[14] John R. Swierk and Thomas E. Mallouk. Design and development of photoanodes for water-splitting dye-sensitized photoelectrochemical cells. *Chem. Soc. Rev.*, 42:2357–2387, 2013.

[15] Z. Yu, F. Li, and L. Sun. Recent advances in dye-sensitized photoelectrochemical cells for solar hydrogen production based on molecular components. *Energy Environ. Sci.*, 8(3):760–775, 2015.

[16] P. Xu, N. S. McCool, and T. E. Mallouk. Water splitting dye-sensitized solar cells. *Nano Today*, 14:42 – 58, 2017.

[17] A. Hagfeldt, G. Boschloo, L. Sun, L. Kloo, and H. Pettersson. Dye-sensitized solar cells. *Chem. Rev.*, 110(11):6595–6663, 2010.

[18] F. Li, K. Fan, B. Xu, E. Gabrielsson, Q. Daniel, L. Li, and L. Sun. Organic dye-sensitized tandem photoelectrochemical cell for light driven total water splitting. *J. Am. Chem. Soc.*, 137(28):9153–9159, 2015.

[19] F. Le Formal, N. Tétreault, M. Cornuz, T. Moehl, M. Grätzel, and K. Sivula. Passivating surface states on water splitting hematite photoanodes with alumina overlayers. *Chem. Sci.*, 2(4):737–743, 2011.

[20] G. Natu, Z. Huang, Z. Ji, and Y. Wu. The effect of an atomically deposited layer of alumina on NiO in p-type dye-sensitized solar cells. *Langmuir*, 28(1):950–956, 2012.

[21] Z. Ji, M. He, Z. Huang, U. Ozkan, and Y. Wu. Photostable p-type dye-sensitized photoelectrochemical cells for water reduction. *J. Am. Chem. Soc.*, 135(32):11696–11699, 2013.

[22] C. Prasittichai, J. R. Avila, O. K. Farha, and J. T. Hupp. Systematic modulation of quantum (electron) tunneling behavior by atomic layer deposition on nanoparticulate SnO_2 and TiO_2 photoanodes. *J. Am. Chem. Soc.*, 135(44):16328–16331, 2013.

[23] M. J. Katz, M. J. DeVries Vermeer, O. K. Farha, M. J. Pellin, and J. T. Hupp. Dynamics of back electron transfer in dye-sensitized solar cells featuring 4-tert-butyl-pyridine and atomic-layer-deposited alumina as surface modifiers. *J. Phys. Chem. B*, 119(24):7162–7169, 2015.

[24] J. R. Swierk, N. S. McCool, C. T. Nemes, T. E. Mallouk, and C. A. Schmuttenmaer. Ultrafast electron injection dynamics of photoanodes for water-splitting dye-sensitized photoelectrochemical cells. *J. Phys. Chem. C*, 120(11):5940–5948, 2016.

[25] L. J. Antila, M. J. Heikkilä, V. Mäkinen, N. Humalamäki, M. Laitinen, V. Linko, P. Jalkanen, J. Toppari, V. Aumanen, M. Kemell, P. Myllyperkiö, K. Honkala, H. Häkkinen, M. Leskelä, and J. E. I. Korppi-Tommola. ALD grown aluminum oxide submonolayers in dye-sensitized solar cells: The effect on interfacial electron transfer and performance. *J. Phys. Chem. C*, 115(33):16720–16729, 2011.

[26] N. S. McCool, J. R. Swierk, C. T. Nemes, C. A. Schmuttenmaer, and T. E. Mallouk. Dynamics of electron injection in SnO_2/TiO_2 core/shell electrodes for water-splitting dye-sensitized photoelectrochemical cells. *J. Phys. Chem. Lett.*, 7(15):2930–2934, 2016.

[27] W. J. Youngblood, S.-H. A. Lee, Y. Kobayashi, E. A. Hernandez-Pagan, P. G. Hoertz, T. A. Moore, A. L. Moore, D. Gust, and T. E. Mallouk. Photoassisted overall water splitting in a visible light-absorbing dye-sensitized photoelectrochemical cell. *J. Am. Chem. Soc.*, 131(3):926–927, 2009.

[28] Gerhard Ertl: "The Nobel Prize in Chemistry 2007 - Prize Announcement".

[29] R. M. Jaeger, H. Kuhlenbeck, H.-J. Freund, M. Wuttig, W. Hoffmann, R. Franchy, and H. Ibach. Formation of a well-ordered aluminium oxide overlayer by oxidation of NiAl(110). *Surf. Sci.*, 259(3):235–252, 1991.

[30] J. Libuda, F. Winkelmann, M. Bäumer, H.-J. Freund, T. Bertrams, H. Neddermeyer, and K. Müller. Structure and defects of an ordered alumina film on NiAl(110). *Surf. Sci.*, 318(1-2):61–73, 1994.

[31] G. Kresse, M. Schmid, E. Napetschnig, M. Shishkin, L. Köhler, and P. Varga. Structure of the ultrathin aluminum oxide film on NiAl(110). *Science*, 308(5727):1440–1442, 2005.

[32] M. Kulawik, N. Nilius, H.-P. Rust, and H.-J. Freund. Atomic structure of antiphase domain boundaries of a thin Al_2O_3 film on NiAl(110). *Phys. Rev. Lett.*, 91:256101, 2003.

[33] M. Schmid, M. Shishkin, G. Kresse, E. Napetschnig, P. Varga, M. Kulawik, N. Nilius, H.-P. Rust, and H.-J. Freund. Oxygen-deficient line defects in an ultrathin aluminum oxide film. *Phys. Rev. Lett.*, 97:046101, 2006.

[34] U. Diebold, S.-C. Li, and M. Schmid. Oxide surface science. *Annu. Rev. Phys. Chem.*, 61:129–148, 2010.

[35] H.-J. Freund and G. Pacchioni. Oxide ultra-thin films on metals: new materials for the design of supported metal catalysts. *Chem. Soc. Rev.*, 37:2224, 2008.

[36] H.-J. Freund, N. Nilius, T. Risse, and S. Schauermann. A fresh look at an old nano-technology: catalysis. *Phys. Chem. Chem. Phys.*, 16(18):8148–8167, 2014.

[37] A. Einstein. Über einen die erzeugung und verwandlung des lichtes betreffenden heuristischen gesichtspunkt. *Ann. Phys. (Berl.)*, 322(6):132–148, 1905.

[38] A. Damascelli, Z. Hussain, and Z.-X. Shen. Angle-resolved photoemission studies of the cuprate superconductors. *Rev. Mod. Phys.*, 75:473–541, 2003.

[39] A. Damascelli. Probing the electronic structure of complex systems by arpes. *Phys. Scr.*, 2004(T109):61, 2004.

[40] Stephan Hüfner. *Photoelectron spectroscopy: principles and applications*. Springer Science & Business Media, 1995.

[41] Osterwalder J. *Electron Based Methods: 3.2.2 Photoelectron Spectroscopy and Diffraction in "Surface and Interface Science"*, chapter 3.2, pages 151–214. Wiley-Blackwell, 2014.

[42] Seah M. P. and Dench W. A. Quantitative electron spectroscopy of surfaces: A standard data base for electron inelastic mean free paths in solids. *Surf. Interface Anal.*, 1(1):2–11, 1979.

[43] S. Tanuma, Powell C. J., and Penn D. R. Calculations of electron inelastic mean free paths. IX. Data for 41 elemental solids over the 50 ev to 30 kev range. *Surf. Interface Anal.*, 43(3):689–713, 2011.

[44] S. Tanuma, C. J. Powell, and D. R. Penn. Calculations of electron inelastic mean free paths. v. data for 14 organic compounds over the 50-2000 ev range. *Surf. Interface Anal.*, 21(3):165–176, 1994.

[45] H. C. Poon and S. Y. Tong. Focusing and diffraction effects in angle-resolved x-ray photoelectron spectroscopy. *Phys. Rev. B*, 30:6211–6213, 1984.

[46] M. Greif, L. Castiglioni, D. Becker-Koch, J. Osterwalder, and M. Hengsberger. Acquisition of photoelectron diffraction patterns with a two-dimensional wide-angle electron analyzer. *J. Electron. Spectrosc. Relat. Phenom.*, 197:30 – 36, 2014.

[47] T. Pillo. PhD thesis, University of Freiburg, 1999.

[48] Dominik Leuenberger. *Electron Dynamics in Low-Dimensional Surfaces Studied by Time-Resolved Photoelectron Spectroscopy*. PhD thesis, University of Zurich, 2012.

[49] T. Greber, O. Raetzo, T. J. Kreutz, P. Schwaller, W. Deichmann, E. Wetli, and J. Osterwalder. A photoelectron spectrometer for k-space mapping above the Fermi level. *Rev. Sci. Instrum.*, 68(12):4549–4554, 1997.

[50] Q.-H. Wu, A. Fortunelli, and G. Granozzi. Preparation, characterisation and structure of Ti and Al ultrathin oxide films on metals. *Int. Rev. Phys. Chem*, 28(4):517, 2009.

[51] W.-D. Zabka, D. Leuenberger, G. Mette, and J. Osterwalder. From two- to three-dimensional alumina: Interface templated films and formation of $\gamma Al_2O_3(111)$ nuclei. *Phys. Rev. B*, 96:155420, 2017.

[52] W.-D. Zabka, M. Mosberger, Z. Novotny, D. Leuenberger, G. Mette, T. Kälin, B. Probst, , and J. Osterwalder. Functionalization and passivation of ultrathin alumina films of defined sub-nanometer thickness with self-assembled monolayers. *submitted*, 2018.

[53] N. M. Martin, J. Knudsen, S. Blomberg, J. Gustafson, J. N. Andersen, E. Lundgren, H. Härelind Ingelsten, P.-A. Carlsson, M. Skoglundh, A. Stierle, and G. Kresse. High-resolution core-level spectroscopy study of the ultrathin aluminum oxide film on NiAl(110). *Phys. Rev. B*, 83:125417, 2011.

[54] W. Song and M. Yoshitake. X-ray photoelectron spectroscopy and low-energy electron diffraction study on the oxidation of NiAl(110) surfaces at elevated temperatures. *Thin Solid Films*, 464:52, 2004.

[55] M. Yoshitake, T. Lay, and W. Song. Well-ordered ultra-thin Al_2O_3 film formation on NiAl(110) by high-temperature oxidation. *Surf. Sci.*, 564(1):211, 2004.

[56] T. T. Lay, M. Yoshitake, and W. Song. Epitaxial growth of well-ordered ultra-thin Al_2O_3 film on NiAl(110) by a single-step oxidation. *Appl. Surf. Sci.*, 239(3):451, 2005.

[57] Y. Lykhach, V. Moroz, and M. Yoshitake. Formation of epitaxial Al_2O_3/NiAl(110) films: aluminium deposition. *Appl. Surf. Sci.*, 241(1):250, 2005. The 9th International Symposium on Advanced Physical Fields.

[58] J. Sauer and H.-J. Freund. Models in catalysis. *Catal. Lett.*, 145(1):109–125, 2015.

[59] H.-J. Freund. Model studies in heterogeneous catalysis. *Chem. Eur. J.*, 16(31):9384–9397, 2010.

[60] G. Pacchioni and S. Valeri. *Oxide Ultrathin Films: Science and Technology*. Wiley, 2012.

[61] C. Freysoldt, P. Rinke, and M. Scheffler. Ultrathin oxides: Bulk-oxide-like model surfaces or unique films? *Phys. Rev. Lett.*, 99:086101, 2007.

[62] G. Pacchioni, L. Giordano, and M. Baistrocchi. Charging of metal atoms on ultrathin $\mathrm{MgO}/\mathrm{Mo}(100)$ films. *Phys. Rev. Lett.*, 94:226104, 2005.

[63] M. Sterrer, T. Risse, M. Heyde, H.-P. Rust, and H.-J. Freund. Crossover from three-dimensional to two-dimensional geometries of Au nanostructures on thin MgO(001) films: A confirmation of theoretical predictions. *Phys. Rev. Lett.*, 98:206103, 2007.

[64] M. Sterrer, T. Risse, U. Martinez Pozzoni, L. Giordano, M. Heyde, H.-P. Rust, G. Pacchioni, and H.-J. Freund. Control of the charge state of metal atoms on thin mgo films. *Phys. Rev. Lett.*, 98:096107, 2007.

[65] J. Repp and G. Meyer. Scanning tunneling microscopy of adsorbates on insulating films. from the imaging of individual molecular orbitals to the manipulation of the charge state. *Appl. Phys. A*, 85(4):399–406, 2006.

[66] C. Freysoldt, P. Rinke, and M. Scheffler. Controlling polarization at insulating surfaces: Quasiparticle calculations for molecules adsorbed on insulator films. *Phys. Rev. Lett.*, 103:056803, 2009.

[67] O. T. Hofmann, P. Rinke, M. Scheffler, and G. Heimel. Integer versus Fractional Charge Transfer at Metal(/Insulator)/Organic Interfaces: Cu(/NaCl)/TCNE. *ACS Nano*, 9(5):5391, 2015.

[68] M. D. Kane, F. S. Roberts, and S. L. Anderson. Effects of Alumina Thickness on CO Oxidation Activity over Pd_{20}/Alumina/Re(0001): Correlated Effects of Alumina Electronic Properties and Pd_{20} Geometry on Activity. *J. Phys. Chem. C*, 119(3):1359, 2015.

[69] J. Zhou, J. Zhou, N. Camillone, and M. G. White. Electronic charging of non-metallic clusters: size-selected $Mo_x\,S_y$ clusters supported on an ultrathin alumina film on NiAl(110). *Phys. Chem. Chem. Phys.*, 14(22):8105, 2012.

[70] M. F. Peintinger, M. J. Kratz, and T. Bredow. Quantum-chemical study of stable, meta-stable and high-pressure alumina polymorphs and aluminum hydroxides. *J. Mater. Chem. A*, 2(32):13143, 2014.

[71] C. Bara, E. Devers, M. Digne, A.-F. Lamic-Humblot, G. D. Pirngruber, and X. Carrier. Surface science approaches for the preparation of alumina-supported hydrotreating catalysts. *ChemCatChem*, 7(21):3422, 2015.

[72] G. Busca. The surface of transitional aluminas: A critical review. *Catal. Today*, 226:2, 2014.

[73] T. N. Jensen, K. Meinander, S. Helveg, A. S. Foster, S. Kulju, T. Musso, and J. V. Lauritsen. Atomic structure of a spinel-like transition $Al_2O_3(100)$ surface. *Phys. Rev. Lett.*, 113:106103, 2014.

[74] C. Becker, J. Kandler, H. Raaf, R. Linke, T. Pelster, M. Dräger, M. Tanemura, and K. Wandelt. Oxygen adsorption and oxide formation on $Ni_3Al(111)$. *J. Vac. Sci. Technol. A*, 16(3):1000–1005, 1998.

[75] V. Maurice, G. Despert, S. Zanna, M.-P. Bacos, and P. Marcus. Self-assembling of atomic vacancies at an oxide/intermetallic alloy interface. *Nat. Mater.*, 3(10):687–691, 2004.

[76] V. Rose, V. Podgursky, I. Costina, R. Franchy, and H. Ibach. High temperature oxidation of CoAl(100). *Surf. Sci.*, 577:139–150, 2005.

[77] M. Antlanger, W. Mayr-Schmölzer, J. Pavelec, F. Mittendorfer, J. Redinger, P. Varga, U. Diebold, and M. Schmid. $Pt_3Zr(0001)$: A substrate for growing well-ordered ultrathin zirconia films by oxidation. *Phys. Rev. B*, 86:035451, 2012.

[78] A. Picone, M. Riva, A. Brambilla, A. Calloni, G. Bussetti, M. Finazzi, F. Ciccacci, and L. Duò. Reactive metal-oxide interfaces: A microscopic view. *Surf. Sci. Rep.*, 71(1):32–76, 2016.

[79] S. Shaikhutdinov, M. Heemeier, J. Hoffmann, I. Meusel, B. Richter, M. Bäumer, H. Kuhlenbeck, J. Libuda, H.-J. Freund, R. Oldman, S.D. Jackson, C. Konvicka, M. Schmid, and P. Varga. Interaction of oxygen with palladium deposited on a thin alumina film. *Surf. Sci.*, 501(3):270, 2002.

[80] J. Sainio, M. Eriksson, and J. Lahtinen. Interaction of oxygen with chromium deposited on Al_2O_3/NiAl(110). *Surf. Sci.*, 532:396, 2003. Proceedings of the 7th International Conference on Nanometer-Scale Science and Technology and the 21st European Conference on Surface Science.

[81] T. Wu, W. E. Kaden, W. A. Kunkel, and S. L. Anderson. Size-dependent oxidation of Pd_n ($n \leq 13$) on alumina/NiAl(110): Correlation with Pd core level binding energies. *Surf. Sci.*, 603(17):2764, 2009.

[82] C.-W. Yi and J. Szanyi. D_2O Adsorption on an Ultrathin Alumina Film on NiAl(110). *J. Phys. Chem. C*, 111(47):17597, 2007.

[83] A. Shavorskiy, K. Müller, J. T. Newberg, D. E. Starr, and H. Bluhm. Hydroxylation of Ultrathin Al_2O_3/NiAl(110) Films at Environmental Humidity. *J. Phys. Chem. C*, 118(50):29340–29349, 2014.

[84] T. Staudt, A. Desikusumastuti, M. Happel, E. Vesselli, A. Baraldi, S. Gardonio, S. Lizzit, F. Rohr, and J. Libuda. Modeling NO_x Storage Materials: A High-Resolution Photoelectron Spectroscopy Study on the Interaction of NO_2 with Al_2O_3/NiAl(110) and BaO/Al_2O_3/NiAl(110). *J. Phys. Chem. C*, 112(26):9835, 2008.

[85] C.-W. Yi and J. Szanyi. BaO/Al_2O_3/NiAl(110) Model NO_x Storage Materials: The Effect of BaO Film Thickness on the Amorphous-to-Crystalline $Ba(NO_3)_2$ Phase Transition. *J. Phys. Chem. C*, 113(2):716, 2009.

[86] C. Weilach, C. Spiel, K. Föttinger, and G. Rupprechter. Carbonate formation on Al_2O_3 thin film model catalyst supports. *Surf. Sci.*, 605(15):1503, 2011.

[87] B. R. Strohmeier. An ESCA method for determining the oxide thickness on aluminum alloys. *Surf. Interface Anal.*, 15(1):51–56, 1990.

[88] C. J. Powell and A. Jablonski. *NIST Electron Inelastic-Mean-Free-Path Database - Version 1.2*. National Institute of Standards and Technology, Gaithersburg, MD, 2010.

[89] N. Cabrera and N. F. Mott. Theory of the oxidation of metals. *Rep. Prog. Phys.*, 12(1):163, 1949.

[90] C. J. Powell and A. Jablonski. Evaluation of Calculated and Measured Electron Inelastic Mean Free Paths Near Solid Surfaces. *J. Phys. Chem. Ref. Data*, 28(1):19, 1999.

[91] S. Andersson, P. A. Brühwiler, A. Sandell, M. Frank, J. Libuda, A. Giertz, B. Brena, A. J. Maxwell, M. Bäumer, H.-J. Freund, and N. Mårtensson. Metal-oxide interaction for metal clusters on a metal-supported thin alumina film. *Surf. Sci.*, 442(1):L964–L970, 1999.

[92] C. S. Fadley. Angle-resolved x-ray photoelectron spectroscopy. *Progr. Surf. Sci.*, 16(3):275, 1984.

[93] L'ubomír Smrčok, Vratislav Langer, and Jan Křest'an. γ-Alumina: a single-crystal X-ray diffraction study. *Acta Crystallogr. Sect. C*, 62(9):83–84, 2006.

[94] R. Browning, T. Z. Li, B. Chui, Jun Ye, R. F. W. Pease, Z. CzyXewski, and D. C. Joy. Empirical forms for the electron/atom elastic scattering cross sections from 0.1 to 30 keV. *J. Appl. Phys.*, 76(4):2016, 1994.

[95] A. Vlad, A. Stierle, N. Kasper, H. Dosch, and M. Rühle. In situ x-ray study of the γ- to α-Al_2O_3 phase transformation during atmospheric pressure oxidation of NiAl(110). *J. Mater. Res. Technol.*, 21(12):3047, 2006.

[96] E. E. Newnham and Y. M. D.E. Haan. Refinement of the a Al_2O_3, Ti_2O_3, V_2O_3 and Cr_2O_3 structures. *Z. Kristallogr. Cryst. Mater.*, 117(1-6):235, 1962.

[97] L. Kovarik, A. Genc, C. Wang, A. Qiu, C. H. F. Peden, J. Szanyi, and J. H. Kwak. Tomography and high-resolution electron microscopy study of surfaces and porosity in a plate-like γ-Al_2O_3. *J. Phys. Chem. C*, 117(1):179, 2012.

[98] A. Dyan, C. Azevedo, P. Cenedese, and P. Dubot. Electronic and atomic structure computation of disordered low index surfaces of γ-alumina. *Appl. Surf. Sci.*, 254(13):3819, 2008.

[99] H. P. Pinto, R. M. Nieminen, and S. D. Elliott. Ab initio study of γ-Al_2O_3 surfaces. *Phys. Rev. B*, 70:125402, 2004.

[100] M. Digne, P. Sautet, P. Raybaud, P. Euzen, and H. Toulhoat. Use of DFT to achieve a rational understanding of acid-basic properties of γ-alumina surfaces. *J. Catal.*, 226(1):54, 2004.

[101] P. Krukowski, S. Chaunchaiyakul, Y. Minagawa, N. Yajima, M. Akai-Kasaya, A. Saito, and Y. Kuwahara. Anomalous hexagonal superstructure of aluminum oxide layer grown on NiAl(110) surface. *Nanotechnology*, 27(45):455708, 2016.

[102] C. T. Campbell. Transition metal oxides: Extra thermodynamic stability as thin films. *Phys. Rev. Lett.*, 96:066106, 2006.

[103] M. Zacharias and P. Streitenberger. Crystallization of amorphous superlattices in the limit of ultrathin films with oxide interfaces. *Phys. Rev. B*, 62:8391–8396, 2000.

[104] S.-C. Lui, M. H. Kang, E. J. Mele, E. W. Plummer, and D. M. Zehner. Surface states on NiAl(110). *Phys. Rev. B*, 39:13149, 1989.

[105] C.-K. Lee, E. Cho, H.-S. Lee, K. S. Seol, and S. Han. Comparative study of electronic structures and dielectric properties of alumina polymorphs by first-principles methods. *Phys. Rev. B*, 76:245110, 2007.

[106] E. Menéndez-Proupin and G. Gutiérrez. Electronic properties of bulk γ-Al_2O_3. *Phys. Rev. B*, 72:035116, 2005.

[107] S. Krause, A. Schöll, and E. Umbach. Determination of transport levels of inorganic semiconductors by ultraviolet and inverse photoemission. *Phys. Rev. B*, 91:195101, 2015.

[108] A. K. Geim and I. V. Grigorieva. Van der waals heterostructures. *Nature*, 499(7459):419, 2013.

[109] T. Niu and A. Li. From two-dimensional materials to heterostructures. *Progr. Surf. Sci.*, 90(1):21, 2015.

[110] S. H. Chae, W. J. Yu, J. J. Bae, D. L. Duong, D. Perello, H. Y. Jeong, Q. H. Ta, Thuc H. Ly, Q. A. Vu, M. Yun, X. Duan, and Y. H. Lee. Transferred wrinkled Al_2O_3 for highly stretchable and transparent graphene-carbon nanotube transistors. *Nat. Mater.*, 12(5):403, 2013.

[111] M. P. Seah. Summary of ISO/TC 201 Standard: VII ISO 15472: 2001 – surface chemical analysis – x-ray photoelectron spectrometers – calibration of energy scales. *Surf. Interface Anal.*, 31(8):721–723, 2001.

[112] V. N. Morozov and T. Y. Morozova. Electrospray deposition as a method for mass fabrication of mono- and multicomponent microarrays of biological and biologically active substances. *Anal. Chem.*, 71(15):3110–3117, 1999.

[113] S. Kavadiya and P. Biswas. Electrospray deposition of biomolecules: Applications, challenges, and recommendations. *J. Aerosol Sci.*, 2018.

[114] L. C. Mayor, J. B. Taylor, G. Magnano, A. Rienzo, C. J. Satterley, J. N. O'Shea, and J. Schnadt. Photoemission, resonant photoemission, and x-ray absorption of a Ru(II) complex adsorbed on rutile $TiO_2(110)$ prepared by in situ electrospray deposition. *J. Chem. Phys.*, 129(11):114701, 2008.

[115] J. V. Barth, G. Costantini, and K. Kern. Engineering atomic and molecular nanostructures at surfaces. *Nature*, 437(7059):671–679, 2005.

[116] R. Mas-Balleste, J. Gomez-Navarro, C.and Gomez-Herrero, and F. Zamora. 2d materials: to graphene and beyond. *Nanoscale*, 3(1):20–30, 2011.

[117] K. S. Novoselov, A. Mishchenko, A. Carvalho, and A. H. Castro Neto. 2d materials and van der waals heterostructures. *Science*, 353(6298):9439, 2016.

[118] J. Justin Gooding and Simone Ciampi. The molecular level modification of surfaces: from self-assembled monolayers to complex molecular assemblies. *Chem. Soc. Rev.*, 40:2704–2718, 2011.

[119] S. P. Pujari, L. Scheres, A. T. M. Marcelis, and H. Zuilhof. Covalent surface modification of oxide surfaces. *Angew. Chem. Int. Ed.*, 53(25):6322–6356, 2014.

[120] D. Mandler and S. Kraus-Ophir. Self-assembled monolayers (SAMs) for electrochemical sensing. *J. Solid State Electrochem.*, 15(7):1535–1558, 2011.

[121] D. Samanta and A. Sarkar. Immobilization of bio-macromolecules on self-assembled monolayers: methods and sensor applications. *Chem. Soc. Rev.*, 40:2567–2592, 2011.

[122] A. L. Eckermann, D. J. Feld, J. A. Shaw, and T. J. Meade. Electrochemistry of redox-active self-assembled monolayers. *Coord. Chem. Rev.*, 254(15):1769 – 1802, 2010.

[123] B. Fabre. Functionalization of oxide-free silicon surfaces with redox-active assemblies. *Chem. Rev.*, 116(8):4808–4849, 2016.

[124] C. A. Schoenbaum, D. K. Schwartz, and J. W. Medlin. Controlling the surface environment of heterogeneous catalysts using self-assembled monolayers. *Acc. Chem. Res.*, 47(4):1438–1445, 2014.

[125] M. Halik and A. Hirsch. The potential of molecular self-assembled monolayers in organic electronic devices. *Adv. Mater.*, 23(22-23):2689–2695, 2011.

[126] S. Casalini, C. A. Bortolotti, F. Leonardi, and F. Biscarini. Self-assembled monolayers in organic electronics. *Chem. Soc. Rev.*, 46(1):40–71, 2017.

[127] Z. Yan, Z. Sun, W. Lu, J. Yao, Y. Zhu, and J. M. Tour. Controlled modulation of electronic properties of graphene by self-assembled monolayers on SiO_2 substrates. *ACS Nano*, 5(2):1535–1540, 2011.

[128] G. Hong, Q. Wu, J. Ren, C. Wang, W. Zhang, and S. Lee. Recent progress in organic molecule/graphene interfaces. *Nano Today*, 8(4):388 – 402, 2013.

[129] Y. Li, C.-Y. Xu, P. Hu, and L. Zhen. Carrier control of MoS_2 nanoflakes by functional self-assembled monolayers. *ACS Nano*, 7(9):7795–7804, 2013.

[130] D. M. Sim, M. Kim, S. Yim, M.-J. Choi, J. Choi, S. Yoo, and Y. S. Jung. Controlled doping of vacancy-containing few-layer mos_2 via highly stable thiol-based molecular chemisorption. *ACS Nano*, 9(12):12115–12123, 2015.

[131] M. Bibes, J. E. Villegas, and A. Barthelemy. Ultrathin oxide films and interfaces for electronics and spintronics. *Adv. Phys.*, 60(1):5–84, 2011.

[132] W. Steurer, J. Repp, L. Gross, I. Scivetti, M. Persson, and G. Meyer. Manipulation of the charge state of single au atoms on insulating multilayer films. *Phys. Rev. Lett.*, 114:036801, 2015.

[133] Michael Hollerer, Daniel Lüftner, Philipp Hurdax, Thomas Ules, Serguei Soubatch, Frank Stefan Tautz, Georg Koller, Peter Puschnig, Martin Sterrer, and Michael G. Ramsey. Charge transfer and orbital level alignment at inorganic/organic interfaces: The role of dielectric interlayers. *ACS Nano*, 11(6):6252–6260, 2017.

[134] S. Shaikhutdinov and H.-J. Freund. Ultrathin oxide films on metal supports: Structure-reactivity relations. *Annu. Rev. Phys. Chem.*, 63(1):619–633, 2012.

[135] V. Maurice, N. Frémy, and P. Marcus. Hydroxylation-induced modifications of the Al_2O_3/nial(001) surface at low water vapour pressure. *Surf. Sci.*, 581(1):88 – 104, 2005.

[136] J. Kelber, N. Magtoto, C. Vamala, M. Jain, D.R. Jennison, and P.A. Schultz. Reactivities of ultrathin alumina films exposed to intermediate pressures of h_2o: Substrate-mediated mechanism for growth and loss of surface order. *Surf. Sci.*, 601(16):3464 – 3471, 2007.

[137] J. A. Kelber. Alumina surfaces and interfaces under non-ultrahigh vacuum conditions. *Surf. Sci. Rep.*, 62(7):271 – 303, 2007.

[138] A. Kumar, S.-S. Sun, and A. J. Lees. *Photophysics and Photochemistry of Organometallic Rhenium Diimine Complexes*, pages 37–71. Springer Berlin Heidelberg, Berlin, Heidelberg, 2010.

[139] A. Vlček. *Ultrafast Excited-State Processes in Re(I) Carbonyl-Diimine Complexes: From Excitation to Photochemistry*, pages 115–158. Springer Berlin Heidelberg, Berlin, Heidelberg, 2010.

[140] K. Kam-Wing Lo. *Exploitation of Luminescent Organometallic Rhenium(I) and Iridium(III) Complexes in Biological Studies*, pages 73–114. Springer Berlin Heidelberg, Berlin, Heidelberg, 2010.

[141] H. Takeda, K. Koike, H. Inoue, and O. Ishitani. Development of an efficient photocatalytic system for CO2 reduction using rhenium(I) complexes based on mechanistic studies. *J. Am. Chem. Soc.*, 130(6):2023–2031, 2008.

[142] H. Takeda and O. Ishitani. Development of efficient photocatalytic systems for co_2 reduction using mononuclear and multinuclear metal complexes based on mechanistic studies. *Coord. Chem. Rev.*, 254(3):346 – 354, 2010.

[143] B. Probst, C. Kolano, P. Hamm, and R. Alberto. An efficient homogeneous intermolecular rhenium-based photocatalytic system for the production of H_2. *Inorg. Chem.*, 48(5):1836–1843, 2009.

[144] B. Probst, A. Rodenberg, M. Guttentag, P. Hamm, and R. Alberto. A highly stable rhenium-cobalt system for photocatalytic H_2 production: Unraveling the performance-limiting steps. *Inorg. Chem.*, 49(14):6453–6460, 2010.

[145] B. Probst, M. Guttentag, A. Rodenberg, P. Hamm, and R. Alberto. Photocatalytic H_2 production from water with rhenium and cobalt complexes. *Inorg. Chem.*, 50(8):3404–3412, 2011.

[146] A. M. Blanco Rodríguez, A. Gabrielsson, M. Motevalli, P. Matousek, M. Towrie, J. Šebera, S. Záliš, and A. Vlček. Ligand-to-diimine/metal-to-diimine charge-transfer excited states of [Re(NCS)(CO)3(α-diimine)] (α-diimine = 2,2'-bipyridine, di-^{i}pr-*N,N*-1,4-diazabutadiene). a spectroscopic and computational study. *J. Phys. Chem. A*, 109(23):5016–5025, 2005.

[147] H. Kvapilová, A. Vlček, V. Barone, M. Biczysko, and S. Záliš. Anharmonicity effects in ir spectra of [Re(X)$(CO)_3$(α-diimine)] (α-diimine = 2,2'-bipyridine or pyridylimidazo[1,5-a]pyridine; X = Cl or NCS) complexes in ground and excited electronic states. *J. Phys. Chem. A*, 119(40):10137–10146, 2015.

[148] J.H. Scofield. Hartree-slater subshell photoionization cross-sections at 1254 and 1487 ev. *J. Electron. Spectrosc. Relat. Phenom.*, 8(2):129 – 137, 1976.

[149] J. Söderström, N. Mårtensson, O. Travnikova, M. Patanen, C. Miron, L. J. Sæthre, K. J. Børve, J. J. Rehr, J. J. Kas, F. D. Vila, T. D. Thomas, and S. Svensson. Nonstoichiometric intensities in core photoelectron spectroscopy. *Phys. Rev. Lett.*, 108:193005, 2012.

[150] Jill Chastain, Roger C King, and J Moulder. *Handbook of X-ray photoelectron spectroscopy: a reference book of standard spectra for identification and interpretation of XPS data*. Physical Electronics Division, Perkin-Elmer Corporation Eden Prairie, Minnesota, 1992.

[151] A. J. Gibson, R. H. Temperton, K. Handrup, M. Weston, L. C. Mayor, and J. N. O'Shea. Charge transfer from an adsorbed ruthenium-based photosensitizer through an ultra-thin aluminium oxide layer and into a metallic substrate. *J. Chem. Phys.*, 140(23):234708, 2014.

[152] B. Kasprzyk-Hordern. Chemistry of alumina, reactions in aqueous solution and its application in water treatment. *Adv. Colloid Interface Sci.*, 110(1):19 – 48, 2004.

[153] C. Arrouvel, B. Diawara, D. Costa, and P. Marcus. DFT periodic study of the adsorption of glycine on the anhydrous and hydroxylated (0001) surfaces of α-alumina. *J. Phys. Chem. C*, 111(49):18164–18173, 2007.

[154] S. Bertazzo and K. Rezwan. Control of α-alumina surface charge with carboxylic acids. *Langmuir*, 26(5):3364–3371, 2010.

[155] M.E. Karaman, D.A. Antelmi, and R.M. Pashley. The production of stable hydrophobic surfaces by the adsorption of hydrocarbon and fluorocarbon carboxylic acids onto alumina substrates. *Colloids Surf. A*, 182(1):285 – 298, 2001.

[156] Z. Zhang, L. Li, and J. C. Yang. γ-Al_2O_3 thin film formation via oxidation of β-NiAl(110). *Acta Mater.*, 59(15):5905 – 5916, 2011.

[157] J. Evertsson, F. Bertram, F. Zhang, L. Rullik, L.R. Merte, M. Shipilin, M. Soldemo, S. Ahmadi, N. Vinogradov, F. Carlà, J. Weissenrieder, M. Göthelid, J. Pan, A. Mikkelsen, J.-O. Nilsson, and E. Lundgren. The thickness of native oxides on aluminum alloys and single crystals. *Appl. Surf. Sci.*, 349:826 – 832, 2015.

[158] R. V. Mom, J. Vermeer, J. W. M. Frenken, and I. M. N. Groot. Structural dynamics of Al_2O_3/NiAl(110) during film growth in NO_2. *J. Phys. Chem. B*, 122(2):788–793, 2018.

[159] A. Taylor and N. J. Doyle. Further studies on the nickel–aluminium system. I. β-NiAl and δ-Ni_2Al_3 phase fields. *J. Appl. Crystallogr.*, 5(3):201–209, 1972.

[160] W.-D. Zabka, T. Musso, M. Mosberger, Z. Novotny, M. Iannuzzi, J. Hutter, B. Probst, , and J. Osterwalder. Rhenium and ruthenium dyes with covalent linkers on ultrathin alumina films: Coverage, electronic and topographic structure. *in preparation*, 2018.

[161] L. Zhang and J. M. Cole. Anchoring groups for dye-sensitized solar cells. *ACS Appl. Mater. Interfaces*, 7(6):3427–3455, 2015.

[162] E. M. J. Johansson, M. Hedlund, H. Siegbahn, and H. Rensmo. Electronic and molecular surface structure of $Ru(tcterpy)(NCS)_3$ and $Ru(dcbpy)_2(NCS)_2$ adsorbed from solution onto nanostructured TiO_2: A photoelectron spectroscopy study. *J. Phys. Chem. B*, 109(47):22256–22263, 2005.

[163] M. Ikeda, N. Koide, L. Han, C. L. Pang, A. Sasahara, and H. Onishi. Lateral distribution of N3 dye molecules on $TiO_2(110)$ surface. *J. Photochem. Photobiol. A*, 202(2):185 – 190, 2009.

[164] K. E. Lee, M. A. Gomez, T. Regier, Y. Hu, and G. P. Demopoulos. Further understanding of the electronic interactions between N719 sensitizer and anatase TiO_2 films: A combined x-ray absorption and x-ray photoelectron spectroscopic study. *J. Phys. Chem. C*, 115(13):5692–5707, 2011.

[165] N. Martsinovich, F. Ambrosio, and A. Troisi. Adsorption and electron injection of the N3 metal–organic dye on the TiO_2 rutile (110) surface. *Phys. Chem. Chem. Phys.*, 14(48):16668–16676, 2012.

[166] M. Weston, T. J. Reade, K. Handrup, N. R. Champness, and J. N. O'Shea. Adsorption of dipyrrin-based dye complexes on a rutile $TiO_2(110)$ surface. *J. Phys. Chem. C*, 116(34):18184–18192, 2012.

[167] C. S. Kley, C. Dette, G. Rinke, C. E. Patrick, J. Čechal, S. J. Jung, M. Baur, M. Dürr, S. Rauschenbach, F. Giustino, S. Stepanow, and K. Kern. Atomic-scale observation of multiconformational binding and energy level alignment of ruthenium-based photosensitizers on TiO_2 anatase. *Nano Lett.*, 14(2):563–569, 2014.

[168] V. Mäkinen, K. Honkala, and H. Häkkinen. Atomic layer deposition of aluminum oxide on TiO_2 and its impact on N3 dye adsorption from first principles. *J. Phys. Chem. C*, 115(18):9250–9259, 2011.

[169] U. Terranova and D. R. Bowler. Coating TiO_2 anatase by amorphous Al_2O_3: Effects on dyes anchoring through carboxyl groups. *J. Phys. Chem. C*, 116(7):4408–4415, 2012.

[170] M. Zuleta, S. Yu, S. Ahmadi, G. Boschloo, M. Göthelid, and A. Hagfeldt. Monitoring N719 dye configurations on $(1\times n)$-reconstructed anatase (100) by means of STM: Reversible configurational changes upon illumination. *Langmuir*, 26(16):13236–13244, 2010.

[171] S. Fantacci, F. De Angelis, and A. Selloni. Absorption spectrum and solvatochromism of the $[Ru(4,4'\text{-}COOH\text{-}2,2'\text{-}bpy)_2(NCS)_2]$ molecular dye by time dependent density functional theory. *J. Am. Chem. Soc.*, 125(14):4381–4387, 2003.

[172] M. K. Nazeeruddin, F. De Angelis, S. Fantacci, A. Selloni, G. Viscardi, P. Liska, S. Ito, B. Takeru, and M. Grätzel. Combined experimental and DFT-TDDFT computational study of photoelectrochemical cell ruthenium sensitizers. *J. Am. Chem. Soc.*, 127(48):16835–16847, 2005.

[173] G. Pizzoli, M. G. Lobello, B. Carlotti, F. Elisei, M. K. Nazeeruddin, G. Vitillaro, and F. De Angelis. Acid–base properties of the N3 ruthenium (II) solar cell sensitizer: a combined experimental and computational analysis. *Dalton Trans.*, 41(38):11841–11848, 2012.

[174] C. S. Fadley. X-ray photoelectron spectroscopy: Progress and perspectives. *J. Electron. Spectrosc. Relat. Phenom.*, 178:2 – 32, 2010.

[175] C. J. Powell and A. Jablonski. Progress in quantitative surface analysis by x-ray photoelectron spectroscopy: Current status and perspectives. *J. Electron. Spectrosc. Relat. Phenom.*, 178:331 – 346, 2010.

[176] M. Bauer, C. Lei, K. Read, R. Tobey, J. Gland, M. M. Murnane, and H. C. Kapteyn. Direct observation of surface chemistry using ultrafast soft-x-ray pulses. *Phys. Rev. Lett.*, 87:025501, 2001.

[177] A. Pietzsch, A. Föhlisch, M. Beye, M. Deppe, F. Hennies, M. Nagasono, E. Suljoti, W. Wurth, C. Gahl, K. Döbrich, and A. Melnikov. Towards time resolved core level photoelectron spectroscopy with femtosecond x-ray free-electron lasers. *New J. Phys.*, 10(3):033004, 2008.

[178] S. Hellmann, C. Sohrt, M. Beye, T. Rohwer, F. Sorgenfrei, M. Marczynski-Bühlow, M. Kalläne, H. Redlin, F. Hennies, M. Bauer, A. Föhlisch, L. Kipp, W. Wurth, and K. Rossnagel. Time-resolved x-ray photoelectron spectroscopy at flash. *New J. Phys.*, 14(1):013062, 2012.

[179] T. Katayama, T. Anniyev, M. Beye, R. Coffee, M. Dell'Angela, A. Föhlisch, J. Gladh, S. Kaya, O. Krupin, A. Nilsson, D. Nordlund, W. F. Schlotter, J. A. Sellberg, F. Sorgenfrei, J. J. Turner, W. Wurth, H. Öström, and H. Ogasawara. Ultrafast soft x-ray emission spectroscopy of surface adsorbates using an x-ray free electron laser. *J. Electron. Spectrosc. Relat. Phenom.*, 187:9–14, 2013.

[180] S. Neppl and O. Gessner. Time-resolved x-ray photoelectron spectroscopy techniques for the study of interfacial charge dynamics. *J. Electron. Spectrosc. Relat. Phenom.*, 200:64 – 77, 2015.

[181] O. Gessner and M. Gühr. Monitoring ultrafast chemical dynamics by time-domain x-ray photo- and auger-electron spectroscopy. *Acc. Chem. Res.*, 49(1):138–145, 2016.

[182] H. Dachraoui, M. Michelswirth, P. Siffalovic, P. Bartz, C. Schäfer, B. Schnatwinkel, J. Mattay, W. Pfeiffer, M. Drescher, and U. Heinzmann. Photoinduced reconfiguration cycle in a molecular adsorbate layer studied by femtosecond inner-shell photoelectron spectroscopy. *Phys. Rev. Lett.*, 106:107401, 2011.

[183] K. R. Siefermann, C. D. Pemmaraju, S. Neppl, A. Shavorskiy, A. A. Cordones, J. Vura-Weis, D. S. Slaughter, F. P. Sturm, F. Weise, H. Bluhm, M. L. Strader, H. Cho, M.-F. Lin, C. Bacellar, C. Khurmi, J. Guo, G. Coslovich, J. S. Robinson, R. A. Kaindl, R. W. Schoenlein, A. Belkacem, D. M. Neumark, S. R. Leone, D. Nordlund, H. Ogasawara, O. Krupin, J. J. Turner, W. F. Schlotter, M. R. Holmes, M. Messerschmidt, M. P. Minitti, S. Gul, J. Z. Zhang, N. Huse, D. Prendergast, and O. Gessner. Atomic-scale perspective of ultrafast charge transfer at a dye-semiconductor interface. *J. Phys. Chem. Lett.*, 5(15):2753–2759, 2014.

[184] W. R. Browne and B. L. Feringa. Light switching of molecules on surfaces. *Annu. Rev. Phys. Chem.*, 60(1):407–428, 2009.

[185] M. Chergui and E. Collet. Photoinduced structural dynamics of molecular systems mapped by time-resolved x-ray methods. *Chem. Rev.*, 117(16):11025–11065, 2017.

[186] G. D. Scholes, G. R. Fleming, L. X. Chen, A. Aspuru-Guzik, A. Buchleitner, D. F. Coker, G. S. Engel, R. Van Grondelle, A. Ishizaki, D. M. Jonas, J. S. Lundeen, J. K. McCusker, S. Mukamel, J. P. Ogilvie, A. Olaya-Castro, M. A. Ratner, F. C. Spano, K. B. Whaley, and X. Zhu. Using coherence to enhance function in chemical and biophysical systems. *Nature*, 543(7647):647, 2017.

[187] A. Vlček and S. Záliš. Modeling of charge-transfer transitions and excited states in d6 transition metal complexes by DFT techniques. *Coord. Chem. Rev.*, 251(3):258 – 287, 2007.

[188] J. Ojeda, C. A. Arrell, J. Grilj, F. Frassetto, L. Mewes, H. Zhang, F. van Mourik, L. Poletto, and M. Chergui. Harmonium: A pulse preserving source of monochromatic extreme ultraviolet (30-110 eV) radiation for ultrafast photoelectron spectroscopy of liquids. *Struct. Dyn.*, 3(2):023602, 2016.

[189] C. A. Arrell, J. Ojeda, L. Longetti, A. Crepaldi, S. Roth, G. Gatti, A. Clark, F. van Mourik, M. Drabbels, M. Grioni, and M. Chergui. Harmonium: An ultrafast vacuum ultraviolet facility. *CHIMIA*, 71(5):268–272, 2017.

[190] A. Ausmees, S. J. Osborne, R. Moberg, S. Svensson, S. Aksela, O.-P. Sairanen, A. Kivimäki, A. Naves de Brito, E. Nõmmiste, J. Jauhiainen, and H. Aksela. High-resolution study of the Xe $4d_{5/2}$:$4d_{3/2}$ branching ratio. *Phys. Rev. A*, 51:855–858, 1995.

[191] K. T. Cheng and W. R. Johnson. Orbital collapse and the photoionization of the inner 4*d* shells for Xe-like ions. *Phys. Rev. A*, 28:2820–2828, 1983.

[192] N. Shanthi and P. C. Deshmukh. Xenon 4p photoionization near the 4d cooper minimum: Interchannel coupling effects. *Phys. Rev. A*, 40:2400–2403, 1989.

[193] Private communication with Ricardo Fernández-Terán.

[194] A. Cannizzo, A. M. Blanco-Rodríguez, A. El Nahhas, J. Šebera, S. Záliš, A. Vlček, and M. Chergui. Femtosecond fluorescence and intersystem crossing in rhenium(I) carbonyl-bipyridine complexes. *J. Am. Chem. Soc.*, 130(28):8967–8974, 2008.

[195] B. N. J. Persson and R. Ryberg. Vibrational interaction between molecules adsorbed on a metal surface: The dipole-dipole interaction. *Phys. Rev. B*, 24:6954–6970, 1981.

[196] B. Hellsing and M. Persson. Electronic damping of atomic and molecular vibrations at metal surfaces. *Phys. Scr.*, 29(4):360, 1984.

[197] S. P. Rittmeyer, V. J. Bukas, and K. Reuter. Energy dissipation at metal surfaces. *Adv. Phys. X*, 3(1):1381574, 2018.

A Supplemental Material:Ultrathin alumina films on NiAl(110)

A.1 From two- to three-dimensional alumina: Interface templated films and formation of γ-Al_2O_3(111) nuclei (Supplemental Material)

This section contains the Supplemental Material of the paper included in section 4.3.

A.1.1 Non-normalized core level spectra

The intensity of the substrate peaks is exponentially dampened when an overlayer is grown ontop. The measured intensity of the substrate I_S can be described by [90]:

$$\frac{I_S}{I_S^\infty} = \exp\left(-\frac{d}{\lambda_O\left(E_{Kin}\right)\cos\theta}\right), \tag{A.1}$$

and for the overlayer I_L by:

$$\frac{I_L}{I_L^\infty} = 1 - \exp\left(-\frac{d}{\lambda_O\left(E_{Kin}\right)\cos\theta}\right). \tag{A.2}$$

Here d is the overlayer thickness, λ_O is the inelastic mean free path of the photoelectrons in the overlayer and θ is the electron emission angle. The respective spectra were taken at normal emission $\theta = 0°$. The Ni^0 3p, the Al^0 2p and the Al^{3+} 2p peaks have nearly the same binding energy and thus kinetic energy in the range of 1177 to 1187 eV. The same $\lambda_O\left(E_{Kin}\right)$ can be assumed for all peaks, as the variation of $\lambda_O\left(E_{Kin}\right)$ is small according to

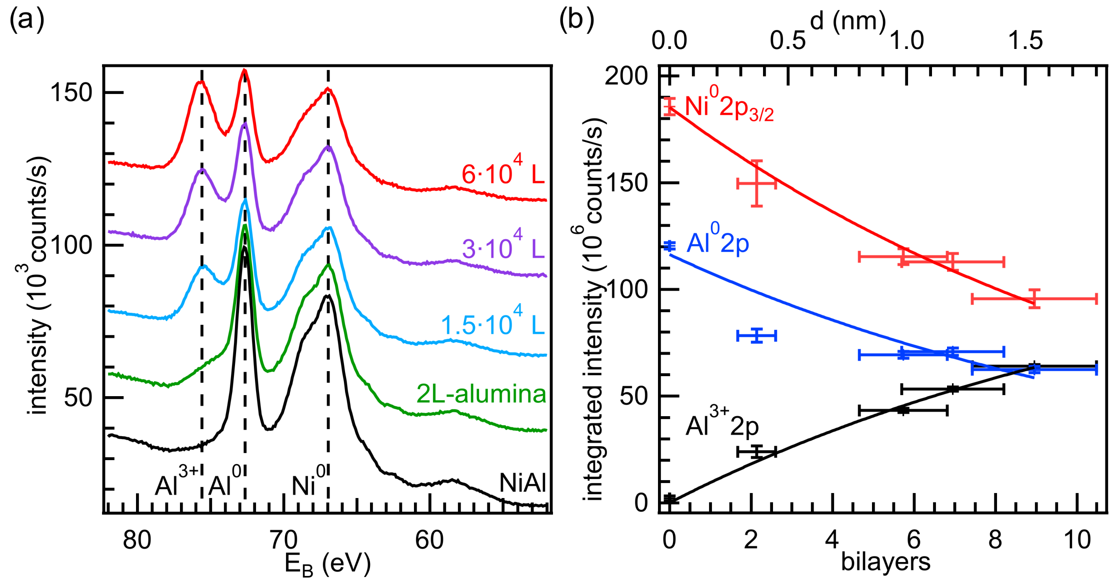

Figure A.1: (a) Al 2p and Ni 3p core level spectra of NiAl(110), 2L-alumina/NiAl(110) and 2L-alumina/NiAl(110) after several oxygen dosages recorded with an unmonochromatized Mg Kα source. (b) Evolution of the intensity. An increase of the Al^{3+} signal indicates oxide formation while the substrate intensity decreases. The lines indicate the fitted results.

the TTP-2M equation [88]:

$$\frac{\lambda_O\,(1187\,\text{eV}) - \lambda_O\,(1177\,\text{eV})}{\lambda_O\,(1187\,\text{eV})} \leq 0.007. \qquad \text{(A.3)}$$

The peak intensities were fitted according to Eq. A.1 and A.2 and resulted in a common exponent of $\lambda_O = 2.24 \pm 0.07\,\text{nm}$. This compares well to the theoretical value of $\lambda_O\,(1182\,\text{eV}) = 2.67 \pm 0.47\,\text{nm}$ from the TPP-2M equation [88]. A bandgap of 6.4 eV was used (valence band onset of 4.2 eV as determined in A.5(b), conduction band 2.2 eV above the Fermi level [91].

A.1.2 XPD simulations

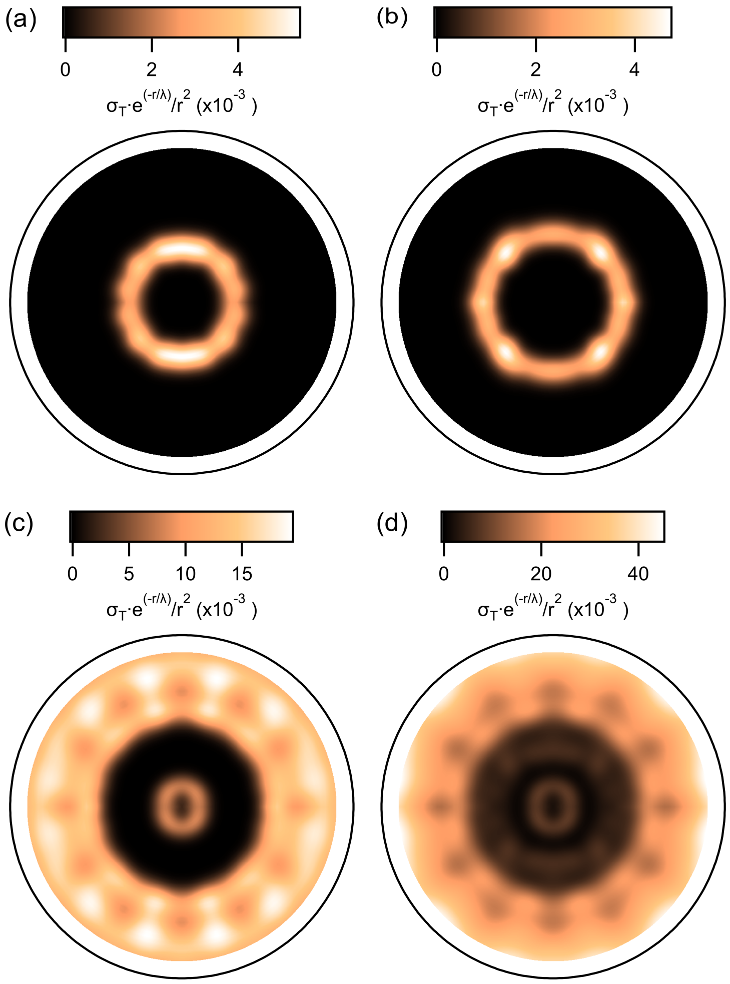

Figure A.2: XPD simulations regarding 2L-alumina based on the structural model of Kresse et. al [31]. No background subtraction is applied. (a) Scattering of O_i on O_s for $\Theta \leq 40°$ (tetrahedral blocks). (b) Scattering of O_i on O_s for $40° \leq \Theta \leq 48°$ (pyramidal blocks). (c) Scattering of O_i on all Al_s. (d) Scattering of O_i on all O_s and Al_s.

It is known that under ambient conditions and depending on temperature, the formation of epitaxial γ-Al_2O_3(111) and α-Al_2O_3(0001) on NiAl(110) is possible [95]. The simulated XPD of α-Al_2O_3(0001) shown in Fig. S3(c) is significantly different. Further, the formation of α-Al_2O_3 requires in general temperatures above 1270 K. It is likely that the short range order in films thicker than 1.0 nm can be accurately described as γ-Al_2O_3(111)-like.

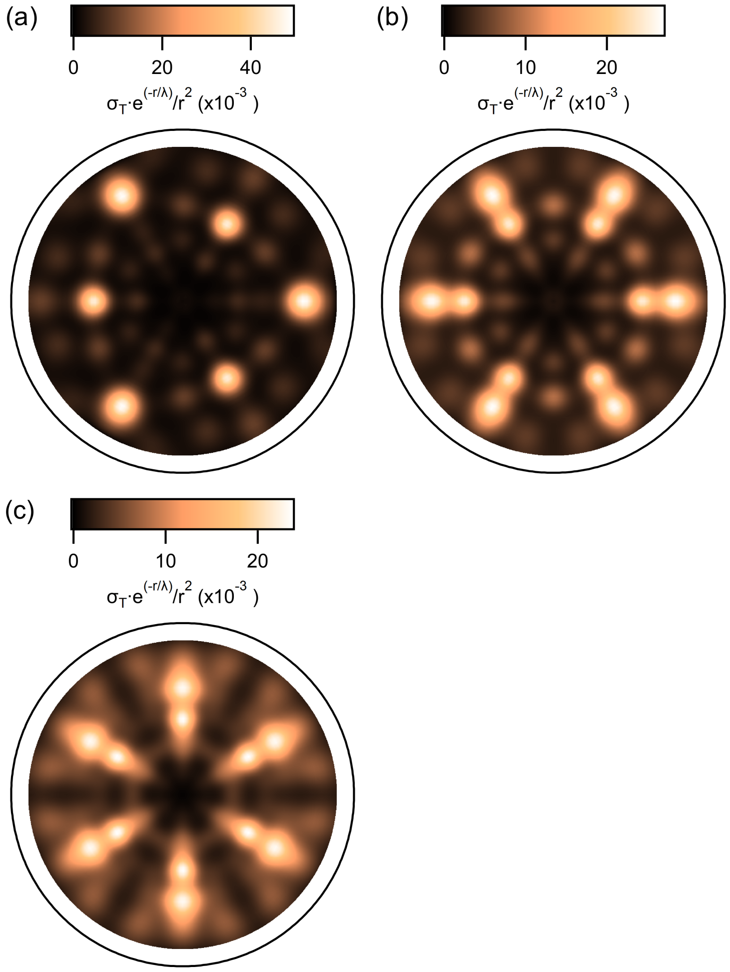

Figure A.3: (a) XPD simulation of γ-Al_2O_3(111) according to the structural model from Ref. [93]. (b) As (a), but two-fold symmetrization applied. (c) XPD simulation of α-Al_2O_3(0001) according to the structural model from Ref. [96] (six-fold symmetry applied).

A.1.3 2^{nd} derivative in energy of the ARPES data

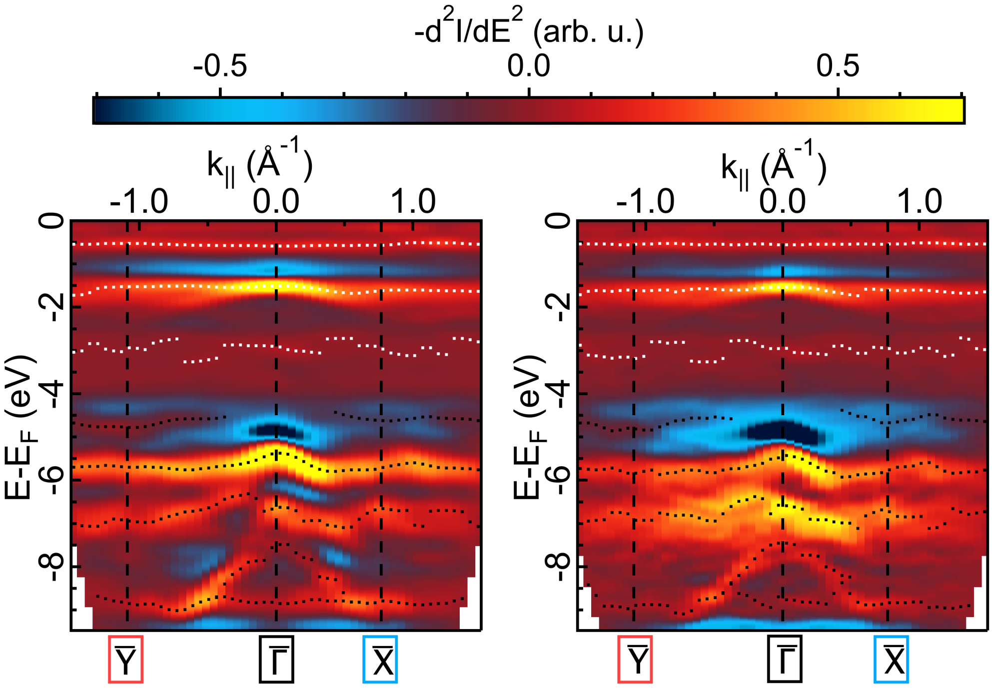

Figure A.4: Inverted 2^{nd} derivative in energy of the measured ARPES data from 2L-alumina (left) and from a 1.5 nm-thick-film (right) in Fig. 4(a). Identified bands of the NiAl(110) substrate and of alumina are marked with white and black dots, respectively.

A.1.4 Valence band onset and work function

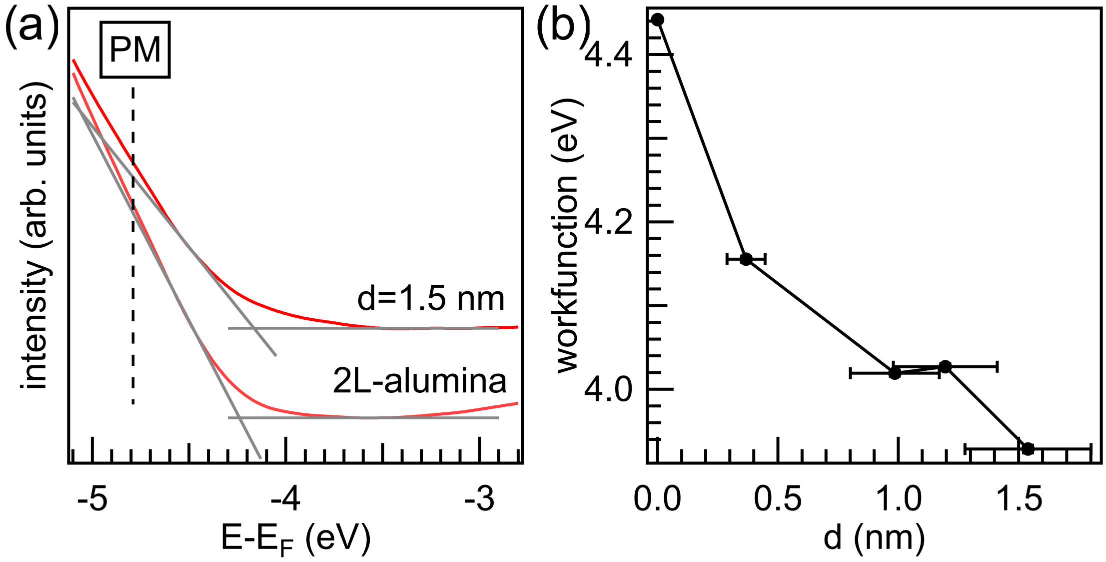

Figure A.5: (a) Fit for determining the valence band onset at $\bar{Y}$ for 2L-alumina and a 1.5 nm-thick-film. (b) Evolution of the work function with increasing film thickness measured by ultraviolet photoelectron spectroscopy.

A.2 Simplified XPD pattern simulations for the high energy regime and large clusters

The in Appendix A.1.2 and section 4.3.3 used code for the simulation of XPD pattern is a simple and fast code that can be used for high kinetic energies. It was developed further and based on three assumptions:

1. The intensity I of a photoelectron wave emitting from an atom is decreasing with the distance r like a spherical wave: $I \propto \frac{1}{r^2}$
2. I decreases exponentially due to scattering processes: $I \propto e^{-r/\lambda}$
3. I is enhanced by an enhancement factor X in the forward direction when it encounters an atom: $I \propto X$

Along the internuclear direction, the enhancement factor of one scattering event can be simplified to [45]:

$$X_J = \left[1 + f(0)/R_j\right]^2. \tag{A.4}$$

Here, R_j is the distance between emitter and scatterer and $f(0)$ is the scattering factor. According to Ref. [45], the scattering factor of copper approaches for high kinetic energies $f_{\mathrm{Cu}}(0) = 5.54\,\text{Å}$. For the simulations it is assumed that $f(0)$ scales with the total electron-atom elastic scattering cross section σ_T, which is calculated according to Ref. [94]:

$$\sigma_T(Z, E_{Kin}) = \frac{3 \cdot 10^{-2} Z^{1.7}}{E_{Kin} + 0.005 Z^{1.7} {E_{Kin}}^{0.5} + 0.0007 Z^2 / {E_{Kin}}^{0.5}}\,\text{Å}^2. \tag{A.5}$$

Here, Z is the atomic number and E_{Kin} the kinetic energy of the electrons. With this scaling, the intensity modulation ΔI of a photoelectron wave due to scattering on an atom j can be expressed as:

$$\Delta I_j = \frac{\left[1 + \frac{f_{\mathrm{Cu}}(0)}{R_j} \frac{\sigma_T}{\sigma_{\mathrm{Cu}}}\right]^2}{{R_j}^2} \cdot e^{-R_j/\lambda}. \tag{A.6}$$

For λ a universal expression of the electron inelastic mean free path is used, which depends only on E_{Kin} (in eV) [175]:

$$\lambda = \frac{0.00523 E_{Kin}^3}{48.6 - 1.76 E_{Kin} + 0.0518 E_{Kin}^2 (-2.61 + \ln(E_{Kin}))}. \tag{A.7}$$

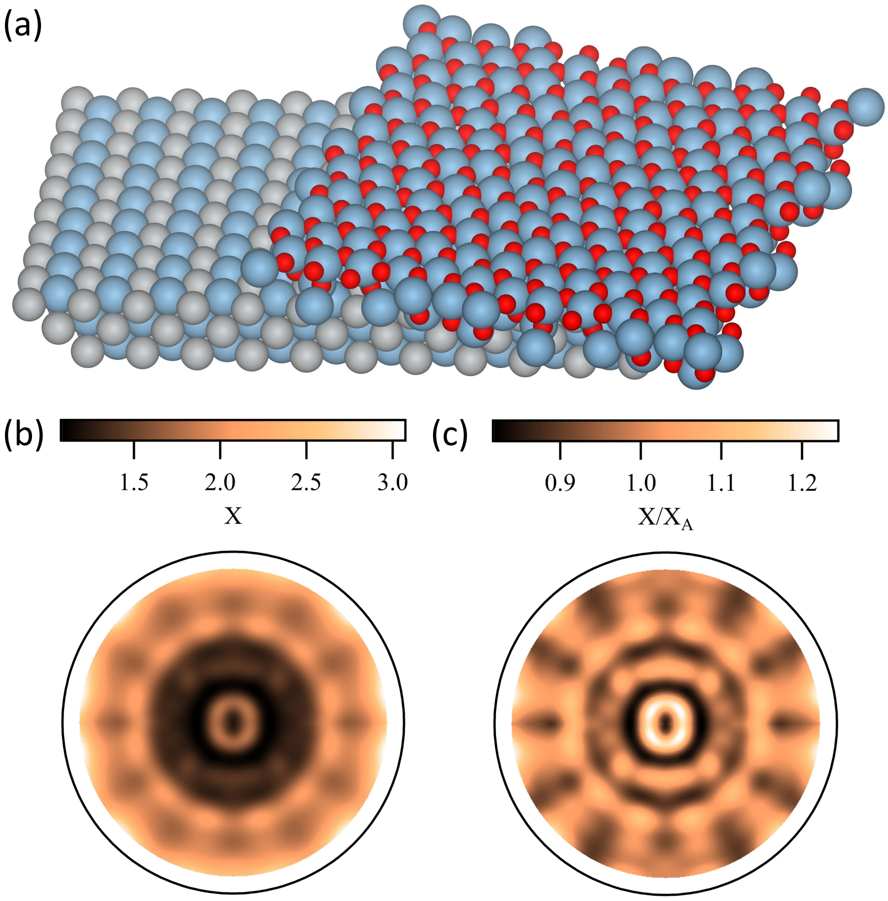

Figure A.6: (a) Cluster used for the simulations. (b) Calculated enhancement X. (c) X with a Gauss divided background.

The total photoelectron intensity is expressed as $I = \alpha N$, where α is the atomic subshell photoionization cross section of the emitter and N the number of emitters in the cluster. The intensity enhancement of the system can then be expressed as:

$$X = \frac{I + \sum_j \Delta I_j}{I}. \tag{A.8}$$

A Gaussian broadening and a binning are used, as previously described (section 4.3.3). This code neglects most phenomena but can describe observed features in the XPD qualitatively. The advantage is that it is fast and can be used for large clusters. Fig. A.6 (a) shows the cluster used for the simulations of 2L-alumina in Fig. 4.4. It contains more than 1000 atoms. The same cluster is used here, and X is computed on a normal computer within a few minutes. The computed pattern for the enhancement is shown in Fig. A.6. The C_{2V} symmetry of the substrate and film [29] was applied to the data. The background subtracted data in Fig. A.6 (c) can be compared to the previous simulations and experimental data in Fig. 4.4.

A.3 Conduction band of 2L-alumina with 2PPE

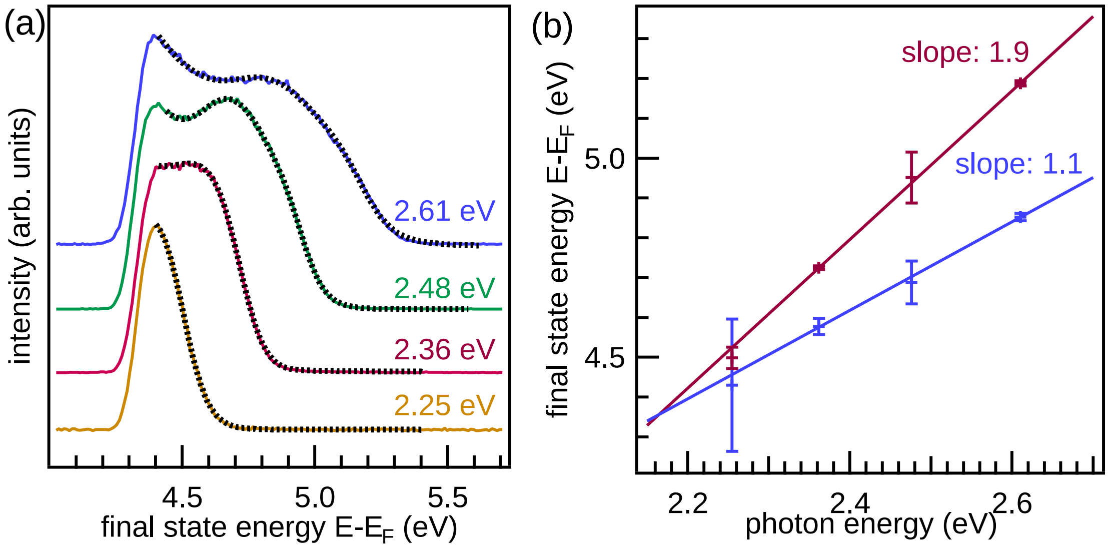

Figure A.7: 2PPE measurements of 2L-alumina/NiAl(110): (a) 2PPE spectra with different photon energies and corresponding fits (black dotted lines). (b) Final state energy of the measured Fermi edge (red) and the peak position (blue) dependent on the used photon energy and belonging linear fits.

The conduction band of 2L-alumina was measured with 2PPE. Laser pulses were generated by a Ti:sapphire laser and the photon energy was varied with an optical parametric amplifier. The 2PPE spectra for different photon energies are shown in Fig. A.7 (a). Electrons from the metal substrate are transferred to the conduction band of 2L-alumina with the first photon. A phonon is required for the change of momentum. The second photon transfers the electron into the vacuum. The spectra are fitted with the sum of a Fermi function, a Gauss function and an exponential background. Fig. A.7 (b) shows the final state energy of the extracted Fermi edge and the peak maximum. The error bars correspond to the standard deviation. Linear fits deliver a slope of 1.9±0.1 for the Fermi edge, indicating that two photons promote electrons from the Fermi level of the NiAl(110) substrate to the vacuum. The slope of the peak maximum is 1.1±0.1. This indicates that an intermediate state at a fixed energy is filled with a first photon, and electrons from that state are promoted to the vacuum with the second photon. The position of this feature is 2.2 ± 0.4 eV above the Fermi level. This value is in good agreement with a value previously found by X-ray absorption spectroscopy [91].

B Supplemental material: Functionalization of ultrathin alumina films on NiAl(110) with self-assembled monolayers

B.1 Beam damage through X-ray radiation and loss of passivation

Radiation damage upon X-ray exposure is a common phenomenon for large molecules and can be of various origins: Hot electrons generated in the substrate can fill unoccupied molecular states of antibonding character or scatter in the molecules and excite vibrations. Further, direct photoexcitation could result in electronically excited states with potential energy landscapes which lead to dissociation. The X-ray radiation used for the XPS measurements damages the molecule after a certain time, which is observed in a shift of the Re 4f peak by 0.5 eV to lower binding energies and a peak broadening (Fig. B.1 (a)). A half-life time $T_{1/2}$ of the molecules is calculated based on the increase of the full width at half maximum (FWHM) (Fig. B.1 (b)). Data within $T_{1/2}$ was used for the analysis of the molecule composition in Table 1 and Fig. 3 of the main manuscript. After exposing a sample with damaged molecules to air (Fig. B.1 (c)), we observe new rhenium species at higher binding energies. Most likely the rhenium from decomposed molecules becomes metallic and oxidizes during the air exposure. Further, as can be seen by the increase of the oxide shoulder of the Al 2p peak, the passivation effect of the molecular overlayer is lost.

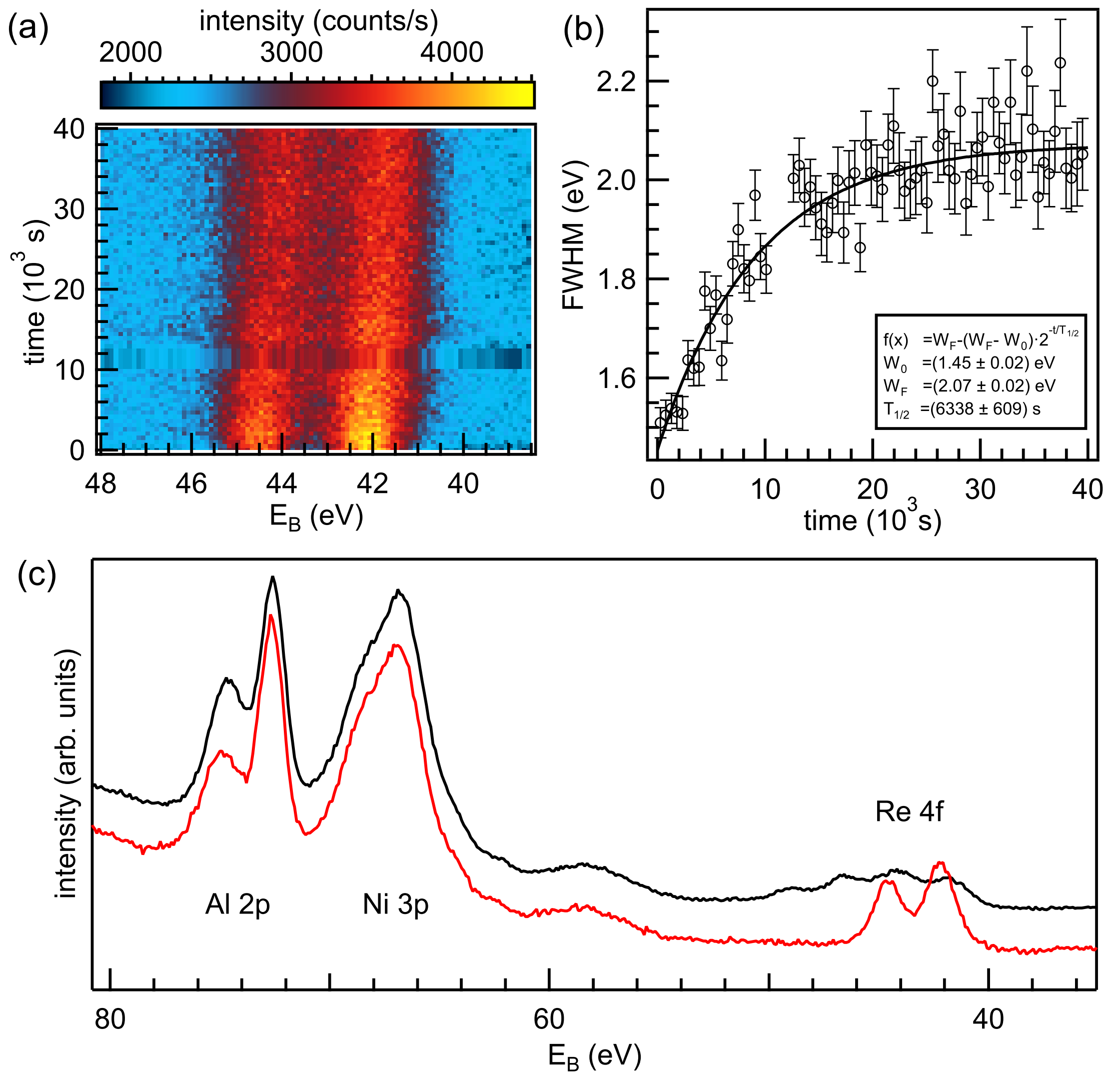

Figure B.1: (a) A shift to lower binding energies and broadening of the Re 4f Peaks during XPS measurements indicates beam damage by the used X-rays. (b) Saturation of the FWHM of the Re 4f peaks over time and determination of the half-life time $T_{1/2}$. (c) Al 2p, Ni 3p and Re 4f peak

B.2 Oxygen 1s XPS

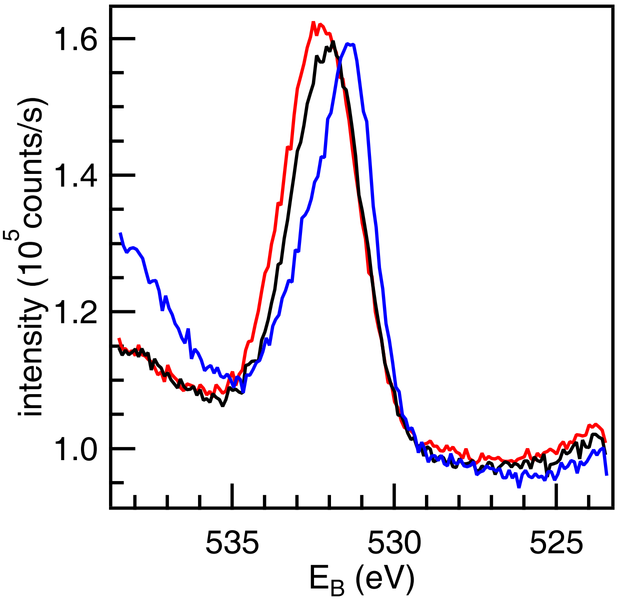

Figure B.2: Oxygen 1s spectrum of 2L-alumina (blue), after SAM deposition (red), and after ongoing radiation damage (black).

During SAM deposition a shift to higher binding energies is observed in the oxygen 1s spectrum due to the formation of further alumina, hydroxide, and due to oxygen in the molecule. After radiation-induced damage the SAM, a slight decrease in the oxygen signal and a shift to lower binding energies are observed. This can be due to loss of oxygen in the carboxyl or carbonyl groups of the molecule.

C Supplemental Material: Rhenium and ruthenium dyes with covalent linkers on alumina/NiAl(110)

C.1 Comparison of molecule (3) in mono- and multilayer

Fig. C.1 compares the mono- and multilayer coverage of molecule (3). The intensity of the Re 4f peak serves as a normalization factor. Fig. C.1 (a) shows the Al 2p, the Ni 3p and the Re 4f peaks. As the intensity of the Re 4f peak was used for normalization, they have the same height, and the substrate Al 2p and Ni 3p peaks are dampened. The S 2p spectrum (Fig. C.1 (b)) shows in the multilayer coverage one distinguished peak at $169\,eV$, which is a typical binding energy for sulfones and sulfates [150]. This peak origins from the OTf counterion. In the monolayer coverage, this peak is not the dominant sulfur species anymore, which indicates a decomposition of the counterion. Approximately 70 % of the counterions decomposed. In the multilayer, the F 1s spectrum (see Fig. C.1 (c)) of the multilayer is described well by a single peak at a binding energy of 689 eV. Fluorine is a further element in the OTf counterion. The atomic ratio between sulfur and fluorine deducted from the S 2p peak at 169 eV the F 1s peak and is 1.0:2.1 in the multilayer and 1.0:2.4 in the monolayer, further indicating that they together origin from the OTf. The N 1s peak (Fig. C.1 (d)) shows in the multilayer one clear peak from nitrogen atoms in the pyridine and bipy. In the monolayer, this peak significantly broadens. The atomic ratios of rhenium, sulfur, fluorine, and nitrogen are in the multilayer 1.0:1.2:2.2:2.9, and in the monolayer 1:0:0.8:2.4:3.7 (both sulfur peaks accounted in the monolayer).

We conclude that a multilayer of molecules and counterions can be adsorbed. In the monolayer, most counterions decompose and release the fluorine.

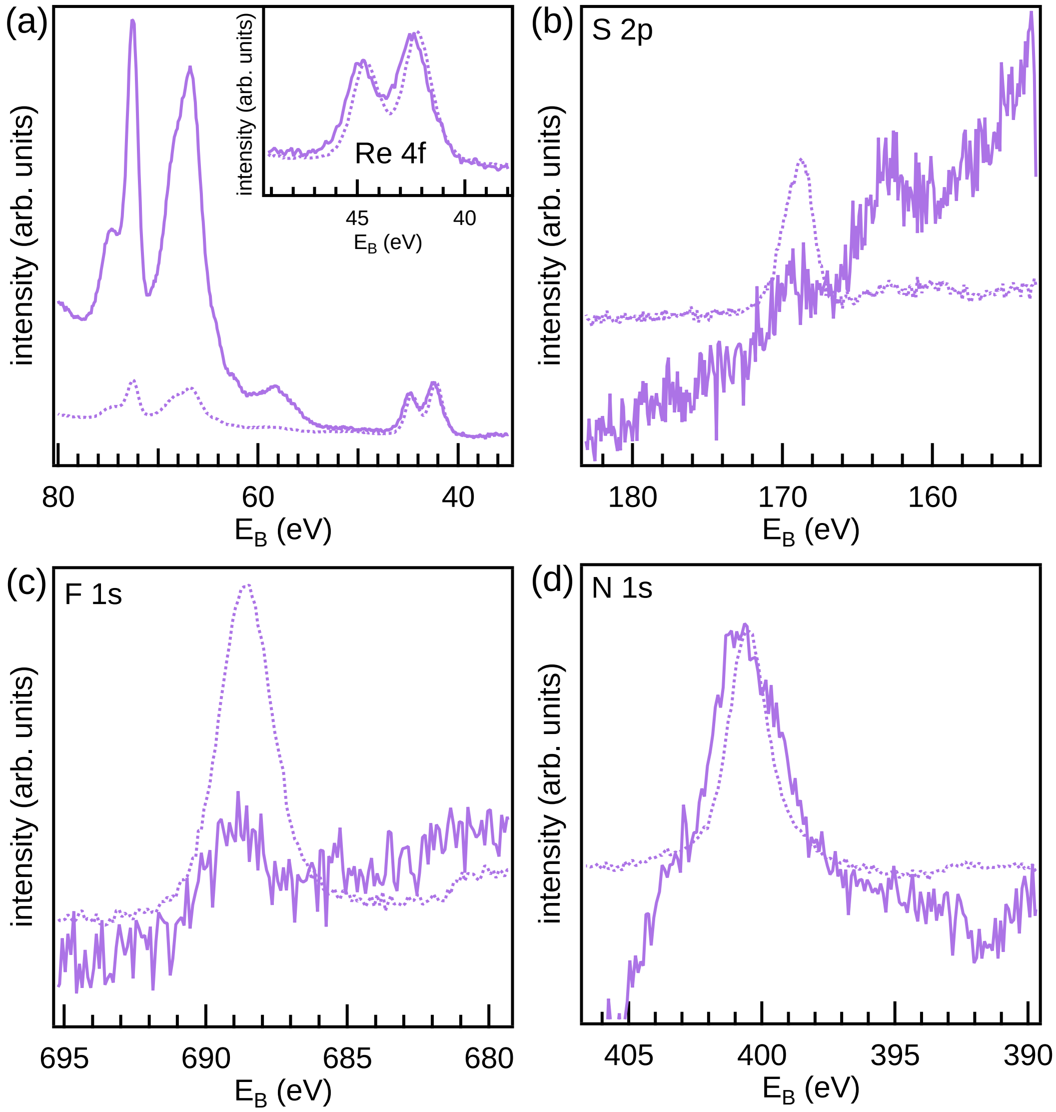

Figure C.1: XPS of the (a) Al 2p, Ni 3p and Re 4f, (b) S 2p, (c) F 1s, and (d) N 1s core-level of molecule (3) in the monolayer (solid line) and multilayer (dashed line).

C.2 Beam damage through ultraviolet radiation and calculation of initial work function

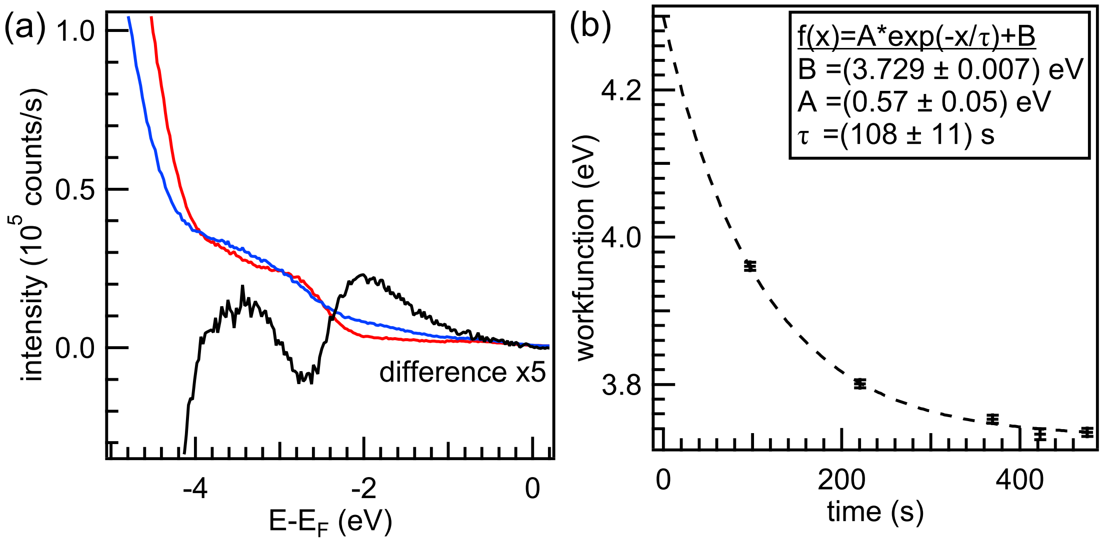

Figure C.2: (a) UPS of a SAM of molecule (1) within the first 80 seconds under the helium discharce lamp (red), after 240 seconds (blue), and their difference (black). (b) Work function decrease of the SAM/alumina/NiAl(110) heterostructure during the measurement. An exponential fit (dashed line) is used to find the initial work function. A helium discharge lamp (He I$_\alpha$, h$\nu = 21.2$ eV) was used.

Similarly to X-rays while conducting the XPS measurements, also the ultraviolet photons from the helium discharge lamp damage the molecule. Fig. C.2 (a) shows the measured UPS of molecule (1) at the beginning of the measurement (red), as in Fig. 6 (a) of the main manuscript, and the UPS after 240 seconds of measurement (blue). The difference (black) indicates that density of states is lost 2.8 eV beneath the Fermi level, where the HOMO is located. An intensity gain during the molecule decay is observed 2.0 eV beneath the Fermi level. The work function is measured using the secondary electron cutoff and decreases as a result of the radiation damage fast over time (Fig. C.2 (b)). An exponential fit is applied to calculate the initial work function of the SAM, which is (4.30 ± 0.05) eV.

C.3 Absorption spectrum

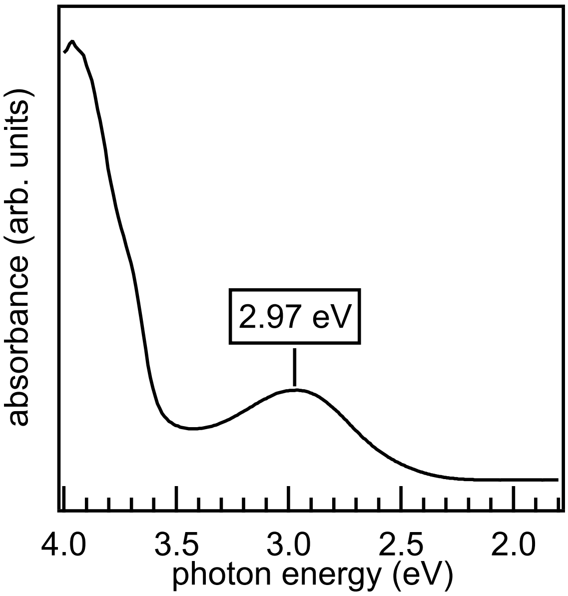

Figure C.3: Absorption spectrum in the ultraviolet-visible photon range of molecule (1) in acetonitrile (concentration of 0.1 mM). Courtesy of Mathias Mosberger.

C.4 Work function and HOMO energies

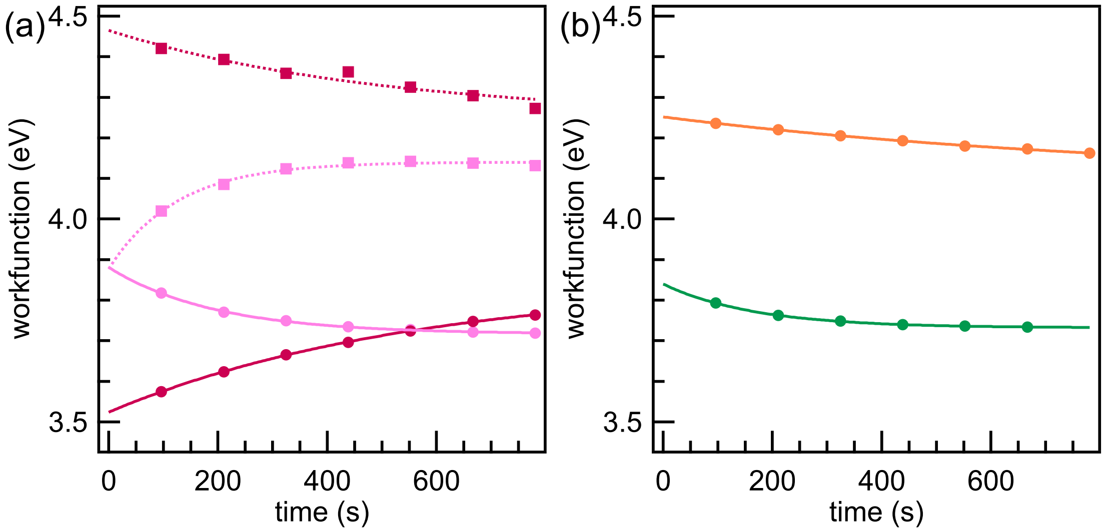

Figure C.4: Evolution of the work function under UV light (markers). Exponential fits are used to find the initial work function of the mono- (solid line) and multilayer (dashed line). (a) molecule (2) (red) and (3) (magenta) in mono- (circles) and multilayer (squares). Exponential fits are used to find the initial work function. (b) Same for monolayers of molecule (4) (orange) and (5) (green).

The dye molecules are prone to radiation damage and are evaluated as discussed in Appendix C.2. Table C.1 shows the resulting values for the work function and the binding energy values of the peak maxima from Fig. 6.6.

Table C.1: Work function and peak position of the HOMO measured by UPS.

molecule		HOMO (eV)	work function (eV)
(1)	mono	-2.8(5)	4.3(0)
	multi	-2.7(3)	-
(2)	mono	-2.9(7)	3.5(2)
	multi	-2.6(4)	4.4(6)
(3)	mono	-3.1(6)	3.8(8)
		-3.8(6)	
	multi	-3.9(1)	3.8(8)
(4)	mono	-2.1(4)	4.2(5)
(5)	mono	-2.2(4)	3.8(4)

C.5 Average separation

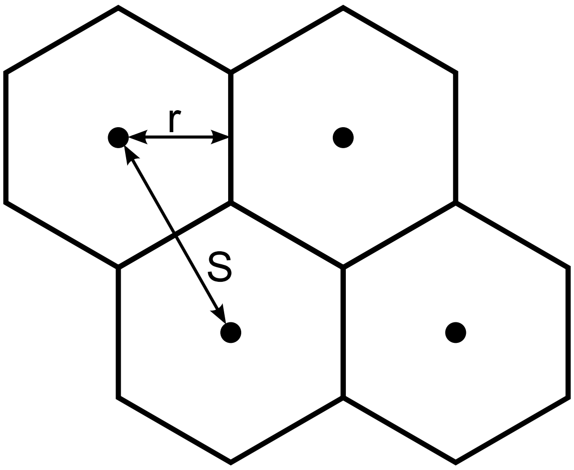

Figure C.5: Scheme for the separation of molecules based on a hexagonal arrangement.

The average separation S is calculated from the density of molecules N. The area a molecule requires at average is assumed to be the of an hexagon with $A_{Hex} = 2\sqrt{3}r^2 = 1/N$, as indicated in Fig. C.5. It follows for S:

$$\begin{aligned} S &= 2 \cdot r \\ &= 2 \cdot \sqrt{\frac{A_{Hex}}{2\sqrt{3}}} \\ &= \sqrt{\frac{2}{\sqrt{3}N}} \end{aligned} \tag{C.1}$$

D Supplemental Material: Metal-to-ligand charge transfer observed with ultrafast time-resolved core-level spectroscopy

D.1 Beam damage

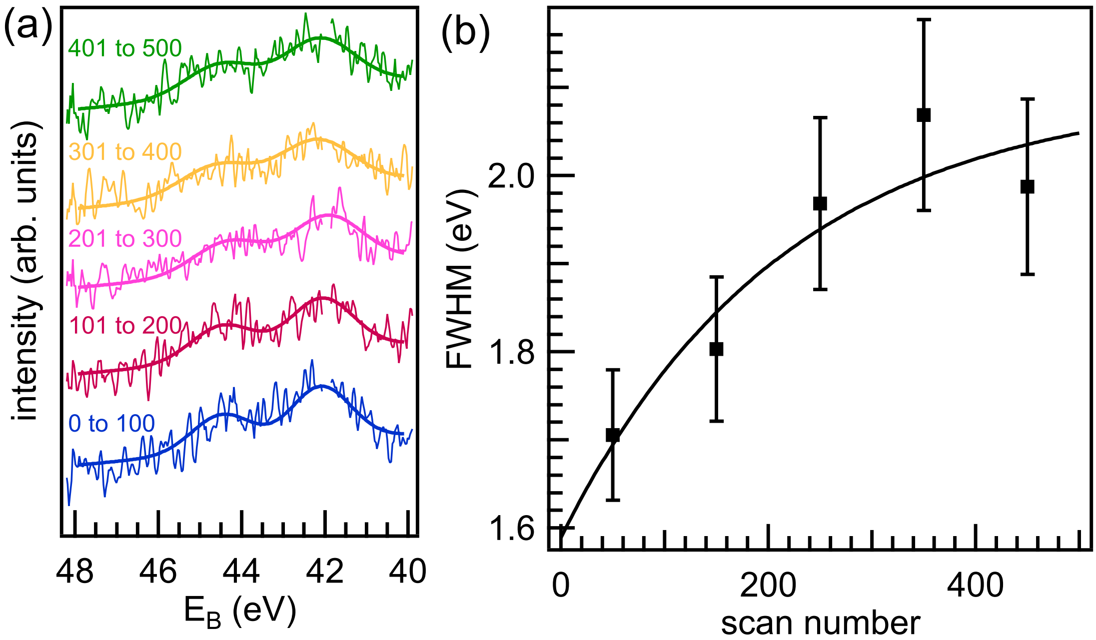

Figure D.1: (a) Spectra of the Re 4f peak prior excitation (thin line) and corresponding fits (thick line). (b) Evolution of the FWHM of the Re 4f peaks during the measurement (markers) and a fit with a saturation curve (black line).

Beam damage in rhenium dyes upon X-ray and ultraviolet light exposure was previously described (see Appendix sct:BeamDamage and sct:Workfunction). The Re 4f peak shifts to lower binding energies and broadens. Fig. D.1 (a) shows spectra of the [Re(NCS)(CO)$_3$(DPO$_3$bipy)] monolayer prior the excitation for different scan numbers, and corresponding fits with two Gauss curves of the same width. Data points due to a hot pixel at $E_B = 42\,\mathrm{eV}$ were removed. Fig. D.1 (b) show the evolution of the full width at half maximum (FWHM) during the measurement, indicating a significant increase over the time of the measurement through beam damage. The whole measurement had a total number of 583 time-delay scans.

Acknowledgment

Acknowledgment will be added after the defense.

List of Publications

- W. Zabka, D. Leuenberger, G. Mette, and J. Osterwalder, From two- to three-dimensional alumina: Interface templated films and formation of γ-$Al_2O_3(111)$ nuclei, *Phys. Rev. B* **96** 155420 (2017)
- D. Leuenberger, W. Zabka, O. Shah, S. Schnidrig, B. Probst, R. Alberto, and J. Osterwalder, Atomically Resolved Band Bending Effects in a p-n Heterojunction of Cu_2O and a Cobalt Macrocycle, *Nano Lett.* **17** 6620 (2017)
- M. Graf, G. Mette, D. Leuenberger, Y. Gurdal, M. Iannuzzi, W. Zabka, S. Schnidrig, B. Probst, J. Hutter, R. Alberto, and J. Osterwalder, The impact of metalation on adsorption geometry, electronic level alignment and UV-stability of organic macrocycles on $TiO_2(110)$, *Nanoscale* **9** 8756 (2017)
- E. Miniussi, C. Bernard, H. Cun, B. Probst, D. Leuenberger, G. Mette, W. Zabka, M. Weinl, M. Haluska, M. Schreck, J. Osterwalder, and T Greber, Fermi surface map of large-scale single-orientation graphene on SiO_2, *J. Phys.: Condens. Matter* **29** 475001 (2017)
- C. Cui, M.c Heggen, W. Zabka, W. Cui, J. Osterwalder, B. Probst and R. Alberto, Atomically dispersed hybrid nickel-iridium sites for photoelectrocatalysis, *Nat. Commun.* **8** 1341 (2017)

Wolf-Dietrich Zabka

Regensbergstrasse 38 – 8050 Zürich – Switzerland – E-Mail: wolf.zabka@gmail.com – Mobil: +41 7678 56789

Personal Information

Date of birth:	12th October 1988
Place of birth:	Ueckermünde, Germany
Nationality:	German

Educational Background

07/2014-07/2018	**PhD: Experimental Physics, University of Zurich (Surface Physics Group)** – thesis title: Oxide thin film functionalization with self-assembled photosensitizers at the two-dimensional limit
10/2011-01/2014	**Master: Physics, Humboldt University Berlin (Specialization: Solid State Physics)** – thesis title: Untersuchung der Wasseradsorption an der galliumreichen Galliumphosphid (100)-Oberfläche im Vakuum
10/2007-09/2011	**Bachelor: Physics, University of Rostock** – thesis title: In situ EDXRD Untersuchung von Kalziumtitanat synthetisiert mit dem Sol-Gel-Verfahren

Work Experience

07/2014-07/2018	**PhD Candidate, Surface Physics Group, University of Zurich** – thesis work conducted in an ESCA laboratory (XPS, XPD, UPS, ARPES, STM,LEED) – user facility beam time organization and participation (NAPP-XPS, FLASH) – supervision of thesis and project work – teaching activities (physics for medicine and biomedicine students) – transitional responsibility for laboratory (organization of laboratory usage and maintenance)
09/2012-04/2013	**Student Assistant, Helmholtz-Zentrum Berlin für Materialien und Energie** – MOCVD growth of III-V-semiconductors – microscopy measurements (AFM)
01/2011-03/2011	**Student Assistant, New Materials group, University of Rostock** – X-ray diffraction data evaluation and interpretation
09/2009	**Intern, Max Planck Institute for plasma physics** – experimental studies about ionic sound waves

International Experience

04/2011-07/2011	**Volunteering, Ladakh Ecological Development Group in India** – simulations about housing insulation – project documentation
10/2010-12/2010	**Volunteering, Travelworks in Costa Rica** – projects for sea turtle protection – nocturnal nesting area patrolling